High Strength, High Toughness Microalloyed Steel Forgings Produced with Relaxed Forging Conditions and No Heat Treatment

by

Aaron Edwin Stein

B.S. in Engineering Science, Saint Vincent College, 2016

Submitted to the Graduate Faculty of the

Swanson School of Engineering in partial fulfillment

of the requirements for the degree of

Master of Science in Materials Science and Engineering

University of Pittsburgh

2019

UNIVERSITY OF PITTSBURGH

SWANSON SCHOOL OF ENGINEERING

This thesis was presented

by

Aaron Edwin Stein

It was defended on

November 20, 2019

and approved by

John Oyler, PhD, Professor, Department of Civil and Environmental Engineering

Patrick Smolinski, PhD, Professor, Department of Mechanical Engineering and Materials Science

Brian Gleeson, PhD, Professor, Department of Mechanical Engineering and Materials Science

Thesis Advisor: Anthony J. DeArdo, PhD, Professor, Department of Mechanical Engineering and Materials Science

Copyright © by Aaron Edwin Stein

2019

High Strength, High Toughness Microalloyed Steel Forgings Produced with Relaxed Forging Conditions and No Heat Treatment

Aaron Edwin Stein, MS

University of Pittsburgh, 2019

Three steel compositions were designed and investigated as possible materials for the forging of a wheel hub geometry using the recrystallization controlled forging (RCF) process. Titanium nitride (TiN) technology was utilized to control prior austenite grain sizes (PAGS) and vanadium precipitation to strengthen ferrite. For processing, two cooperating systems were investigated, RCF, for refinement of the PAGS, and controlled cooling, where interrupted direct quenching (IDQ) and indirect accelerated cooling (IAC) provided multiple possible physical property combinations. The response of the steels to thermo-mechanical processing (TMP) was investigated to determine optimal forging conditions for refinement of the PAGS. The maximum reheat temperature to avoid grain coarsening, as well as the minimum forging temperature for complete recrystallization was determined. Ti and V additions were found to elevate both temperatures. After, IDQ and IAC cooling paths were performed on the steels to yield desired microstructure products. Microstructures comprising predominantly polygonal ferrite, bainite and martensite were attainable in the laboratory samples. Finally, the steels were tested at Meadville Forging Company (MFC), a collaborator in this project. Here, each steel was subjected to the MFC standard forging routine and varying cooling paths were used. Mechanical testing samples were machined and tested from the forgings. The strengths increased with cooling rate and alloying, but the fully forged, hot water quenched bainitic samples did not perform well, having lower strengths than the fast air cool to room temperature (ACRT) conditions. This is interpreted to be because of

the low alloying, specifically the low carbon, limiting the strength of the bainite when present in large bainite phase percentages. The performance of the steels is compared with those of similar steels and discussed from metallurgical standpoints. Methods of improving upon the current design of the steels are discussed. This research has demonstrated that low-carbon compositions, when subjected to proper RCF processing, are capable of being refined to equivalent circular prior austenite grain diameters approaching 10μm. Additionally, ultimate tensile strengths in the non-water quench to room temperature (WQRT) conditions were observed between 550MPa and 720MPa, and approaching 940MPa in the WQRT condition, with good toughness in all conditions.

Table of Contents

List of Tables

List of Figures

Acknowledgements

Over the course of this thesis, the support of many people has been crucial to my success, and here I would like to extend my gratitude to these people for their support.

First and foremost, my gratitude is extended to my advisor, Dr. Anthony J. DeArdo. The knowledge and experience he has in the field of physical metallurgy is remarkable, and his willingness to share this with me has been a crucial resource for me over the course of my study. Additionally, I would like to thank the other members of my thesis committee, Professor Gleeson, Professor Oyler and Professor Smolinski for their efforts in reviewing my thesis, as well as attending my thesis defense and providing their insights to improve my thesis.

Secondly, I would acknowledge my appreciation to Dr. Hua who personally conducted much of my training, as well as helping with preparation and testing of samples. Additionally, the efforts of Qionshu Wang are acknowledged for their importance in my training and preparation for my work. Finally, the fellow members of the BAMPRI group, namely Dr. Bing Ma, Yingjie Wu, Xinchi Feng and Rami Almatani have my deepest thanks. The peer mentoring, help and friendship they have extended to me have been crucial over the course of my work, and in my development as an individual.

Ultimately, I need to extend my thanks to my parents, for the unwavering support and devotion they have offered me, as well as the support of my siblings. Without them, I would never have been able to successfully complete my degree.

Glossary

To aid in the comprehension of this document, a list of commonly referenced terminology is included below, along with the definition of the term.

RCF…	Recrystallization Controlled Forging
RCR…	Recrystallization Controlled Rolling
PAGS…	Prior Austenite Grain Size
PAGB…	Prior Austenite Grain Boundary
IDQ…	Interrupted Direct Quenching
IAC…	Indirect Accelerated Cooling
TMP…	Thermo-Mechanical Processing
ACRT…	Air Cool to Room Temperature
WQRT…	Water Quench to Room Temperature
HSLA Steel…	High Strength Low Alloy Steel
QT Steel…	Quench and Tempered Steel
CCR…	Conventional Controlled Rolling
CHR…	Conventional Hot Rolling
D_I...	Ideal Diameter
T_{GC}…	Grain Coarsening Temperature
T_{RH}…	Reheat Temperature
T_{95}/T_{RX}…	Deformation Temperature for 95% Recrystallization
T_5…	Deformation Temperature for 5% Recrystallization

WET…	Water End Temperature
VIM…	Vacuum Induction Melting
OM…	Optical Microscopy
SEM…	Scanning Electron Microscopy
EDS…	Energy Dispersive Spectroscopy
TEM…	Transmission Electron Microscopy
SIQU…	Submersive Interrupted Quench Unit

1.0 Introduction

The application of high strength low alloy steels (HSLA) has been the subject of extensive studies since the early 1970's for many different applications; one particular collective example are the vanadium-aluminum-nitrogen steels such as the VAN 80 HSLA steels developed by the former Jones and Laughlin Steel Corporation.[1] Prior to the development of HSLA steels, high strength forgings were achievable only through the application of a quenching and tempering (QT) process. This process was both uneconomical and detrimental to the environment through the necessity of extra processing steps.[2] However, 1974 through to 1980 saw the development of medium carbon steels which utilize the benefits of the microalloying elements niobium, titanium, and vanadium. The individuals who investigated these steels found that additions of these elements increased both the yield and ultimate strengths of the steels, with this effect being enhanced in the presence of accelerated cooling.[2] As can be seen in Figure 1, the processing of these steels is much simpler than the QT steels, and thus the economic viability of these steels is much higher.[2]

Recrystallization controlled rolling or forging (RCR or RCF) combined with interrupted direct quenching (IDQ)/ indirect accelerated cooling (IAC) is a technology which has been in development since the early 1980's. The attractive qualities of this technology are its uncomplicated nature, its elimination of normalizing steps, and its capability of application on unconventional forging plants.[3] The grain refinement achieved by RCR processing is central to increasing the toughness of these steels. Though this technology has been generally well accepted, the implementation of the RCR process in forging applications to create a new recrystallization controlled forging (RCF) process is relatively new, with a low-carbon, Nb microalloyed multiphase steel being designed for hot deformation under RCR conditions.[4]

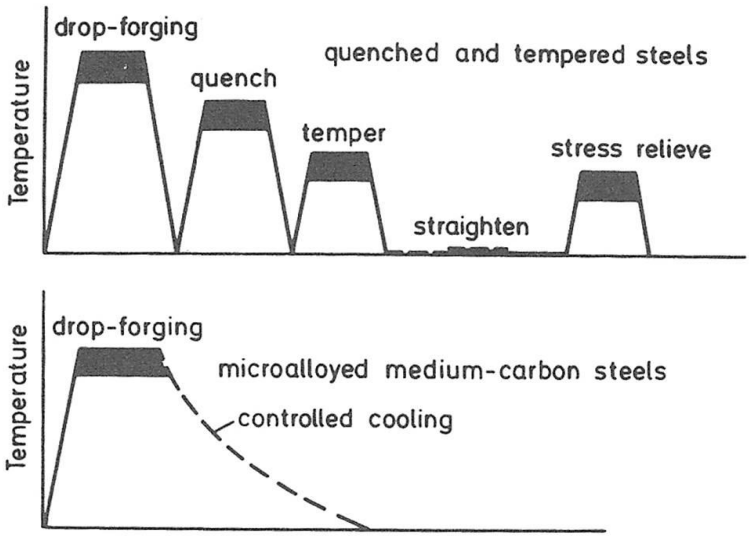

Figure 1: Processing path of quenched and tempered steel vs the processing path of microalloyed medium-C steels[2]

The principal goal of the research conducted herein was to implement various steel compositions designed for use in the recrystallization controlled forging system and implement several differing cooling conditions to provide a range of final microstructures with desirable strength and toughness combinations for automotive industry applications.

To accomplish this goal, laboratory characterization experiments were conducted. The first of these experiments, the grain coarsening experiments, determined the T_{GC} for each steel. Deformation experiments occurred next, determining both the post deformation austenite grain sizes, as well as the T_{95} for each steel. The final characterization experiments, the cooling experiments, determined cooling paths to achieve ferrite, bainite and martensite constituent microstructures. Upon completion of these experiments, hot water quench trials were conducted in order to generate a cooling path capable of forming bainite in the full forgings in the industrial scale trials.

The results of the characterization and hot water quench trials were used to design the full-scale forging trials, during which the MFC standard processing schedule was conducted. Following this processing schedule, the steels were cooled according to five differing cooling paths: ACRT, fan ACRT, WQRT, 27 second hot water quench, and 50 second hot water quench. The full forgings produced from these cooling paths were sectioned, and metallographic analysis occurred at five locations throughout the steel. Additionally, tensile and charpy v-notch samples were machined and tested from each of the full forging conditions. Finally, precipitation analysis was conducted in the steels, determining precipitate composition, shape and average size within the M3 fan ACRT condition.

2.0 Background

2.1 Strengthening Mechanisms

2.1.1 Strengthening Overview

Plastic deformation in steels occurs due to the motion of dislocations throughout the structure. Strengthening methods refer to methods of changing the structure and/or the local chemistry of the steel, to make it more resistant to the motion of these dislocations, and thus requiring of higher stress levels to force the motion of the dislocations. In such a manner, the yield strength of a steel can be adjusted, and can be expressed according to a generalized form shown below:[5]

$$\sigma_y = \sigma_0 + \sigma_{SS} + \sigma_{pptn} + \sigma_{dis} + \sigma_{texture} + \sigma_{GB} \quad (2\text{-}1)$$

Here σ_0 is the Peierl's-Nabarro stress, which quantifies the intrinsic resistance to dislocation motion in the perfect BCC Iron lattice, σ_{SS} is the solid solution strengthening contribution from solutes in solid solution in the ferrite, σ_{pptn} is the precipitation strengthening contribution from the fine precipitates that may reside in the ferrite matrix, σ_{dis} is the dislocation strengthening contribution from pre-existing dislocations present prior to the tensile test, $\sigma_{texture}$ is the texture hardening contribution resulting from the orientation dependent effects of the Schmidt factor Taylor factor and elastic constants, and σ_{GB} is the grain boundary strengthening contribution or Hall-Petch hardening. (i.e. $\sigma_{GB} \propto \frac{1}{\sqrt{d}}$ where d is the grain size)

2.1.2 Solid Solution Strengthening

Alloying elements which have not precipitated out of the matrix in which they were introduced into instead incorporate themselves into the host matrix and are said to be in solid solution. Depending upon the size and valence of the atom relative to the matrix atoms, these solute atoms can occupy either substitutional sites or interstitial sites in the matrix. If the solute and solvent atoms are similar in size, substitutional solid solution behavior occurs, and the solute atoms occupy the positions of solvent atoms. However, if the solute atoms are much smaller than the solvent atoms, interstitial solid solution behavior occurs. The elements which commonly form interstitial solid solutions are carbon, nitrogen, oxygen, hydrogen and boron. Typically, interstitial solid solutions produce strengthening effects which are 10-100 times more pronounced than that of the substitutional solid solutions.[5] In general, solute atoms in solid solutions affect the strength of the material through the creation of local distortions, which impede dislocation motion throughout the material.

2.1.3 Precipitation Strengthening

Precipitation strengthening is the method of increasing the strength of a material through the precipitation of compounds within the matrix. These precipitates impede the dislocation motion within the metal, and thus increase the strength. This increase in strength is dependent upon the individual precipitate characteristics, such as size, shape, and coherency with the matrix, as well as bulk characteristics, such as distribution and volume fraction of the precipitates. For this strengthening mechanism to be employed, the elements of the precipitate must be solid soluble at

higher temperatures, and also demonstrate decreasing solubility with temperature, such that they precipitate upon cooling.[6]

Dislocation motion within the metal may interact with the precipitate particles in 1 of 2 distinct ways, depending on the nature of the particles. When the precipitates are deformable by the moving dislocations, then the strengthening is described by the Friedel[7] process. Deformable particles tend to be small, soft and coherent with the matrix, and are mainly found in FCC systems such as aluminum, copper and nickel-based alloys. A schematic view of particle cutting is shown in Figure 2.[6] The extent of strengthening introduced due to this type of precipitation/dislocation interaction is dependent upon several strengthening mechanisms, including coherency strains and stacking-fault energies, among others.[6] In FCC systems, when the specimen has become overaged, and the precipitates present are either large and/or hard, dislocations react with the particles in another distinct manner. Figure 3 shows this second interaction method, which details the by-passing or looping of dislocation lines around harder precipitate particles, as found in BCC ferrite.[8] This Orowan-Ashby hardening mechanism also tends to dominate for incoherent particles.[8] In the case of microalloying precipitates in ferrite matrices, the particles are very hard, ordered intermetallic compounds which cannot be coherent with the ferrite matrix nor sheared by mobile dislocations. Therefore, microalloyed strengthening particles in ferrite follow the Orowan-Ashby by-pass mechanism of strengthening, illustrated in Figure 3.

The bypassing of a dislocation over a hard particle is explained in Figures 4 and 5. Here, dislocation slide/glide is shown in Figure 5 as (a), and dislocation climb is shown in Figure 5 as (b). As seen in Figure 4, these mechanisms allow for the motion of dislocations to overcome obstacles in the path of motion.

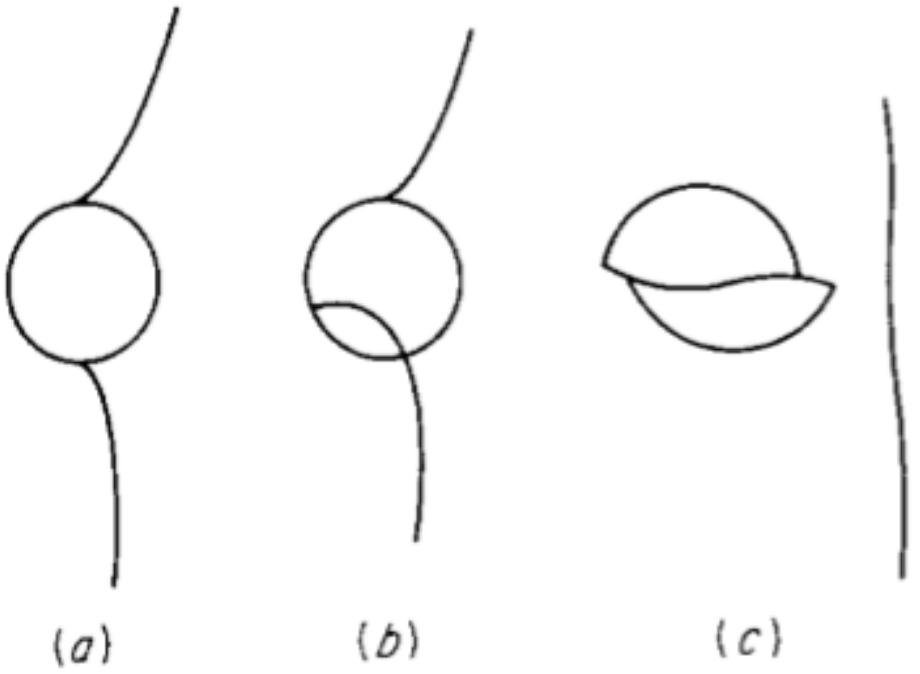

Figure 2: Dislocation cutting of a small, soft inclusion[6]

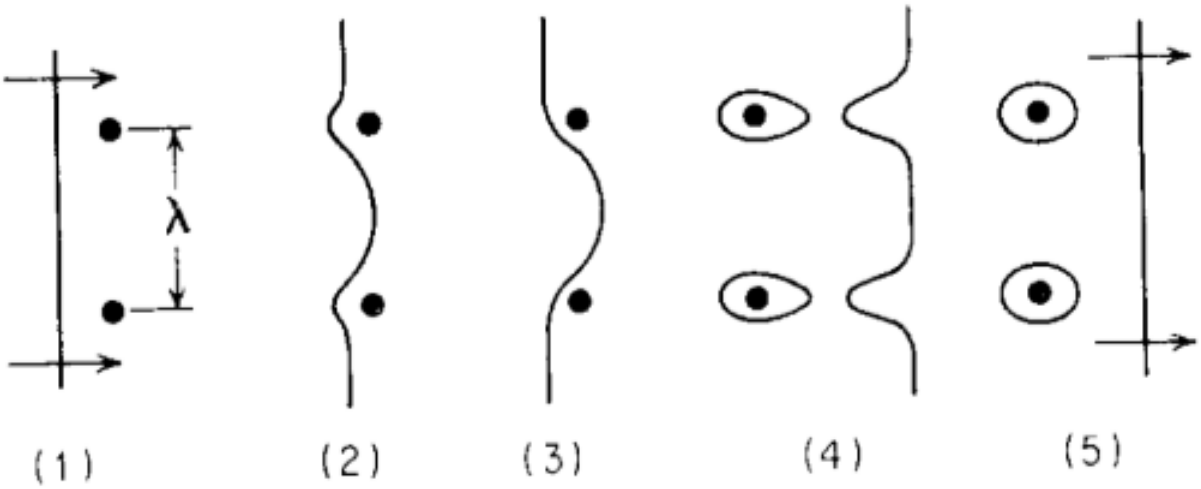

Figure 3: Dislocation bypassing of large, hard particles[8]

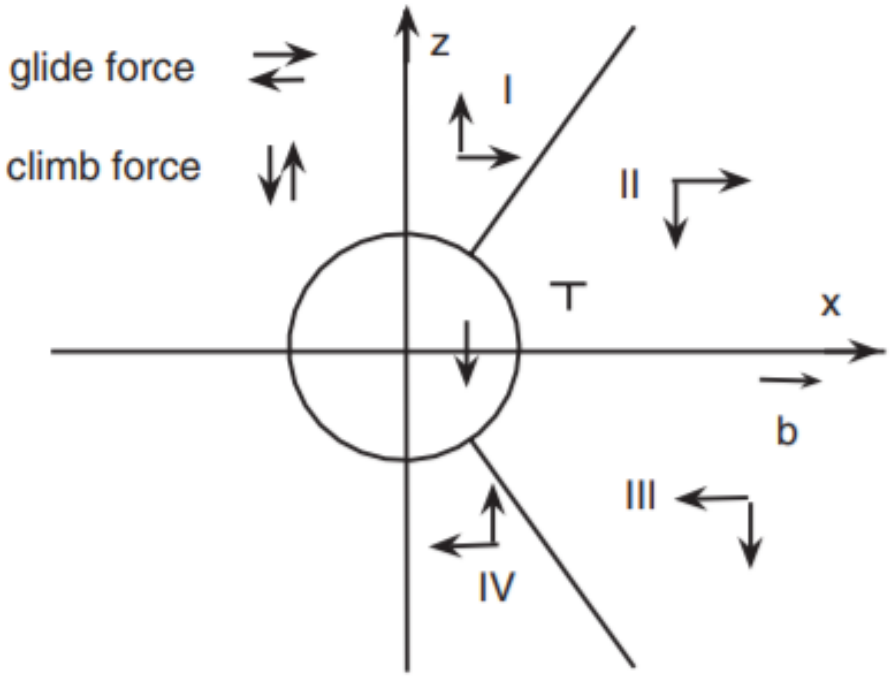

Figure 4: Model of dislocation and particle interaction showing glide and climb force directions[9]

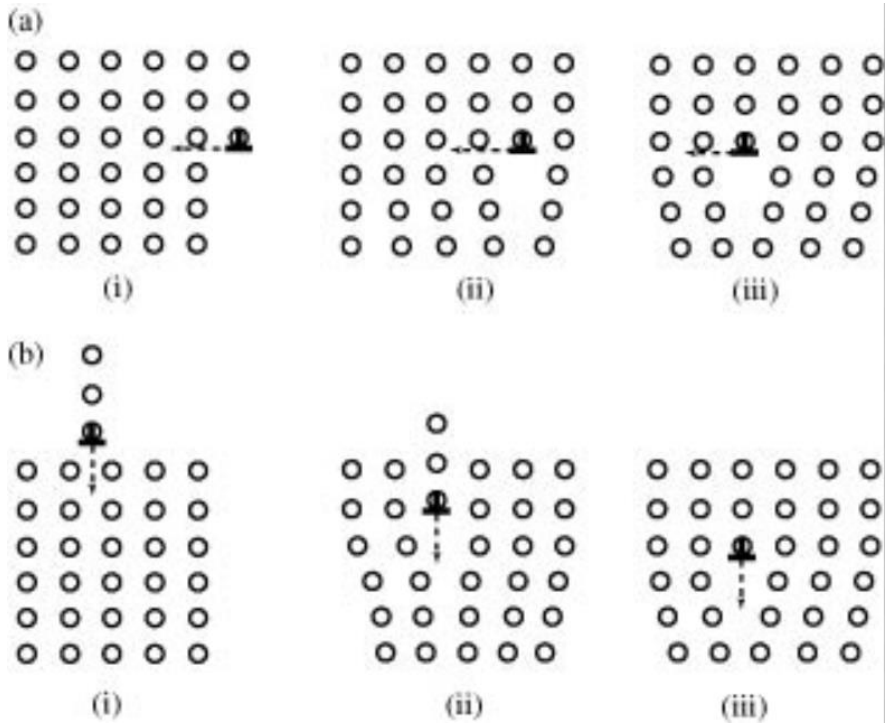

Figure 5: Dislocation model showing dislocation movement through (a) dislocation slide and (b) dislocation climb[10]

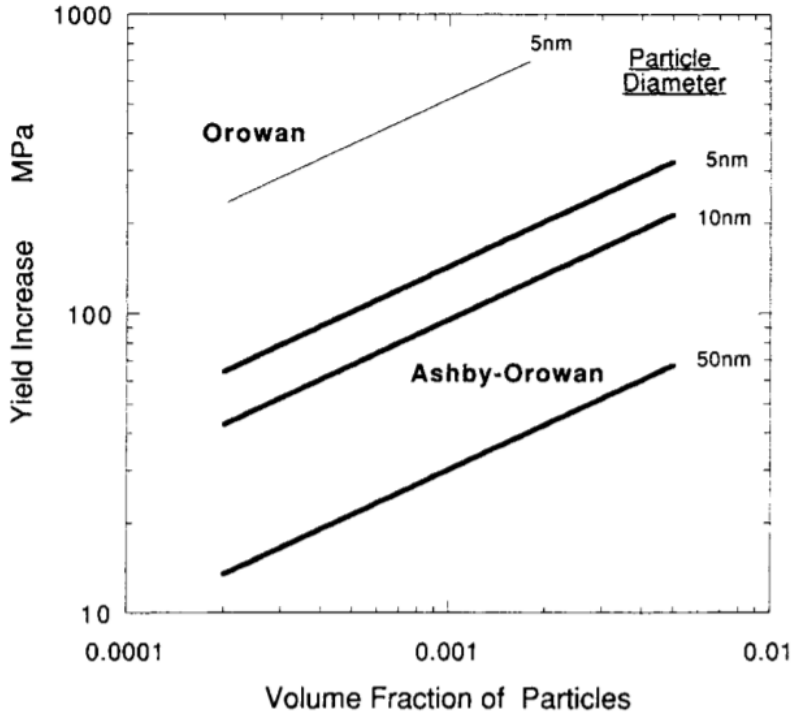

Figure 6: Precipitation strengthening relationship with particle volume fraction and size[11]

Figure 6 shows the relationship between the strengthening increment due to precipitation and the volume fraction and size of the precipitates. Here is demonstrated the importance of a fine distribution of precipitates, where particles approaching 5nm in diameter contribute very high strength increments exceeding 100MPa at very low volume fractions, while the larger particles at 50nm increase the strength moderately.

In the literature [11] the strengthening increment of a particle distribution is described by

$$\Delta\sigma_y = (0.538Gbf^{1/2}/X)\ \ln(X/2b) \qquad (2\text{-}2)$$

Where $\Delta\sigma_y$ is the yield strength change due to precipitation (MPa), G is the shear modulus (MPa), *b* is the burgers vector (mm), *f* is the volume fraction of particles, and X is the real (spatial) diameter

of the particles (mm).[11] Of importance to note here is the relationships between the aspects of the precipitation and the strength. Specifically, the strengthening increment increases with the square-root of the volume fraction of the particles, while the strength increase decreases as the real diameter of the particles increases.

Precipitation strengthening can be highly desirable in many high-strength applications, and as such, an aging time is often incorporated into the processing of the steel to allow for sufficient precipitation. However, as Figure 7 shows, when too long of a time is allotted for aging, negative effects tend to take place.[6] The precipitates begin to lose coherency with the matrix such that the Friedel mechanism cannot operate, and furthermore the growth of the particles leads to decreasing strengthening increments in the Orowan-Ashby machanism.[6]

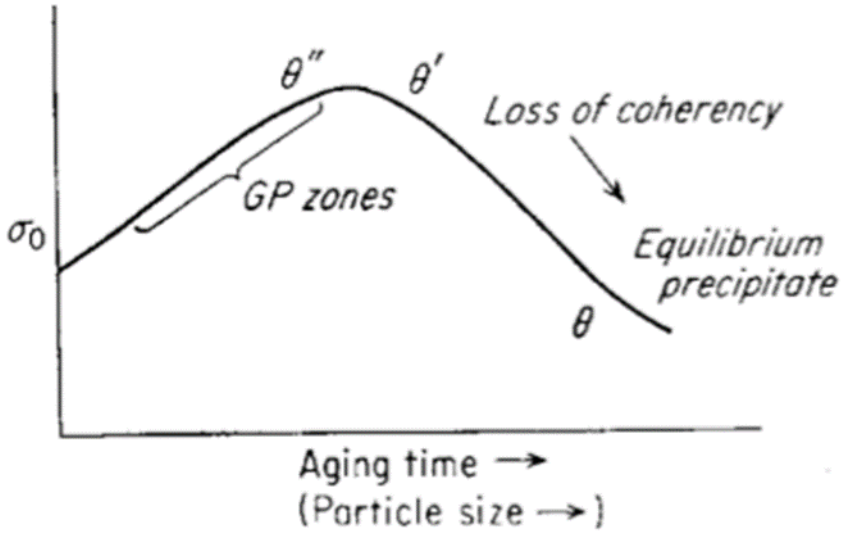

Figure 7: Aging time and particles size influence on precipitation strengthening[6]

2.1.4 Grain-Boundary Strengthening

The presence of grain boundaries within a metal provides resistance to the motion of dislocations throughout the structure. While the grain boundary itself has little inherent strength, the boundaries give rise to significant strengthening through interference to slip within and between the grains, such that the strengthening scales with the misorientation across the grain boundary.[6] This strengthening effect increases with the ASTM grain boundary numbers, and thus also scales inversely with the grain size, according to the following equation proposed by Hall and expanded by Petch:[12, 13]

$$\sigma_0 = \sigma_i + kD^{-1/2} \tag{2-3}$$

Where σ_0 is the yield stress, σ_i is the friction stress, k is the locking parameter which describes the strengthening contribution of the grain boundaries, and D is the grain diameter.[6]

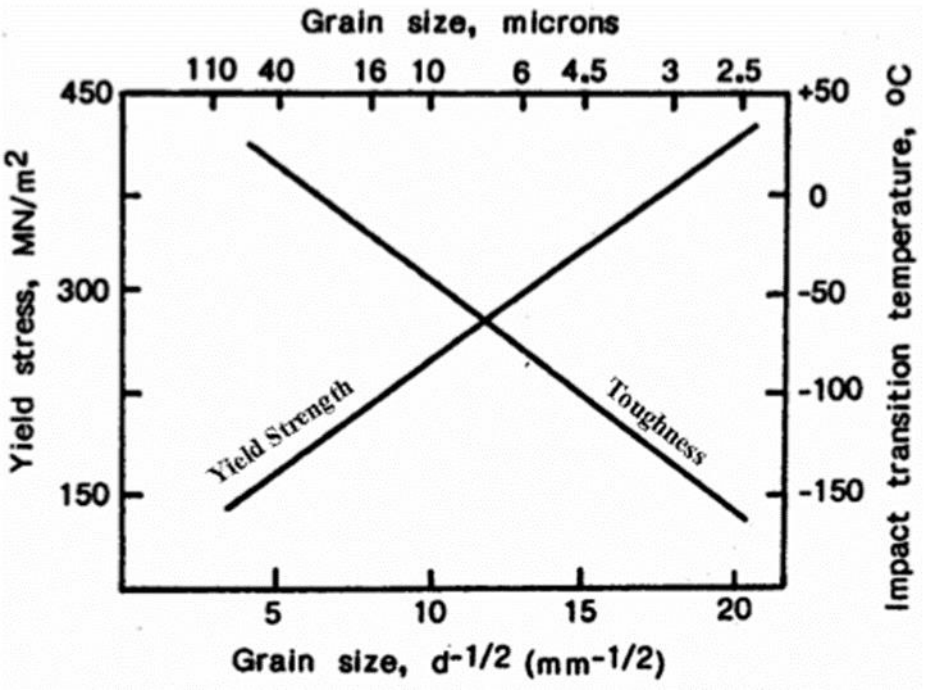

Figure 8: Influence of grain size upon strength and toughness[5]

While many strengthening mechanisms tend to decrease the toughness of the material when the strength is increased, grain boundary strengthening is considered highly desirable because a reduction in grain size increases both the strength and toughness of the material, as can be seen in Figure 8 above.[5] Because of this, the primary focus of RCF conditioning is to reduce the final grain size, to produce concurrently high strength and high toughness steel forgings.

2.1.5 Dislocation Strengthening/Work Hardening/Strain Hardening

As dislocations are imperfections in the stable structure of a material, they cause distortions in the matrix surrounding them. These distortions result in stress fields in the areas surrounding them, and these stress fields produce forces between dislocations and other dislocations.[6] Due to these interactions between dislocations, the difficulty with which dislocations traverse the matrix,

and thus the strength of the material, scales with the dislocation density in the metal. As dislocations have no thermal equilibrium value, such as exists for vacancies in the metal, the dislocation density in a metal may be widely varying, from 10^6 dislocation lines per square centimeter to 10^{12} dislocations lines per square centimeter, depending upon the prior history of the material.[6]

Dislocation strengthening is the process of increasing the dislocation density within the metal, typically using cold working at temperatures below half the melting point of the steel. Dislocations can also result from transformation of austenite to ferrite, because of both the volume change and the nature of the transformations. The formation of polygonal ferrite is considered a reconstructive transformation, and therefore leads to moderate increases in dislocation density. However, bainite and martensite formations are considered displacive in nature, occurring by shearing of the austenite. These transformations can lead to very high dislocation densities. Figure 9 shows the influence of cold working upon the physical properties of the metal. In general, the dislocation density contribution to the flow stress of the material is related to the structure through the following relation:[6]

$$\sigma_0 = \sigma_i + \alpha G b \rho^{1/2} \qquad (2\text{-}4)$$

Where σ_0 is the flow stress, σ_i is the base stress of the lattice, α is a constant, G is the shear modulus, b is the burger's vector, and ρ is the dislocation density in the metal.

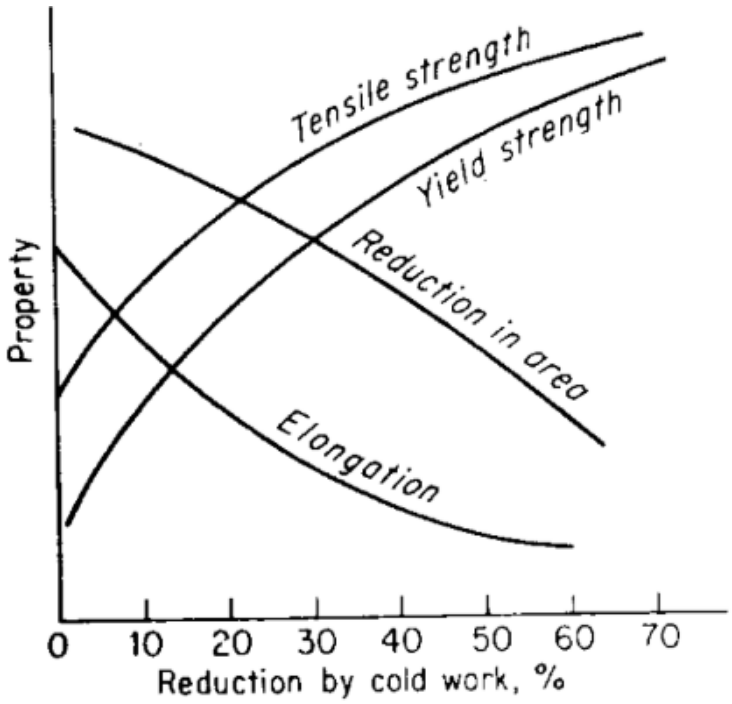

Figure 9: Influence of cold working on physical properties[6]

While dislocation strengthening increases the yield strength of a material, this benefit is usually accompanied by several negative influences, such as decreases in ductility and chemical effects such as decreases in electrical conductivity and corrosion resistance.[6]

2.2 Composition and Alloying

2.2.1 BAMPRI, Meadville Forging Company, TIMKENSTEEL Steel Company

Composition

In microalloyed steels, varying the concentration of elements can have significant influences on the performance of the steel, even when this change is on the order of as little as

.01wt%, as is shown in the article by Hua et al.[1], where small deviations in composition have significant impacts on important parameters, such as the T_{95} temperature. Table 1 lists the nominal compositions of the steels that will be studied in this thesis project. Each element in these steels plays a role in altering various properties, such as strengthening mechanisms and hardenability.

In Table 1, note that the steels M1, M2 and M3 are the steels designed specifically for the RCF processing schedule, steel 10V40 is the current steel in use at Meadville Forging Company, and steels T1 and T2 are TIMKENSTEEL Steel Company commercially available steels, suggested for testing in the project by TIMKENSTEEL Steel Company personnel.

Additionally, note that the D_I value in Table 1 represents the Ideal Diameter, a measure of determining the hardenability of a steel according to ASTM A255-02. This value represents the maximum diameter of a rod with a center microstructure consisting of 50% martensite volume fraction. The value is calculated from a summation of factors depending upon the alloying and the prior austenite grain size. For this project, a prior austenite grain size of ASTM grain size number 7 (average equivalent circular grain diameter equal to approximately 30μm) was used.

Table 1: Nominal compositions of BAMPRI steels M1, M2 and M3, Meadville 10V40 steel, and TIMKENSTEEL steels T1 and T2

Element/Steel	M1	M2	M3	10V40	T1	T2
C (wt%)	0.10	0.10	0.10	0.37	0.15	0.20
V (wt%)	0.06	0.060	0.12	0.060	0.080	0.11
Ti (wt%)	0.015	0.015	0.015	-	0.003	0.003
N (wt%)	0.012	0.012	0.012	0.0094	0.009	0.009
Cr (wt%)	0.50	0.25	0.50	0.10	0.10	0.10
Mo (wt%)	0.30	0.15	0.30	0.02	0.030	0.030
Mn (wt%)	1.20	1.20	1.20	1.14	1.35	1.50
Si (wt%)	0.40	0.40	0.40	0.22	0.20	0.30
P (wt%)	0.010	0.010	0.010	0.010	0.010	0.010
Al (wt%)	0.030	0.030	0.030	0.028	0.030	0.030
S (wt%)	-	-	-	0.016	-	-
Ni (wt%)	-	-	-	0.05	-	-
Cu (wt%)	-	-	-	0.12	-	-
D_I (cm)	3.86	2.18	4.19	3.99	2.04	3.43

2.2.2 Carbon

Carbon is perhaps the oldest alloying element in iron and is the defining addition in the widely-used carbon steels. Carbon displays one of the largest solute strengthening capacities of any element, with the slightest additions returning significant strengthening increments. Additionally, C contributes to the precipitation strengthening of the material, through formation of carbide precipitates. One form of precipitate shown in the literature are precipitates of the type V(CN), shown by Siwecki and Engberg.[14] Furthermore, higher concentrations of C in the steel favor formation of alternative phases over ferrite, allowing for various microstructures such as bainite and martensite to form more easily, providing a range of possible mechanical properties. High levels of C, however, also have a significant, negative influence on the toughness of the steel, thus limiting the amount of carbon strengthening a steel designer can practically employ for a given application.

Additional consideration of C in the steels studied herein must be taken to determine the effect upon the forging loads during hot deformation of the steel, a factor which directly influences the economic viability of the steel through die wear. These factors were studied by Wei et al.[15], and the results are summarized in Figure 10 below in the form of flow stress curves from a hot compression test at 1000°C, the expected region of hot deformation for the steels presented herein. These curves show that for the higher tested strain rates of $10s^{-1}$ and $1s^{-1}$, which among the tested strain rates more closely resemble the strain rates anticipated in the present experiment, a lower C concentration is seen to lower the hot flow stress, and thus positively influence the economic viability of the steels by reducing die wear.

In the V-Ti-N steel studied herein, the optimal carbon concentration seen throughout the literature is in the proximity of 0.1 wt%. Lower levels of C, while detrimental to the steel strength,

increase the steel toughness by decreasing the amount of pearlite formations. It is well known that pearlite is detrimental to ductility and toughness.[16] This is paramount in these steels, as the low toughness of the steels is the principal cause of failure in the final pieces. All steels present in a study by Siwecki[3] had C concentrations in the region of 0.09 to 0.14 weight percent. Also, the steels utilized in the recrystallization controlled rolling experiments by Zheng et al.[17] comprised of C concentrations of 0.07 and 0.08 weight percent. Similarly, the majority of the literature concerned with recrystallization-controlled rolling in the V-Ti-N steel system shows C concentrations above a minimum of 0.07 weight percent C, with only Chen et al.[18] using a concentration lower than this, with a carbon weight percent of 0.051.

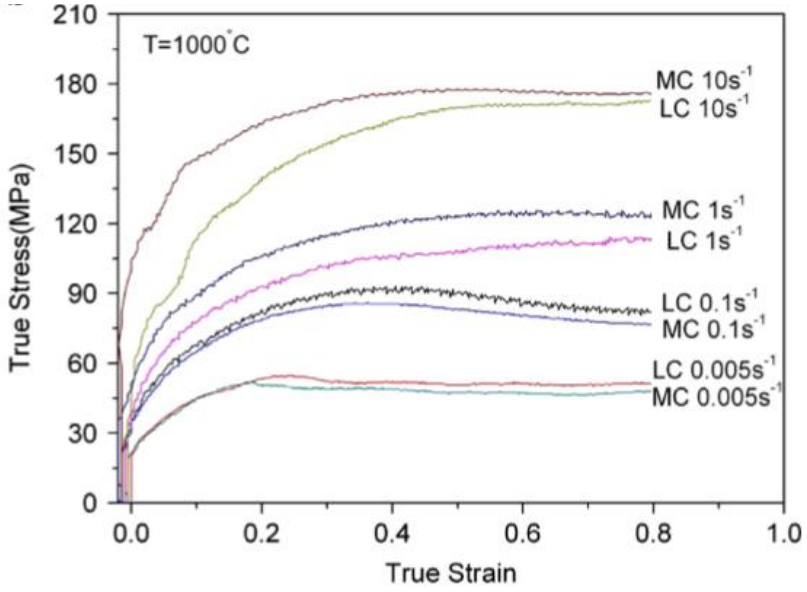

Figure 10: Flow stress curves of MC (Medium-C) and LC (Low-C) Vanadium microalloyed steels with varying strain rates[15]

2.2.3 Vanadium

Vanadium is a prominent microalloying addition, being potentially involved with austenite conditioning, hardenability, and precipitation hardening of the final microstructure. The primary purpose of V in the steels proposed herein is to supply a substantial quantity of precipitation strengthening. Vanadium carbides may form in the steel under suitable transformation and cooling conditions, but in the presence of sufficient quantities of N, vanadium nitride precipitates may form and substantially increase the strength even more.[14] However, since in the current experiments the N content is kept constant at approximately 60 ppm, this may not be a factor.

An additional benefit of V additions in the Ti-V-N steels studied in the literature is the refinement of the final microstructure through the intragranular nucleation of ferrite upon inclusions, especially the V precipitates which form on MnS inclusions.[19] Traditionally, ferrite nucleation during the austenite to ferrite transformation occurs predominantly upon the prior austenite grain boundaries. With the increased nucleation rates from the intragranular nucleation of the ferrite, a higher quantity of individual ferrite grains is formed, and thus an overall smaller ferrite grain size is observed.[19] These methods of intragranular ferrite nucleation upon inclusions in V-bearing steels were studied by several authors[20-22] and were found to be effective means of refining the final microstructure of the steel.

2.2.4 Titanium

Titanium is the other prominent microalloying element in the proposed steels. The role of Ti is primarily in the control of austenitic grain size, through the Zener pinning of austenite grain boundaries by stable, high-temperature TiN precipitate particles.[17] These TiN particles, when

subjected to proper conditions, can significantly lower the potential for grain coarsening, providing the optimal conditions for recrystallization controlled forging.

With regards to austenite conditioning and control, an addition of Ti to a N containing alloy results in the high temperature precipitation of TiN particles, which pin austenitic grain boundaries and impede growth, significantly raising the grain coarsening temperature.[17] These TiN particles were observed by various authors in the literature, and are well documented to be a key austenitic conditioner.[14, 17, 23-26] TiN particles also have a significant effect upon the recrystallization kinetics of the steel, which is a very core component in the recrystallization controlled forging process proposed. Zheng et al.[17] demonstrated that additions of Ti to the V and N steels resulted in a depressing of the recrystallization temperature. Figure 11 below demonstrates both the effects of Ti on the grain coarsening and recrystallization temperatures, and the effects of the N level, which will be explained shortly.

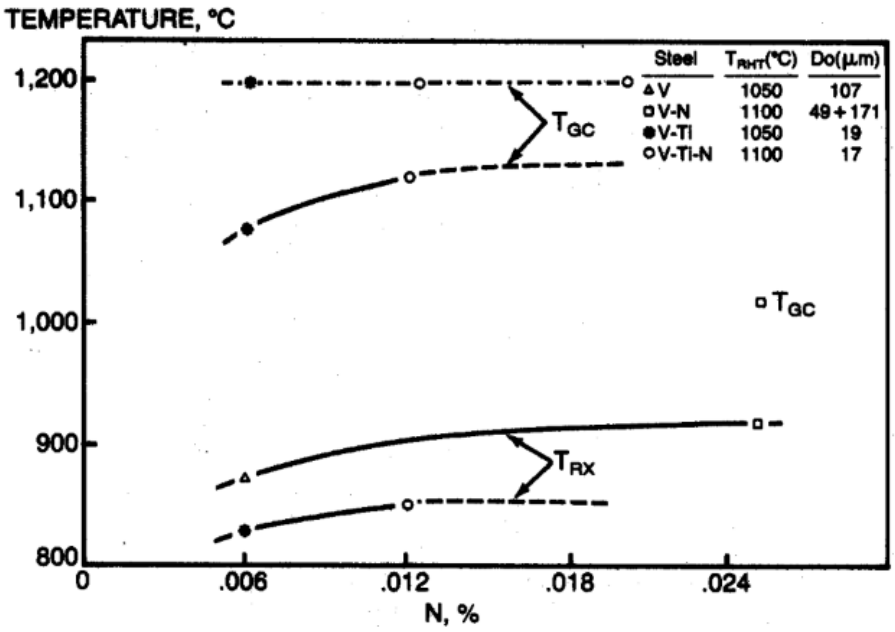

Figure 11: Influence of N composition and Ti resence on the grain coarsening and recrystallization temperatures in a V microalloyed steel[17]

Though Ti has a very positive effect on the conditioning of the austenite in the RCF process, the composition of the element is limited practically due to coarsening of the TiN particles. For the grain size control to be most effective, the dispersion of the TiN particles should be very fine.[14, 27] Such a small distribution is achievable through adjusting the Ti/N ratio in the composition. As Ti is a slower diffusing element than N, limiting the quantity of Ti in the steel to a hypostoichiometric Ti/N ratio (Ti < 3.42N) will limit the coarsening of the TiN particles. Such was confirmed in the literature by several authors.[14, 17, 24-28]

The key role of titanium in the steels, as stated, is the formation of fine TiN precipitation, in order to pin austenite grain boundaries at high temperatures, preventing austenite grain growth in the steels. The pinning pressure of a precipitate distribution in steel is dependent on several variables, shown in the rigid boundary model, which assumes a fully rigid austenite boundary, allowing for no flexibility: [29-33]

$$F_{PIN}^{R} = \frac{6\,\sigma\,f_{\mathrm{v}}}{\pi\,r} \tag{2-5}$$

Where σ = 0.8 J/m^2 in austenite [34], f_{v} is the volume fraction of precipitates, and r is the average particle radius. Other derived pinning models include the flexible boundary model,[30, 35] which assumed an infinitely flexible boundary which interacted with all particles in the steel until completely pinned, and the subgrain boundary model,[30, 36] which considered the impact of the interactions of austenite subgrain boundaries and precipitates:

$$F_{PIN}^{F} = \frac{3\,\sigma\,{f_{\mathrm{v}}}^{2/3}}{\pi\,r} \tag{2-6}$$

$$F_{PIN}^{S} = \frac{3\,\sigma\,f_V\,l}{2\,\pi\,r^2} \quad (2\text{-}7)$$

Where l is the average austenite subgrain intercept in the microstructure.

The overall effect of the Ti in the system can be seen in Figure 12 below, which is taken from the work of Zheng et al.[17] This figure shows the effect of additions of N and Ti to a V steel on the austenitic grain size and the grain coarsening behavior of the steel.

2.2.5 Nitrogen

Nitrogen's effect on the processing of the steel lies primarily in its interactions with, and its capability to enhance the effects produced by the microalloying additions in the steel, primarily Ti and V. As can be seen in Figure 11 and Figure 12 from Zheng et al.[17], an increase in the quantity of N in the steel enhances the austenitic refinement benefits of the Ti. N enhances the grain coarsening reduction of Ti through manifestation of a finer distribution of TiN precipitates in the steel.[14, 17, 24-28, 37]

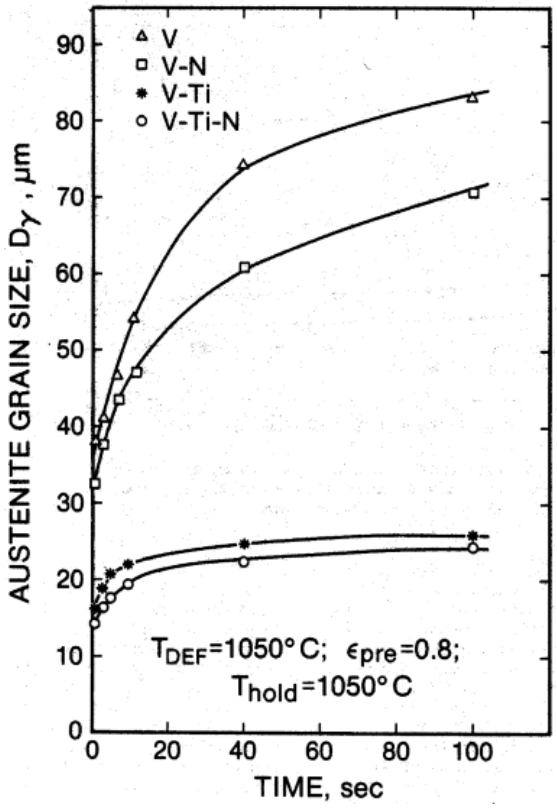

Figure 12: Influence of N and Ti presence upon the austenite grain size and coarsening behavior of the tested steels[17]

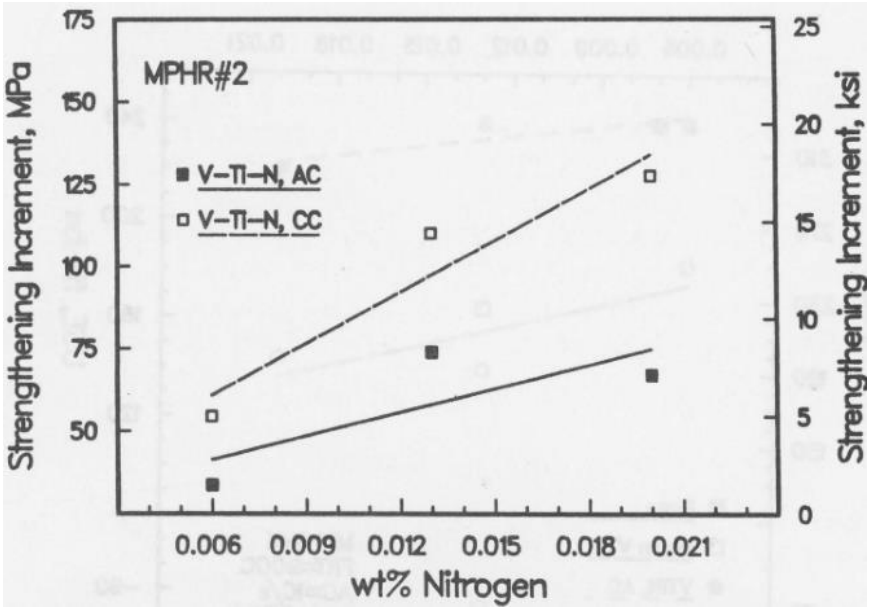

Figure 13: Influence of N content on precipitation hardening[37]

N also enhances the benefits of the V additions, which has its precipitation strengthening increments augmented at higher levels of N. This fact is clearly observed in Figure 13, from Fix et al.[37] Similar strengthening effects of N are observed by several other authors in the literature.[1, 14, 17]

Medina et al.[20] also suggested that increasing quantities of N, when coupled with V, would also help to increase the extent of intragranular nucleation of ferrite due to the increased presence of VN precipitates on MnS particles. This additional nucleation of ferrite grains would result in a further refined final ferritic microstructure.

2.2.6 Vanadium and Titanium Precipitates: Solubility and Influences

Within the V-Ti-N steel system utilized in the experiment proposed herein, V and Ti form several precipitate phases which heavily influence the performance of the steel. Principal among these precipitates regarding the properties of the steel are TiN, VN, and VC. Titanium nitride in the system is utilized as the primary method of suppressing grain coarsening during the high temperature processing of the steel in the austenite temperature regime. [3, 14, 17, 18, 24, 37] Vanadium nitride serves the primary roles of increasing the nucleation rate during the transformation from austenite to ferrite, through the provision of an increased quantity of heterogeneous nucleation sites, as well as an increase in the precipitation hardening of the steel. [1, 19, 20, 38] Finally, vanadium carbide provides significant precipitation strengthening for the system when present in the form of a wide distribution of fine particles; However, this strengthening, as all precipitation strengthening methods, comes at the cost of a reduction in the toughness of the steel.[38, 39]

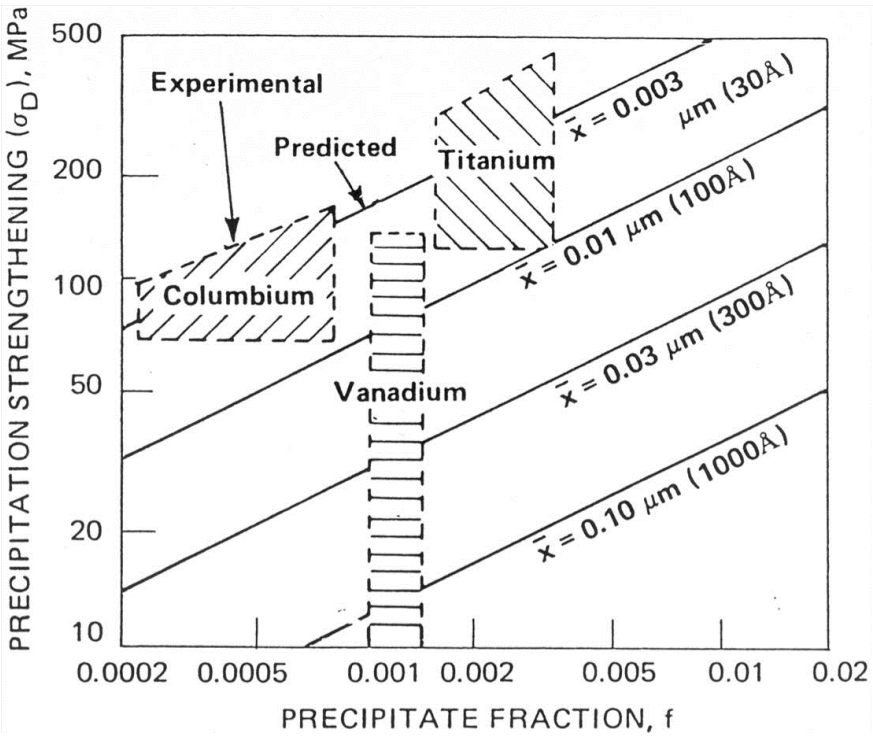

Figure 14: Impact of precipitate and size on precipitation strengthening increment for 3 common precipitating elements[40]

The relative precipitation strengthening effects of niobium (columbium), vanadium and titanium are shown in Figure 14. Here, all three microalloying additions are shown to be capable of significant strengthening increases. Additionally, Figure 14 shows the benefits of fine precipitation over large precipitation, reiterating the need for proper control of Ti and N in the steels. Here it is shown that higher strengthening increments are achieved for finer precipitation distributions.

Similarly, Figure 15 shows the grain size impact of precipitation distributions varying in volume fraction and particle size. Here, the lines descending to the right represent distributions of equal particle sizes, but with higher volume fractions as they go to the right. This effect is simple, since the higher quantity of precipitates provides higher levels of grain pinning to resist grain

coarsening. Also seen in this figure is again the impact of the finer precipitation distributions. Here, smaller precipitate sizes produce finer microstructures than the coarser particles of equal particle volume fractions.

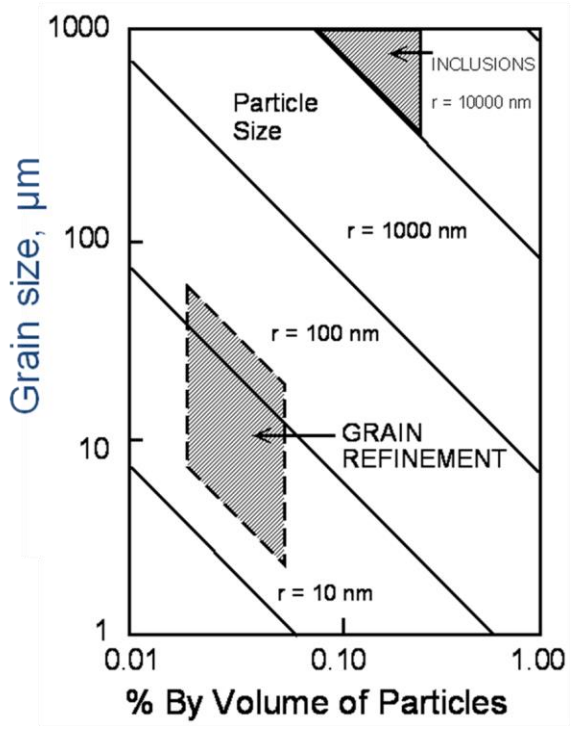

Figure 15: Impact of precipitate volume fraction and particle size on the grain size in steel[41]

The roles of each of these three primary precipitates in the system are predominantly derived through the relative solubility products of the respective precipitates, and the ratio of the constituent elements relative to the stoichiometry of the compounds. In this regard, Figure 16 and Table 2 have been included, and elucidate the range of precipitation for each precipitating compound. [39, 42, 43]

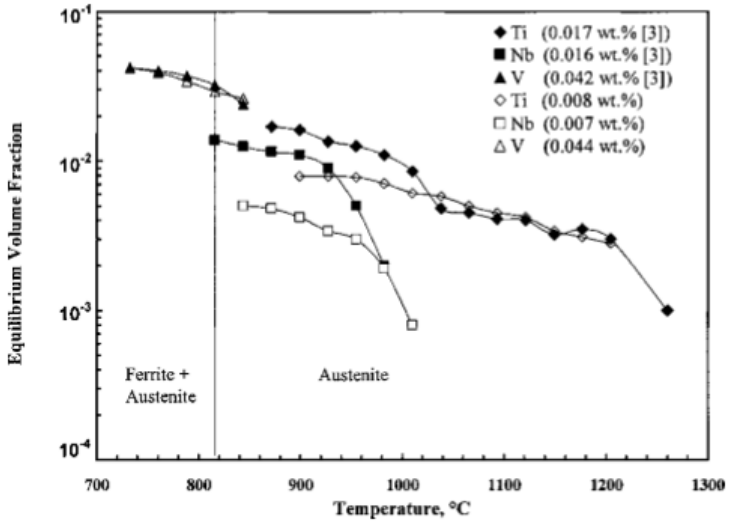

Figure 16: Precipitation of microalloying elements vs temperature[39, 43]

Table 2: Empirical solubility products of microalloying precipitates[39, 42]

Type of precipitate	Precipitate	Solubility product	Temperature range, °C/ phase	Reference
Nitrides	VN	log [V][N] = 3·4 –330/T+ 0·12(% Mn)	870–1480 Austenite	1
	NbN	log [Nb][N] = 2·8–8500/T	870–1480 Austenite	1
	TiN	log [Ti][N] = 3·82–15020/T	870–1480 Austenite	1
		log [Ti][N] = 5·9–16586/T	>1480 Liquid Steel	1
Carbides	VC	log [V][C] = 6·72–9500/T	870–1480 Austenite	1
		log [V][C] = 8·05–12265/T	480–815 Ferrite	1
	NbC	log [Nb][C] = 3·42–7900/T	870–1480 Austenite	1
		log [Nb][C] = 5·43–10960/T	480–815 Ferrite	1
	TiC	log [Ti][C] = 5·33–10475/T	870–1480 Austenite	1
		log [Ti][C] = 4·4–9575/T	480–815 Ferrite	1

As Figure 16 shows, with decreasing temperature, the first element in the steel to experience precipitation with falling temperature is Ti, which begins to form well before the other microalloying elements.[39] Titanium nitride, which has a much lower solubility product than titanium carbide in the austenite region, has a complete dissolution temperature which exceeds the dissolution temperature of all other microalloying carbonitrides, and the melting temperature of the steel.[38] For example, evaluation of the empirical solubility products in Table 2 determines the solubility product of TiN in austenite at 1000°C to be $[Ti\%][N\%] = 1.05*10^{-8}(wt\%)^2$ and the

solubility product of TiC in austenite at 1000°C to be [Ti%][C%] = $1.26*10^{-3}(wt\%)^2$, thus demonstrating a much lower precipitation potential for TiC in austenite.[42] In Figure 16, it can also be seen that V does not begin to precipitate until the temperature has entered the austenite to ferrite transformation regime.[39] Additionally, the solubility products of VN and VC can be calculated from Table 2 to be $1382.8(wt\%)^2$ and $0.181(wt\%)^2$ respectively, demonstrating that precipitation in austenite is unfavorable for the compositions proposed herein.[42] It should be noted that experiments in the literature have shown the presence of chromium to decrease the chemical activity of N, and thus decrease the solubility product of the VN.[44]

Stoichiometric ratio of TiN gives a Ti:N mass ratio equal to 3.42.[45] As titanium nitride begins to precipitate well before the other nitrides and carbides, there is a consequential depletion of Ti within solid solution, which reduces the formation of TiC to a small fraction.[39] Following the depletion of the Ti, the excess N then combines with the V in solid solution to form VN, which has a lower solubility in austenite than that of VC, which has a considerably higher solubility than any other microalloy carbide or nitride.[39] If the V concentration is greater than the stoichiometric ratio compared to the excess N remaining in solid solution ([V%] / [excess N%] > 3.64), then VN will precipitate until the depletion of the N in solid solution. In this super-stoichiometric condition, the excess V remains in solution for interphase precipitation or precipitation after transformation as vanadium carbides.[39]

The importance of ensuring a fine precipitation of TiN is best illustrated through a consideration of the Zener pinning model. Included in Figure 17 is an illustration of the interaction of a spherical particle with a grain boundary. The maximum force a particle of this size can produce, designated the Zener pinning force, is calculated by:[46]

$$F_z = \pi r \gamma \quad (2\text{-}8)$$

Where r is the radius of the individual particle and γ is the energy per unit area of a grain boundary. Analysis of this equation shows a direct relation between particle size and Zener pinning force of a particle in a 1 to 1 ratio. However, although individual particles will have a larger Zener pinning force at larger radii, the total Zener pinning forces present in the steel is a summation of the Zener pinning force of all individual particles, whose summation of volumes must necessarily equal the total volume fraction of the particles in the steel. Since the Zener pinning force of the particle increases linearly, and the volume of a particle increases in the third degree with respect to the radius of the particle, at equivalent volume fractions, the total Zener pinning force present in the steel increases as the average particle size decreases. Thus, as stated, a fine dispersion of TiN precipitation is more effective in pinning austenite grain boundaries, further supporting the necessity of a substoichiometric Ti/N ratio.

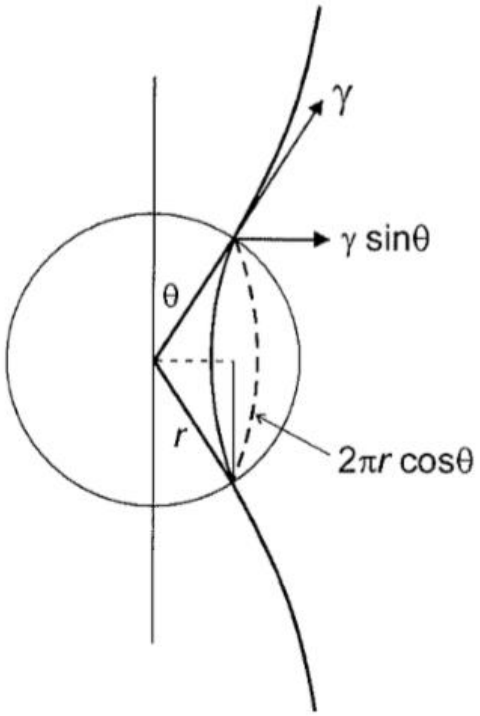

Figure 17: Schematic diagram of the interaction of a spherical particle with a grain boundary[46]

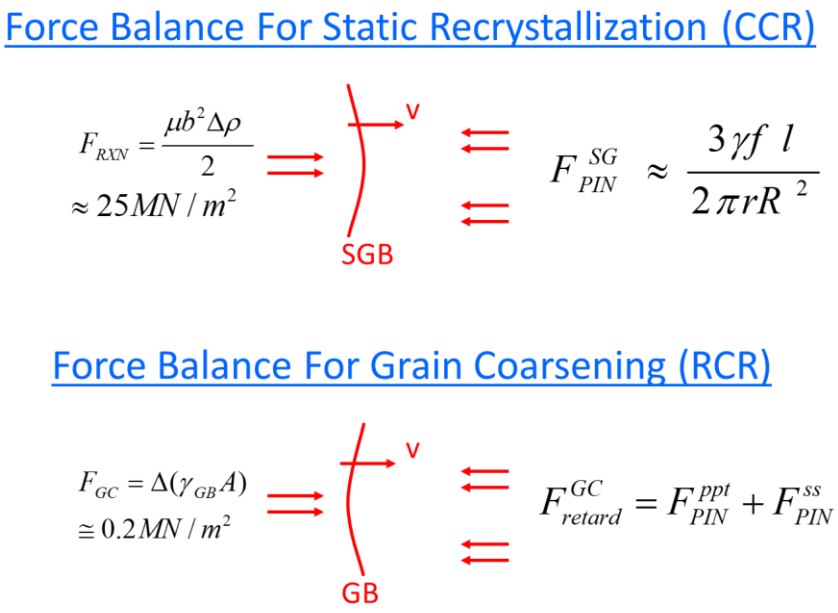

Figure 18: Forces in steel driving and opposing recrystallization and grain coarsening processes[1, 47, 48]

Figure 18 shows the relevant driving forces for recrystallization and grain coarsening. In the top of this figure is shown on the left the driving force for recrystallization, and on the right the pinning force generated by a distribution of precipitate particles. In recrystallization suppression, these driving forces are equivalent, or the pinning force exceeds the driving force for recrystallization. In the bottom of this figure is shown on the left the driving force for grain growth, and on the right the summation of forces opposing grain growth. In order to avoid grain growth, the sum of the precipitation pinning and solid solution pinning forces must exceed or equal the grain growth driving forces. Optimally, in the RCR process the pinning force of the particles exceeds the driving force for grain growth, without exceeding the grain growth for recrystallization:

$$F_D^{GC} < F_{PIN} < F_D^{RXN} \tag{2-9}$$

In analyzing precipitation in steels, one final aspect is of interest. When precipitates form in steel, they commonly form in a specific orientation, with respect to the phase they precipitated within. The first of these orientation relationships is labeled the Baker-Nutting orientation relationship.[49] This orientation relationship is defined by the following parameters:

$$\{100\}\ \alpha - Fe \ ||\ \{100\}\ precipitate \tag{2-10}$$

$$\langle 011\rangle\ \alpha - Fe \ ||\ \langle 010\rangle\ precipitate \tag{2-11}$$

The presence of this orientation relationship implies that the precipitate in question precipitated in the ferrite in the steel. A second common orientation relationship is labeled the Kurdjumov-Sachs orientation relationship.[50] This orientation relationship is defined by the following parameters:

$$\{110\}\ \alpha - Fe\ ||\ \{111\}\ precipitate \tag{2-12}$$

$$\langle 111\rangle\ \alpha - Fe\ ||\ \langle 110\rangle\ precipitate \tag{2-13}$$

The presence of this orientation relationship implies that the precipitate in question precipitated in the austenite in the steel.

Figure 19 shows a sample Baker-Nutting orientation relationship between a precipitate and a ferrite matrix.[51] Additionally, Figure 20 shows a schematic diagram of the rotation transformation which occurs during the austenite to ferrite transformation.[52] This rotation allows for the orientation relationship present between the austenite and the precipitate to remain detectable through the austenite to ferrite transformation.

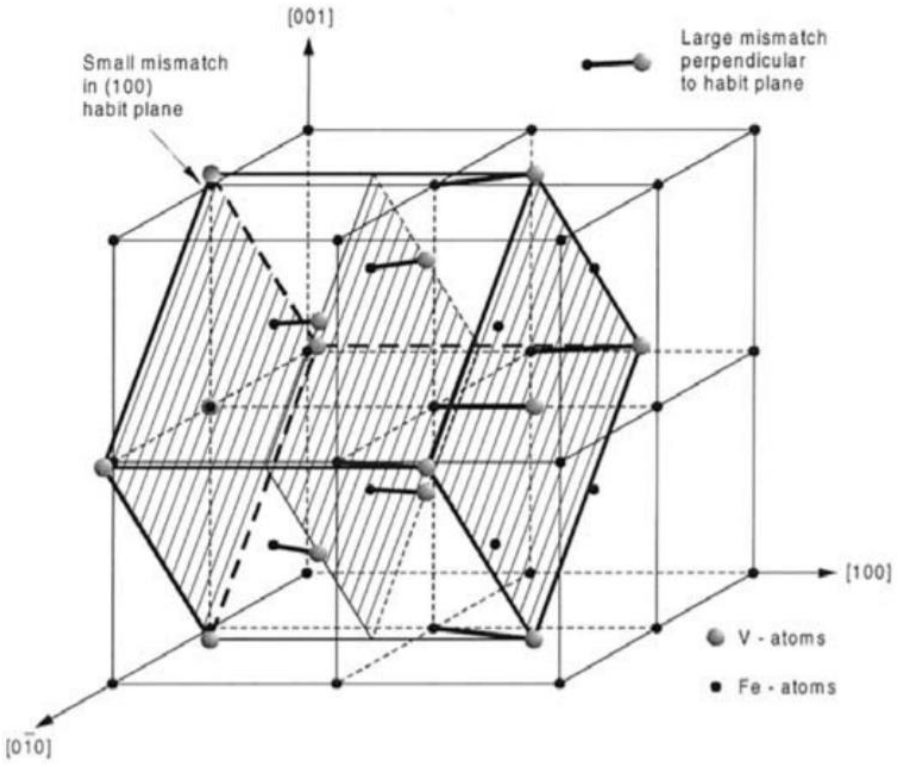

Figure 19: Schematic diagram of Baker-Nutting orientashion relationship[51]

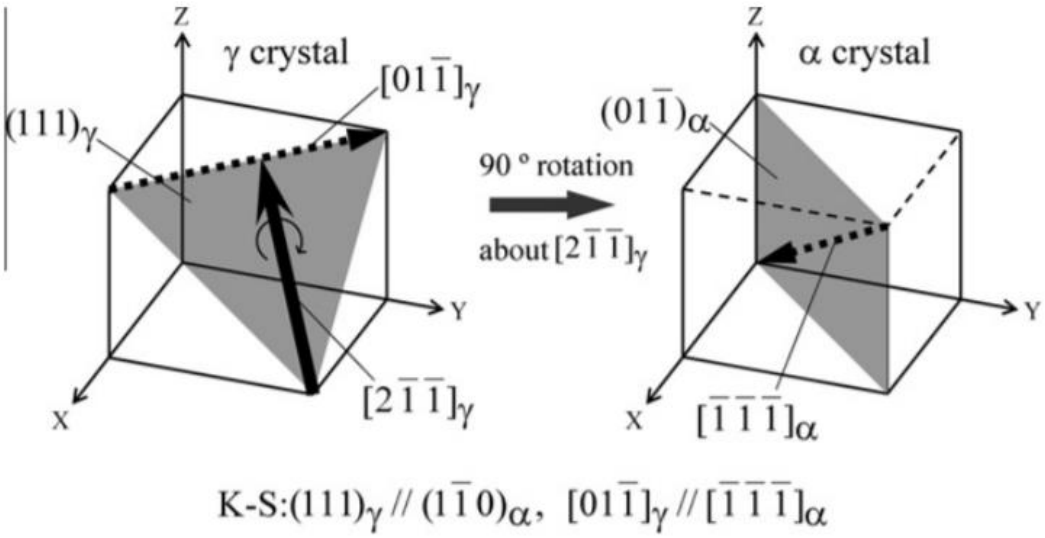

Figure 20: Schematic diagram of rotation of austenite to ferrite transformation, allowing for retention of austenite-precipitate orientation relations through the transformation[52]

2.2.7 Chromium, Molybdenum and Manganese

Chromium and molybdenum are the two most pronounced hardenability alloying elements in steels. Additions of these elements to the steels cause shifts to longer times in the transformation temperatures, which is equivalent to a rightward shift on the CCT diagrams of the steels. This effect can be seen below in Figure 21, which displays the CCT diagrams for the M1 and M2 steels, which differ only in that steel M2 has half the quantity of Cr and Mo that steel M1 has. The rightward shift in the curves on steel M1, which has the higher Cr and Mo compositions, encourage the formation of non-ferritic/pearlitic microstructures, such as bainite at lower cooling rates, and martensite at elevated cooling rates. Additionally, Mo was seen to decrease the transformation start temperature of the steel in several of the works in the literature.[53, 54] Additionally, Radovic et al[55] shows that the addition of Cr and Mo to the V steel used in the experiment promotes the formation of a bainite sheave microstructure, through the suppression of ferritic/pearlitic and acicular ferritic microstructures. Furthermore, the hardenability multiplying factors of Cr and Mo for the calculation of the ideal diameter parameter (The diameter of a bar which can be quenched to produce a 50% martensitic microstructure at the center diameter) can be seen in Figure 22.[56] This figure shows Cr and Mo as the most effective hardenability elements, along with Mn.

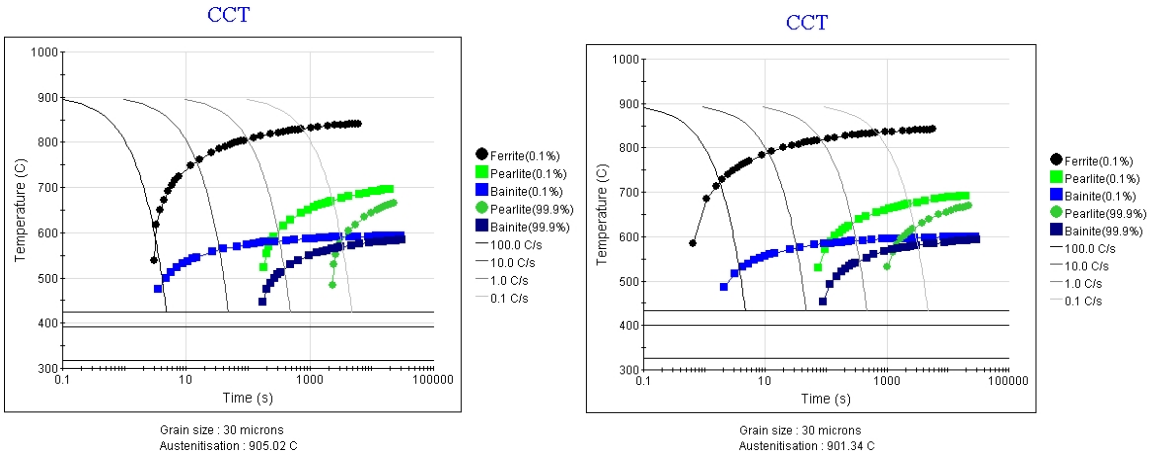

Figure 21: CCT diagrams of steel M1 with high Cr, Mo (pictured left) and steel M2 with low Cr, Mo (picture right) from JMATPro

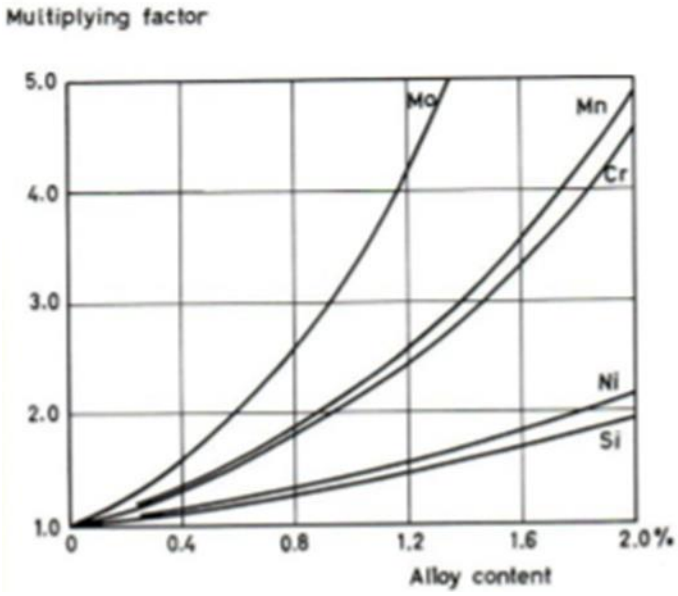

Figure 22: Hardenability multiplying factors of various elements[56]

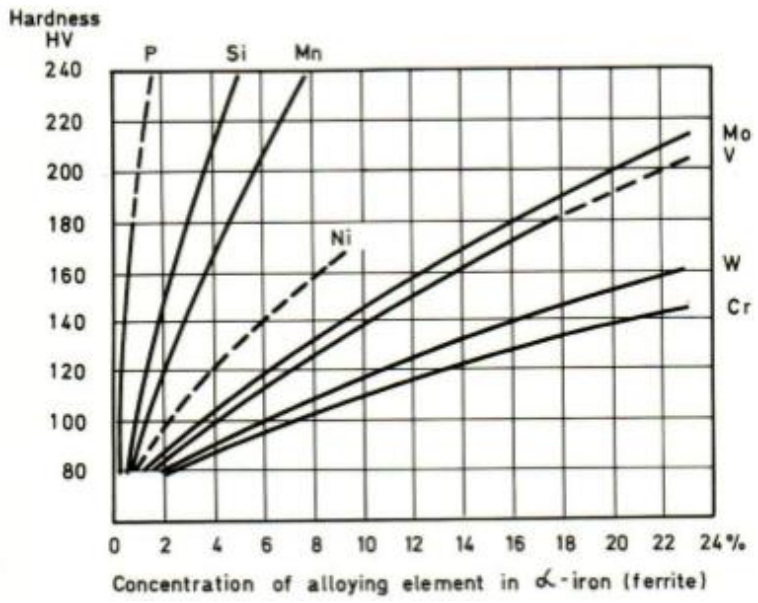

Figure 23: Solute strengthening of various elements in ferrite[56]

Apart from hardenability, these elements, particularly manganese, also show the added benefit of extraordinarily high solute strengthening. These effects can be seen in Figure 23.[56] In this diagram, it is seen that Mn and Mo both display large, positive slopes on the curves relating strength and solute concentration, while Cr shows a moderate, positive slope on its curve. Due to the high solute strengthening potential of Mn, the necessarily low composition of C in the steels designed for this experiment, and the strong hardenability effect of Mn, a large Mn composition has been selected for the BAMPRI steels, such that the high Mn content may substantially increase the hardenability of the steel, and compensate for the low solute strengthening because of the low C content in the steels.

2.2.8 Silicon, Phosphorous and Aluminum

As can be seen from Figure 23, phosphorous and silicon both exhibit superior solute strengthening capabilities, and thus are present for the strengthening capabilities they present. Additionally, P acts as a catalyst for the machining of the wheel hub, concerning which there are multiple segments which require extensive machining after the final forging pass.

Aluminum is perhaps the most complex addition in the design of the steel, as its presence brings about a collection of negative and positive effects. Al has the positive effect of significantly raising the martensitic start temperature (see Figure 24)[56], which can be quite beneficial when the objective is to avoid softer microstructures through quenching. Additionally, as Figure 25 shows, the steel responds very beneficially to the formation of aluminum nitrides for strengthening.[56] However, in the literature it is shown that aluminum nitrides form at quite elevated temperatures, and thus the Al competes with the Ti in the steel for the formation of nitrides.[57] This effect could be quite hampering to the austenitic conditioning of the steel, as TiN is the primary retardant of grain coarsening in the RCR process, while AlN only very slightly affects coarsening.

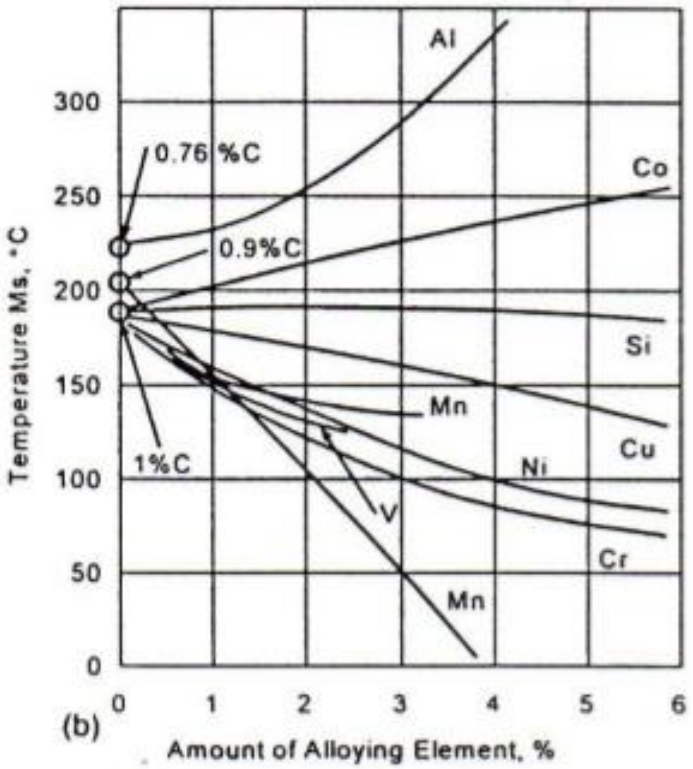

Figure 24: Influence upon M_s transformation temperatures of various elements[56]

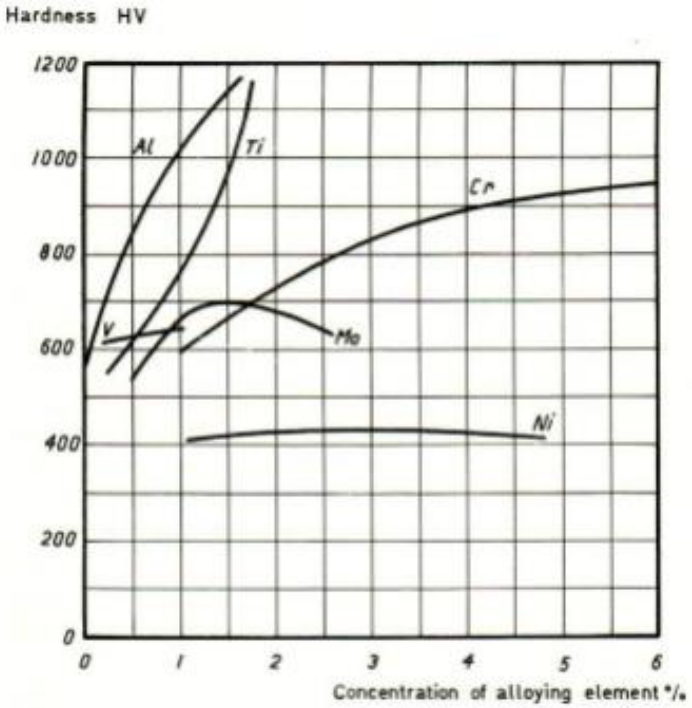

Figure 25: Nitride precipitation strengthening of various elements[56]

2.3 Austenite Conditioning

2.3.1 S_V Parameter

The goal of austenite conditioning is to increase the value of the parameter S_v, which represents the interfacial near-planar surface area per unit volume, since these are both nucleating sites for subsequent transformation and barriers to cleavage crack growth. This parameter is tied to the geometry of the austenite grains comprising the microstructure during high temperature deformation; Specifically, it increases when grains become smaller or when the grains become less spherical in shape, i.e., pancaked. With regard to the increase in S_v for a decrease in austenite grain size, Underwood[58] proposed that for equiaxed austenite grains, the S_v parameter and the grain size are related by the following relation:

$$S_v = \frac{2}{D_\gamma} \tag{2-14}$$

This clearly shows the inverse relationship between the S_v parameter and the austenitic grain size. As the diameter D_γ decreases, the parameter S_v increases. Furthermore, Kozasu et al.[59] elaborate on the contribution of deforming the grains on the S_v parameter. As the grains are deformed, deformation bands are developed in the grains, and these furthermore contribute to the overall S_v value, as can be seen by the following relation:

$$S_v = S_v(GB) + S_v(IPD) \tag{2-15}$$

Where S_v(GB) is the contribution from the austenite grain boundaries, and S_v(IPD) is the contribution from the austenite intragranular planar defects in the austenite.

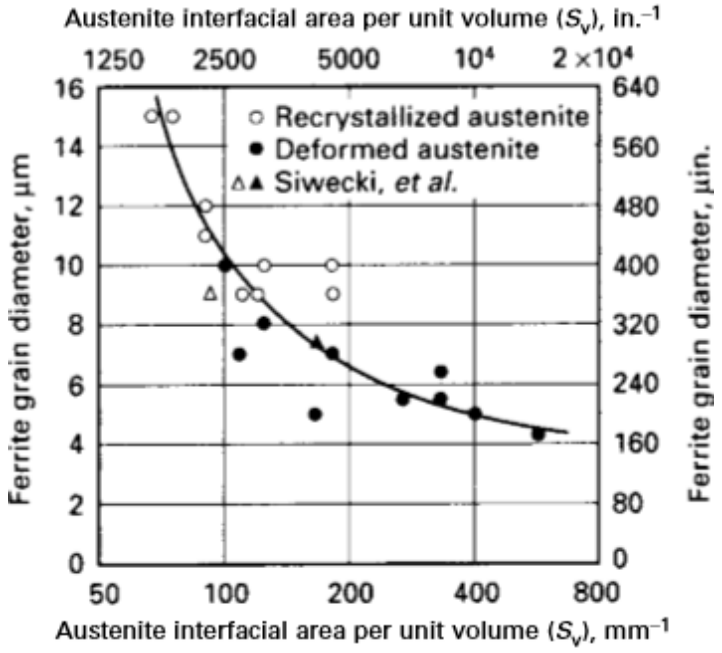

Figure 26: Influence of S_V parameter upon the ferrite grain diameter[60]

The importance of the S_v parameter can be seen in Figure 26, from Speich et al.[60] In this figure, it is seen that as the S_v parameter is increased, the ferrite grain size decreases significantly.

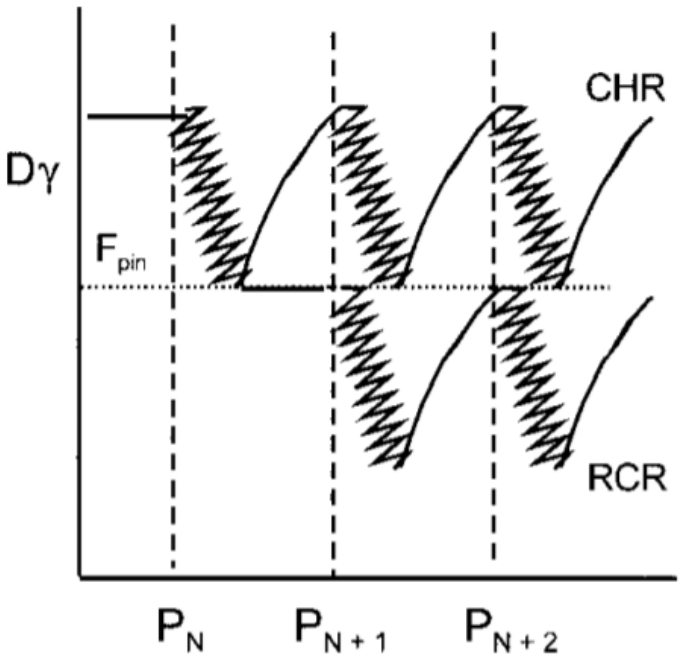

Figure 27: Grain refinement of austenite during deformations in RCR process, compared to the CHR process[61, 62]

The core concept of the RCR schedule can be seen in Figure 27. Here, it is seen that the conventional hot rolling (CHR) does not induce significant grain refinement in the steel. In contrast, the RCR process technology is capable of refining the microstructure more significantly, due to the presence of grain coarsening inhibitors.

2.3.2 Recrystallization and Temperatures T_5 and T_{95}

Recrystallization in metals is a process by which a deformed microstructure is replaced by strain-free grains by a nucleation and growth process.[63] Under conditions of complete recrystallization, the entire microstructure will have been consumed by these deformation-free

grains. Due to the nature of recrystallization being a growth and diffusion-controlled process, it is thus a function of temperature, as can be seen in Figure 28.

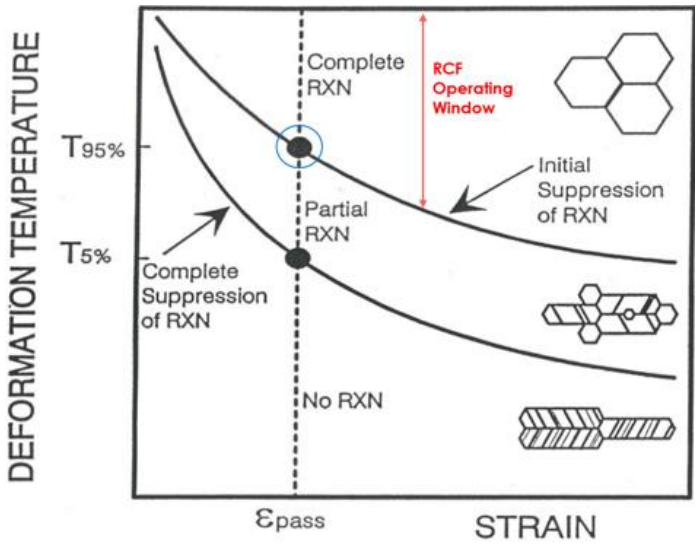

Figure 28: Austenite recrystallization curves as a function of temperature and strain[47]

As can be seen from Figure 28, there are regions of temperatures and strains where recrystallization does not proceed to completion, instead only partially recrystallizing the microstructure. As such, the temperatures T_5 and T_{95} are defined, with temperature T_{95} being of far more importance in this research. T_5 represents the temperature for which the microstructure will contain only 5% recrystallized fraction at a given strain, while the T_{95} for the same strain represents the temperature at which 95% of the microstructure will be recrystallized. For the RCF process, the refinement occurs via the repetitive recrystallization of the microstructure, and as such, all deformations in this process should occur above the T_{95} temperature, where the maximum recrystallization and refinement is possible.

As stated earlier, the primary benefit of the Ti additions to the V steel is depressing of the recrystallization temperatures, as well as the increase in the grain coarsening temperature, which

will be elaborated next. Both effects can be seen in Figure 11 by analysis of the Ti and non-Ti curve locations, while the effect on the recrystallization of the system can be seen in Table 3 below[17], where the T_{95}/T_{RX} temperature is estimated using the sectioning red line.

Table 3: Recrystallization at various temperatures for V-Ti-N steels[17]

Steel	T_{RHT}, °C	D_o, μm	Rolling Temp., °C									
			1080	1030	982	954	927	899	871	850	830	788
V-Ti	1050	19.2		R	R	R	R	R	R	R	P	N
V-Ti-N	1100	17.0	R		R	R	R	R	R	P	P	N
V	1050	107		R		R		R	P	P	N	N
V-N	1100	49 + 171			R	R	P	P	N	N	N	N

R = recrystallized P = partly recrystallized N = non-recrystallized

2.3.3 Grain Coarsening and Temperature T_{GC}

At higher temperatures, microstructures undergo a process known as grain coarsening, where larger grains in the microstructure grow at the expense of smaller grains. This process is driven by the will of the system to minimize the grain boundary energy per unit volume, i.e. the grain boundary area per unit volume.[63] Grain boundaries thus move towards their center of curvature, and sharp, or highly curved boundaries tend to straighten. Thus, the process is controlled by the motion of grain boundaries, a diffusional process. As a diffusional process, the motion of the grain boundaries is thermally activated, and depends upon the temperature. Included below in Figure 29 is a diagram from Siwecki et al.[14] which separates regions of fine and coarse

microstructures in the 3-dimensional space displaying temperature, holding time, and strain level effects. Herein only the temperature effects are considered, as the time and deformation parameters are strictly defined by the production requirements of the industry partners. It should be noted that the author explains that the surface opens around the deformation axis at more severe values, allowing for more forgivable conditions (higher temperatures and holding times).

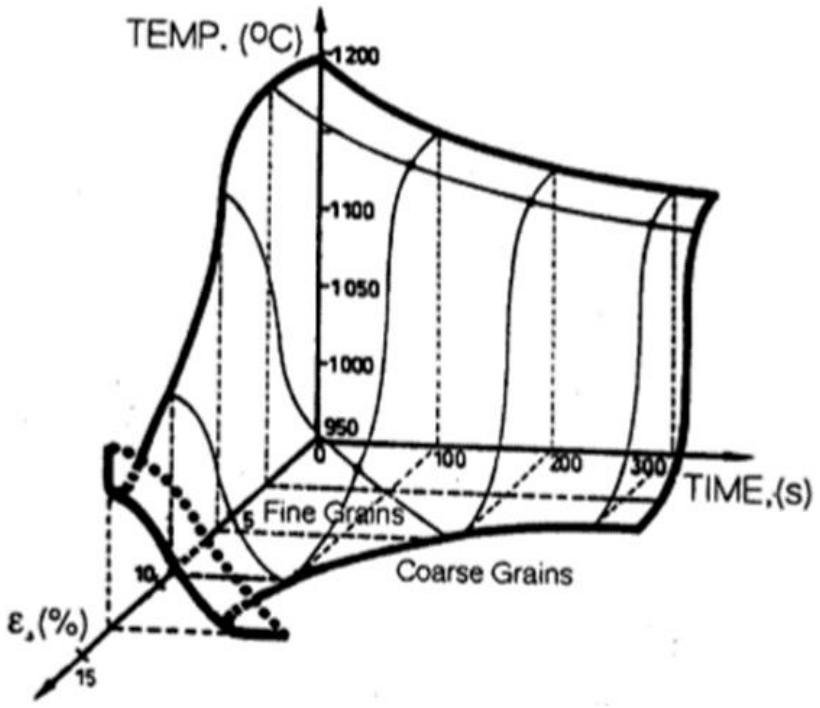

Figure 29: Grain coarsening in T-t-ε space[14]

In the presence of high stability, fine precipitates, which are insoluble up to very high temperatures, the temperature requirements for grain coarsening are increased, and coarsening occurs via abnormal grain coarsening. In this process, the microstructure remains relatively unchanged, save for a small number of grains which grow at excessively high rates.[33] This form of abnormal grain coarsening results in a bimodal distribution of grain sizes, and significantly raises the standard deviation of the grain size distribution function. Curves such as those pictured

in Figure 30 from Zheng et al.[17] can be used to display the grain coarsening temperature T_{GC}, which occurs at the beginning of the upper curve, which represents the average size of the secondary coarsening grains. A vertical red line has been introduced into this figure, such as to aid in the estimation of the grain coarsening temperature for the V-Ti-N system.

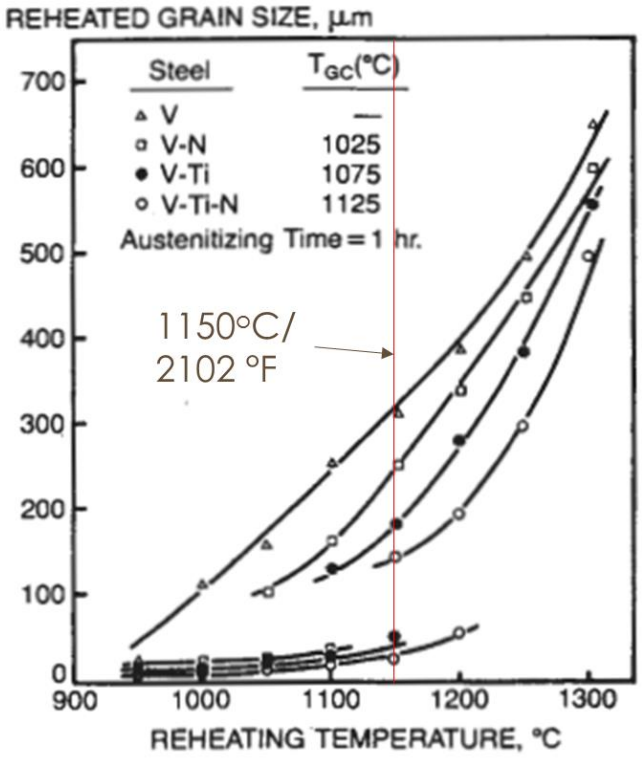

Figure 30: Grain coarsening curves for the V-Ti-N steel systems[17]

As can be seen in Figure 30, the additions of Ti and N to the V steel result in a remarkable increase in the grain coarsening temperature of the steel. This result is also shown elsewhere in the literature.[1, 3, 14, 24, 64] However, the influence of the Ti and N composition decreases significantly without the proper processing. In the literature, it is consistently stated that fine precipitates retard grain boundary motion to a higher degree, and thus further retard the coarsening of the microstructure. This can be seen in Figure 31,[64] which displays models developed by Zener[65],

Gladman[33], and Hellman-Hillert[66]. Each of these models shows increased grain refinement for precipitates of smaller sizes and/or larger volume fractions, both resulting in a higher density particle distribution.

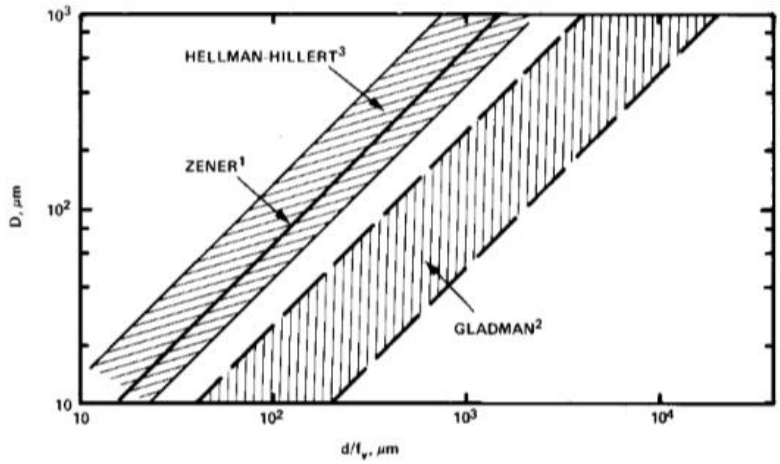

Figure 31: Three models relating grain size to precipitate particle distributions[64]

2.3.4 Deformation and Forging Passes

In the recrystallization controlled forging process, the forging passes are implemented not just to shape the piece, but also to refine the austenitic microstructure, in preparation for the cooling and transformation. The forging passes implemented are conducted at large deformations, to maximize the contribution from the grain refinement, through higher recrystallization nucleation rates. These deformations thus increase the total S_V of the microstructure through increasing the S_V^{GB} values, as can be seen in Figure 32.[60] Figure 33 also helps to illustrate the influence of the austenitic grain size upon the total S_V value for the steel.[59] As can be seen from this figure, an increase in the ASTM grain size number (i.e. a decrease in the grain size) corresponds to an

increase in the S_V for the steel. It is important to note that the deformation temperature range for the RCF process occurs entirely between T_{RX} (the temperature for 95% recrystallization) and T_{GC} (the grain coarsening temperature). This temperature range is overlayed upon Figure 11 from Zheng et al.[17] in Figure 34 pictured below. Zheng et al.[17] also showed that this temperature range is 175°C larger for the V-Ti steels than for the V steels, allowing for higher temperature deformations and longer holding times, ultimately permitting lower forging loads and high flexibility in the manufacturing process.

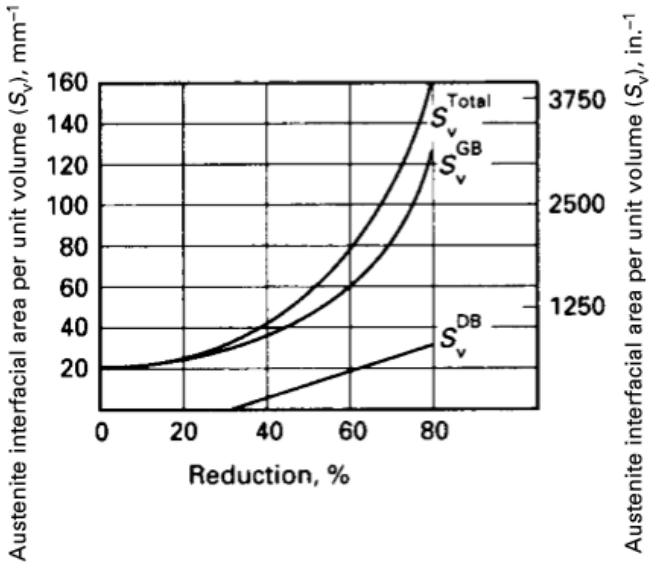

Figure 32: Deformation influence upon S_V parameter contributors[60]

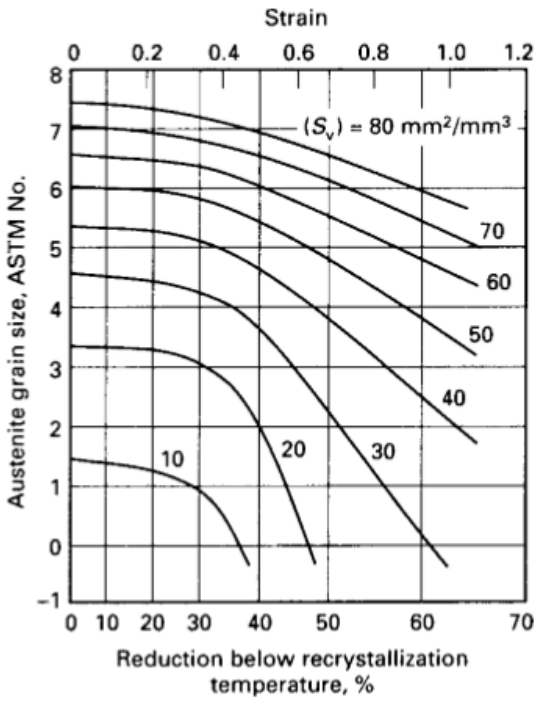

Figure 33: Constant S_V curves plotted on a grain size vs reduction axis system[59]

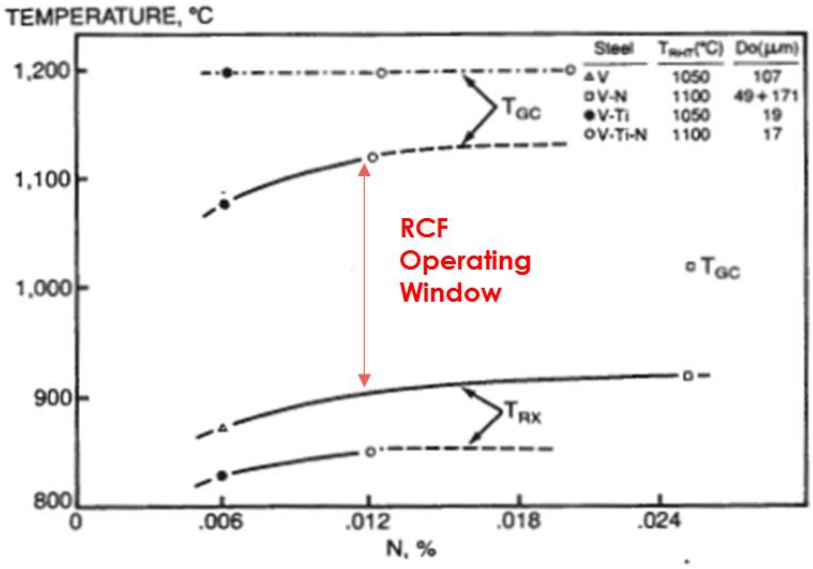

Figure 34: RCF operating window in V-Ti-N systems[17]

2.4 Cooling and Transformation

2.4.1 Cooling Rates

Following high temperature conditioning of the austenite in the steel, proper cooling schedules are necessary to capitalize on the former processing. JMATPro simulation software is an excellent resource in this regard, as it allows for one to specify an initial austenite grain size and a cooling rate, and then produce diagrams to analyze the expected microstructure phase constitution. Some diagrams which can be derived from the software include CCT diagrams (shown in Figure 21), TTT diagrams (shown in Figure 35), and phase-temperature diagrams (shown in Figure 36).

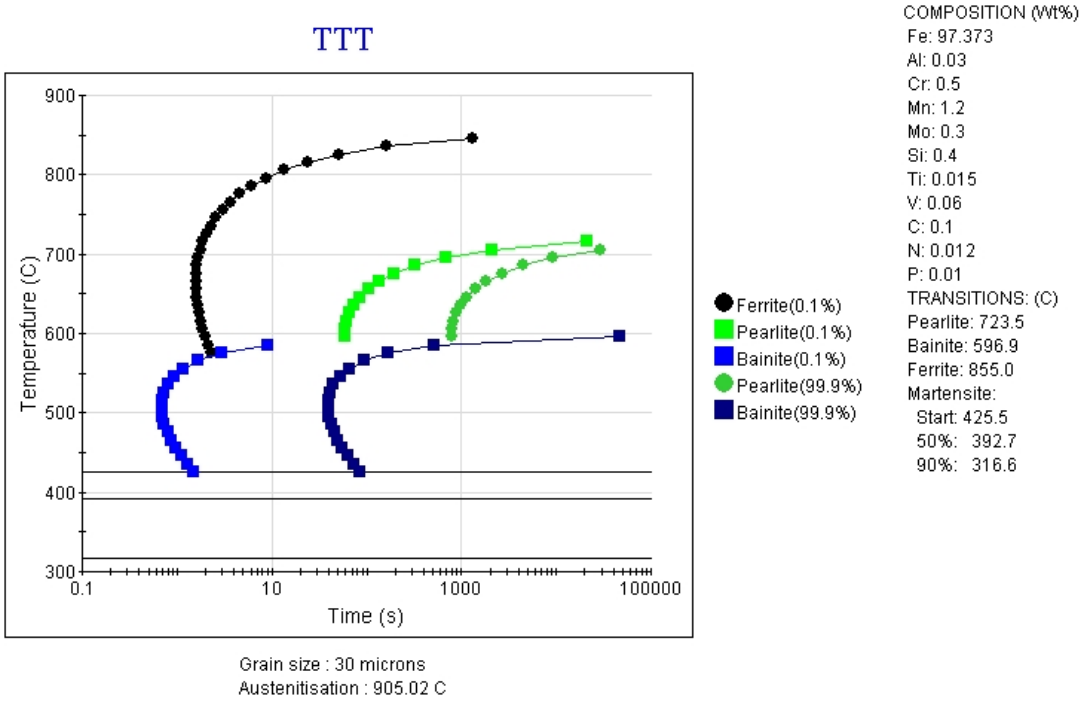

Figure 35: TTT diagram for M1 steel drom JMATPro

These diagrams are extremely useful in the design of the cooling schedule, as they allow for the selection of cooling rates and holding times for optimization of the microstructure for a set of desired properties. It is well known the general property differences and disadvantages between the various phases in steel and modifying the microstructure to utilize these phases when needed is a core focus of the experiments discussed herein.

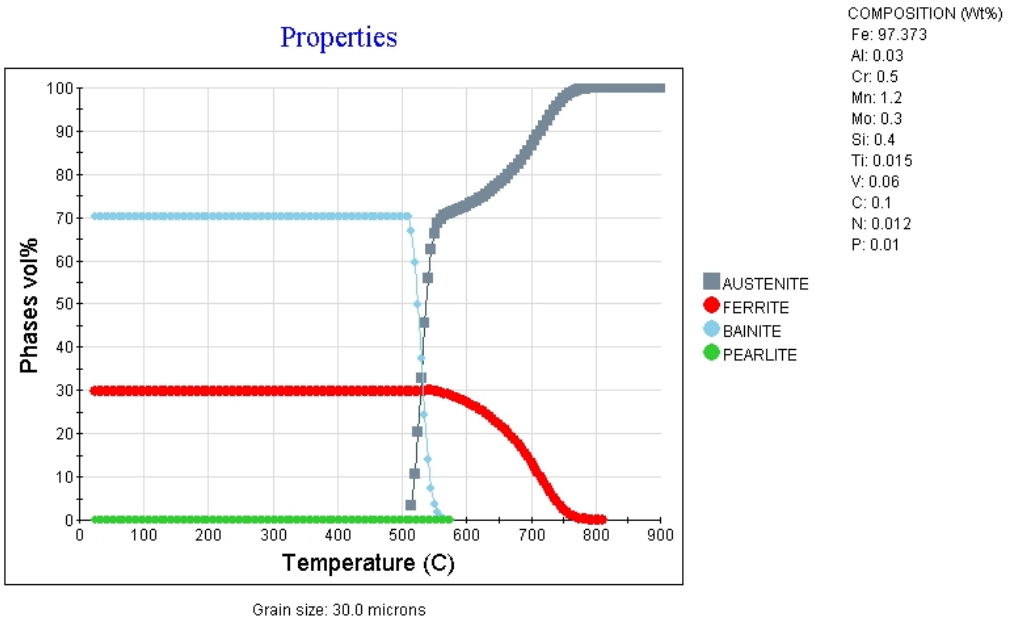

Figure 36: M1 phase-temperature diagram at 5°C/s from JMATPro

An example of phase changes with cooling modifications provided in the literature is presented in Table 4 below, where the author changed the cooling rate of the steel and produces microstructures varying in phase compositions and strength.[67] In this table, an introduction of granular bainite into the polygonal ferrite and pearlite microstructure, due to an increase in the cooling rate, causes a significant rise in the hardness of the steel. Note that further increases in the cooling rate resulted in a martensitic microstructure with a significantly higher hardness level.

Table 4: Microstructure and hardness changes due to cooling rate[67]

Heat Treatment	Cooling rate (K s^{-1})	VHN	Microstructure
Annealing	0.03	167	PF + P
Normalising	1.4	224	PF + P + GB
Quenching	300	436	M

[a] PF, polygonal ferrite; P, pearlite; GB, granular bainite; M, martensite.

In the literature, several authors have noted increases in strength when the cooling rate of the steel is increased. Apart from the differences in phases in the microstructure, this change can be attributed to either refinements in the microstructure due to domination of nucleation events over growth events during transformations or through limiting growth of the austenitic microstructure during high temperature processing. Figure 37[18] shows an example from the literature of the limitation of austenitic microstructure or grain size due to an increase in the high temperature cooling rate.

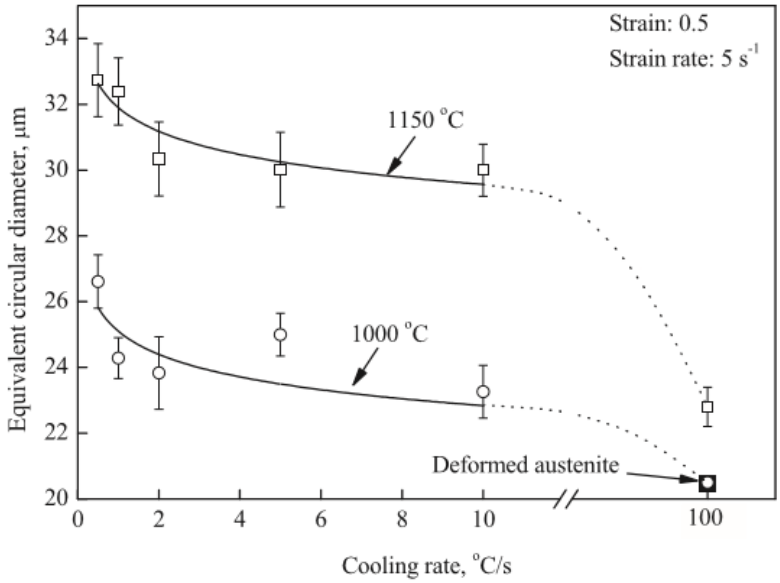

Figure 37: Effect of high temperature cooling rate onaustenitic grain size[18]

In this diagram, the temperature upon the curve represents the deformation temperature, and the microstructure is seen to be refined through increasing the cooling rate, although this effect is seen to diminish at higher cooling rates. In reality, Figure 37 shows how the diffusive growth of freshly recrystallized austenite grains can be reduced through increased cooling rates.

The cooling rate during the transformation temperature regime also has a large influence on the final grain size and properties. Figure 38[14] below shows the influence of increasing the cooling rate on several steels. As can be seen, an increase in the cooling rate brings about a significant reduction in the final ferrite grain size, as well as an increase in the strength of the steel.

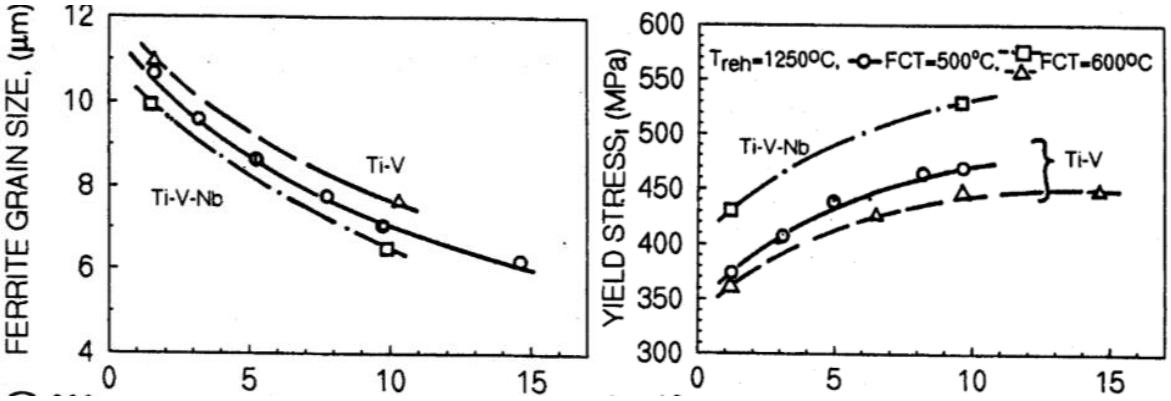

Figure 38: Effect of low-temperature cooling rate on final properties[14]

2.4.2 RCF Cooling Schedules

In the recrystallization controlled forging process, the cooling schedule is comprised of some form of controlled cooling from the final forging pass to a predetermined water end temperature (WET), followed by a hold of variable time at this WET, and concluding with an air cool to room temperature (ACRT). Figure 39 contains several temperature paths, which show the

various possible cooling schedules which the steel might assume upon completion of the second forging pass. At several places in the literature a schedule such as this is present in the RCR process. In the defining article concerning the RCR process, the authors state that a core basis of the RCR process is the utilization of accelerated cooling to an intermediate temperature, followed by ACRT.[17] In another article, Chen et al.[18] subjected the steels of the experiment to the cooling schedule shown in Figure 40. As can be seen, the steels underwent accelerated cooling to the intermediate temperature of 400°C and were then allowed to ACRT. In a collaborative article from DeArdo and Zheng,[23] multiple RCR cooling schedules were investigated, including ACRT, cooling at 6.7°C/s to 550°C followed by ACRT, and finally cooling at 8.7°C/s to 594°C followed by ACRT. Within this work, it was found that good combinations of strength and toughness were attainable using the proposed RCR processing and cooling schedules.

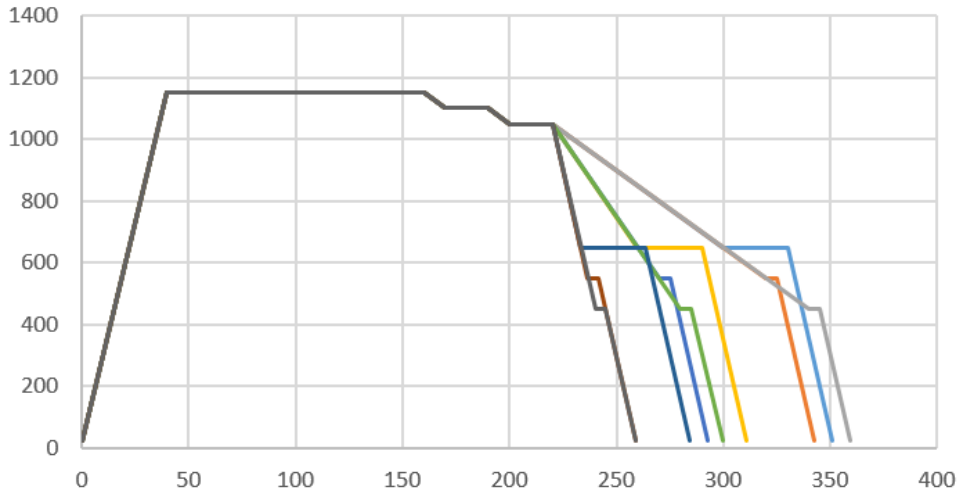

Figure 39: Possible temperature paths during cooling to achieve different strength levels. For example, the lengthy hold at 620°C is expected to result in F-P microstructures, the shorter hold at 550°C in F-B microstructures and the very short hold at 450°C in F-M microstructures.

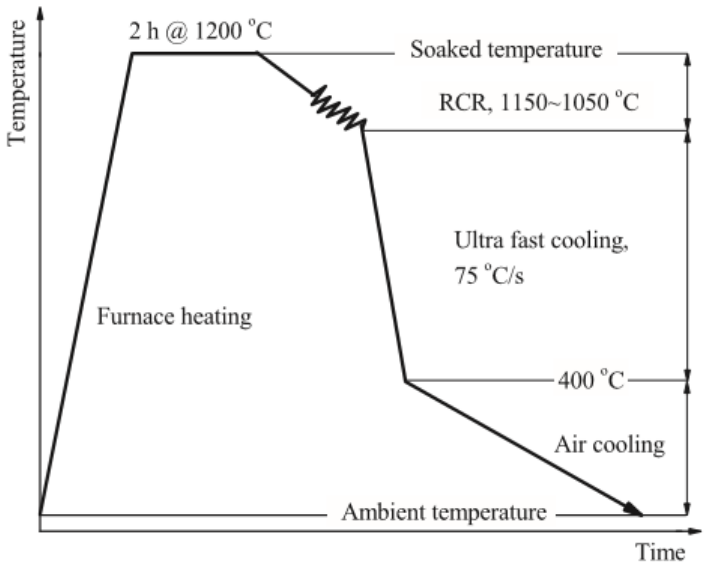

Figure 40: Temperature path utilized in the RCR process[18]

Of additional importance to the processing of the pieces forged using the RCF process is the variation of cooling throughout the portions of the part, as variations in the microstructure may arise because of these cooling discrepancies. One such example of these differences is provided below in Figures 41 and 42. In Figure 41, a sample sectioning of the final piece which will be produced in this study is presented, and regions of the piece are labeled surface (where the highest cooling rates are expected), and center (where the lowest cooling rates are expected). In Figure 42, the CCT of the M1 steel is presented, and the cooling curves of the edge and center regions are overlaid on the diagram, having been generated using ANSYS thermal simulation software.

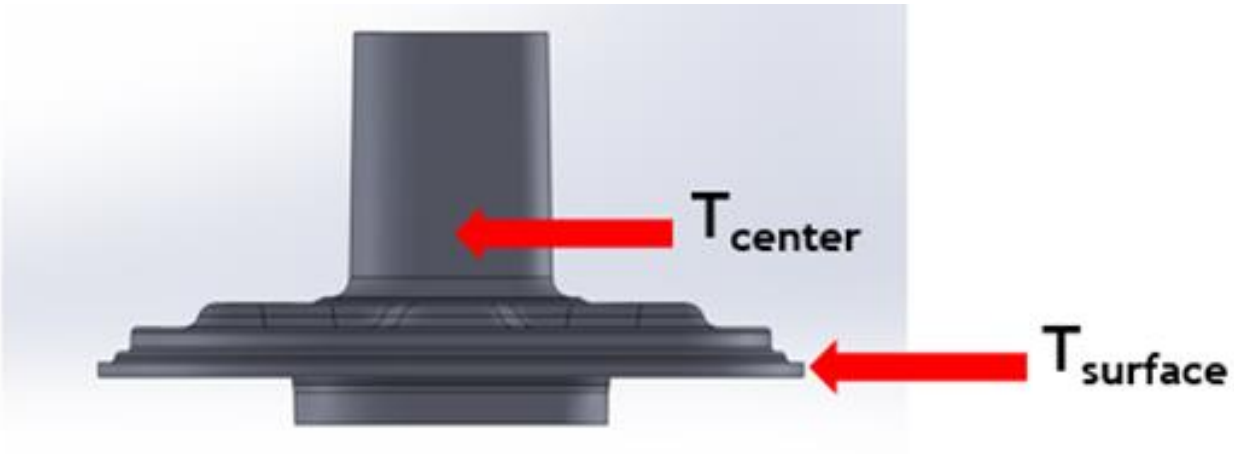

Figure 41: Wheel hub with labeled cooling regions

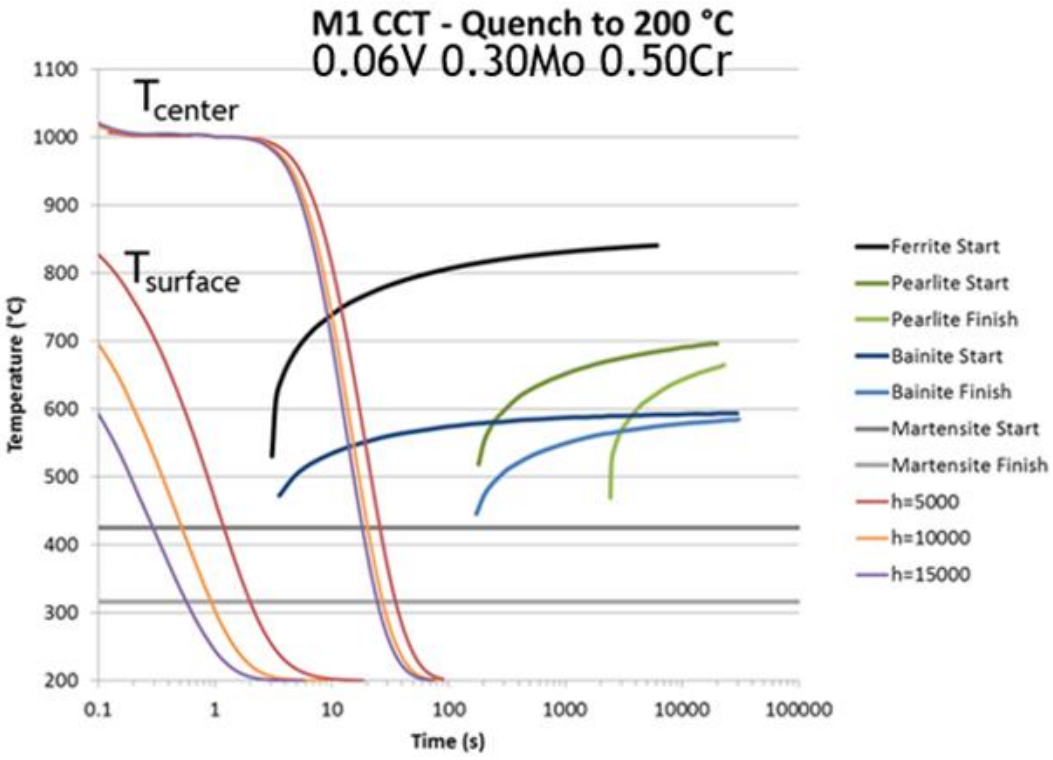

Figure 42: M1 CCT diagram with overlaid cooling profiles

From these overlays, while the edge is predicted to comprise only of martensite, the center of the specimen additionally crosses both the ferrite and bainite start curves, and thus may have a composition comprising of martensite, ferrite and bainite.

2.5 Relation to FIERF RCF Project

2.5.1 Austenite Conditioning

The underlying principal of the RCF experiments proposed in this project is the increasing of the toughness and strength of the steels through an increasing of the S_V parameter by refining the austenitic microstructure. It was shown in Figure 26 that the ferrite grain size is seen to decrease as the S_V parameter is increased.[60] As the well-known Hall-Petch equation shows, this refinement of the ferrite microstructure causes an increase in both the strength and toughness of the F-P microstructure in the steel.[12, 13] To refine the microstructure in this experiment, a series of 2 hot forging steps will be employed. Upon completion of the deformation steps, the deformed microstructure will undergo recrystallization, where new strain-free grains are nucleated. This process decreases the austenitic grain size. Since this process must occur at high-enough temperatures for recrystallization to occur, a grain coarsening inhibitor must be added to the steel to increase the grain coarsening temperature, T_{GC}. It is to this end that Ti and N are added to the steel. TiN particles have a significant effect on the steel, raising the T_{GC} markedly.[17] It is important in this experiment that the Ti content be sub-stoichiometric with regards to the Ti:N stoichiometry of 3.42. This is necessary as large quantities of Ti in the steel would lead to coarsening of the TiN particles, and would reduce the effectiveness of the grain coarsening inhibition.[14, 27]

Having designed the steels for high T_{GC} values, experiments were conducted to determine the proper reheating temperature for each steel. These experiments comprise of heating specimens of each steel to various reheating temperatures between 950°C and 1250°C for 5 minutes, to simulate the induction heating in the forging plant, and then quenching to room temperature to form a martensitic microstructure. A picric acid etchant is utilized to determine the prior austenitic grain size, and the grain coarsening temperature is determined through analysis of the data. A reheating temperature is then selected below this determined temperature.

Once the reheat temperature is selected, a series of deformation trials was completed to determine the optimal temperatures at which the two 50% forging blows are to be conducted at. For these experiments, the steels are heated to the reheat temperature determined in the previous trials, and then cooled to various forging temperatures and hot compressed 50%. The specimens are then quenched, and the austenite grain size and shape again determined. These trials determine the forging temperatures at which the most grain refinement is seen in the steel, and the T_{95} temperature for each steel.

2.5.2 Cooling and Transformation

Upon completion of the austenite conditioning, the analysis of the cooling rates and holding temperature during the steel's cooling to room temperature was conducted. As was shown in the literature by Rodrigues et al.,[67] changes in the cooling schedule of the steel can result in various microstructures with differing mechanical properties. It is for this reason that cooling schedules as shown in Figure 39 and Figure 40[18] were employed, to produce multiple strength levels with a single steel composition. Analysis of diagrams and simulations such as those displayed in Figure

42 were conducted, and the information gleaned from these studies helped to design experiments which pinpoint the temperatures at which the various phase transformations of each steel occur.

The cooling and transformation studies proposed herein comprise initially of the austenite conditioning processes determined in the previous experiments. Upon completion of these previous steps, the steel was cooled to a WET, where it was held for a time which varied upon the anticipated phase transformation. Upon further cooling of these steels to room temperature, the phase volume fractions of the steels were analyzed. The data found herein served to design the cooling paths for the final trials which will occur on MFC production lines. Figure 43 below shows an example of the use of CCT diagrams provided by JMATPro in order to determine the approximate WET values for the cooling experiments.

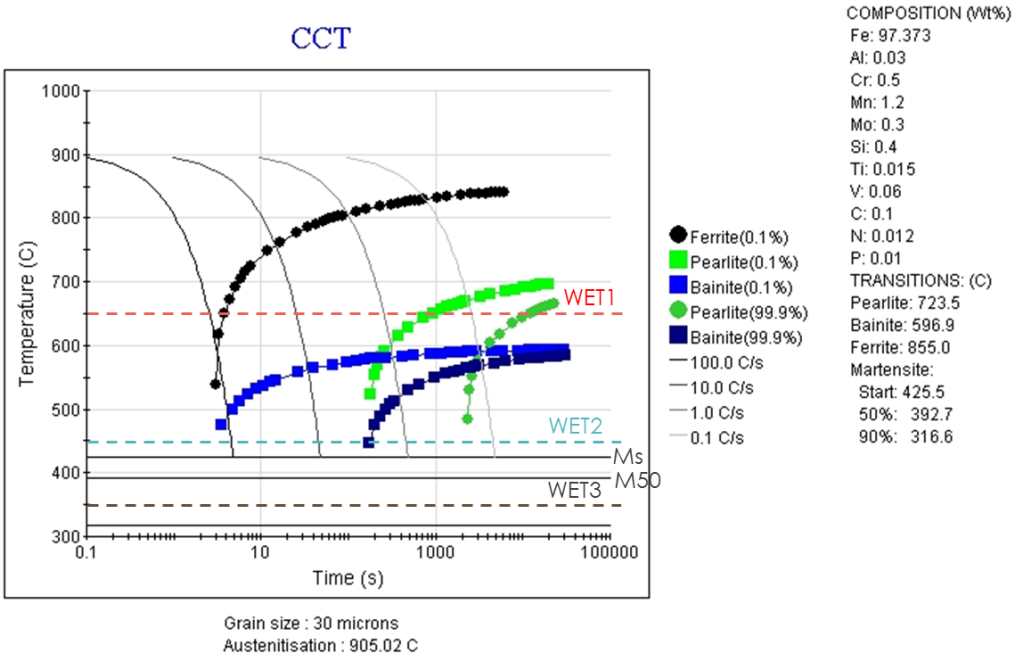

Figure 43: Steel M1 CCT diagram with approximate WET selections

2.5.3 Strengthening Employed

Multiple strengthening mechanisms were employed within the steels in the current experiment. Grain boundary strengthening is by far the most prevalent strengthening mechanism, as the foremost purpose of the project is the refinement of the microstructure of the steel, to amplify mechanical properties via the Hall-Petch equation. In addition, the benefit to toughness of fine austenite grains is also recognized. However, several other strengthening mechanisms are present in the steels.

The V presence in the steel primarily serves to provide a source of precipitation strengthening in the steel. Because the steel is sub-stoichiometric in the Ti:N ratio, complete precipitation of TiN particles leaves excess N for the precipitation of VN or VCN, which precipitates at a lower temperature than TiN, and has significant precipitation hardening effects.[1] Additionally, upon the depletion of N in the steel, the V further precipitates as VC, increasing the precipitation hardening increment furthermore. Precipitation hardening, however, also serves to decrease the toughness of the steel,[38, 39] and thus the current experiments primarily utilize toughness favoring grain boundary strengthening over, or at least in conjunction with, the detrimental precipitation hardening effects.

A third strengthening mechanism is present in the steels' designs in the form of solute strengthening. While C is the most prevalent of solute strengthening additions, many other elements are added for this purpose as well. Figure 23[56] displays quite well the strengthening effect of additions of many of the elements in the current steels' designs.

Apart from the strengthening mechanisms previously mentioned, the most prevalent remaining mechanism is dislocation strengthening. This strengthening mechanism is generally accrued through the deformation passes of the steel. However, this mechanism is not present in

notable quantities in the steels present herein, because the high temperatures at which the deformations occur. The recrystallization of the microstructure following the deformation nucleates strain-free austenite grains,[61] and thus eliminates the dislocations from which the dislocation strengthening would derive. However, the formation of bainite and/or martensite, being displacive transformations involving shearing, will result in high dislocation densities leading to the possibility of very high strength being attained in the final forging.

3.0 Statement of Objectives

The operating hypotheses for the project were as follows: First, the Titanium Nitride project steels were expected to form a fine dispersion of Titanium Nitride precipitation, preventing grain coarsening to high temperatures, exceeding 1150°C, as similar grain coarsening prevention was seen in the study by Zheng et al.[17], where grain coarsening was impeded until 1150°C. Second, prior austenite grain refinement to approximately 20μm average equivalent austenite grain diameter was predicted, as the same study by Zheng et al.[17] also noted post deformation prior austenite grain diameters between 15-25°C, as can be observed in Figure 12. Third, through controlled cooling, microstructures predominantly consisting of ferrite/pearlite, bainite and martensite were expected to provide low, medium and high strengths. These phases were anticipated in the final microstructure from analysis of CCT curves similar to Figure 21, which were generated with JMATPro simulation software. These microstructures were anticipated to provide multiple strength and toughness combinations, with the strength of the bainitic forgings exceeding that of the standard, 10V40 steel forging. The strengths of the non-martensitic forgings were expected to range from 550MPa to 830MPa (80 KSI to 120 KSI). Chen et al.[18] observed tensile strengths in an ultrafast cooled bainite RCR steel approaching 980MPa, demonstrating the strength capacity of the RCR cooling technology.

The objectives of this project were to optimize the performance of steel forgings in automotive applications by providing a good combination of strength and toughness, while limiting the cost of production of the steel. Additionally, a further objective of the project was to investigate cooling schedules which could be applied to the steels, providing flexibility in the final product.

To accomplish these objectives, an additional objective was set forth, to characterize the steels. This characterization included determination of the T_{GC}, the T_{RH} and the metallography of the final microstructure after several cooling schedules. After the steel characterization, the objectives shifted to application of the steels in the full-scale forging trials, in order to fulfill the goal of creating automotive forgings with concurrent high strengths and toughness values.

The final objective of the project was to provide an analytical description of the precipitation and phases present in the final forging samples. To this extent, the phases in the steel were intended to be identified and the phase percentage determined, as well as hardness measurements of the phases observed. A core goal of this objective was the formation of a predominantly bainitic constituent microstructure forging, in order to achieve the intermediate strength and toughness condition. The precipitates in the steel were also intended to be identified, and the average size of the different precipitates present in the steel. Finally, the identified precipitate nature was to be analyzed with models put forth in the literature, in order to determine the effectiveness of the pinning of the precipitates.

4.0 Experimental Procedures

The steels tested in this experiment were melted at TIMKENSTEEL Steel Company and were produced in laboratory size heats. Here, vacuum induction melting (VIM) was used, and the steels were hot forged into bars of the following diameters: Steels 10V40, M1, M2 and M3 were forged to a 2.75 inch diameter (2.985 mm), steel T1 was forged to a 3.392 inch diameter (8.616 mm), and steel T2 was forged to a 4 inch (10.16 mm) diameter. All steels were air cooled to room temperature following forging. Steels T1 and T2 were then machined to 2.75 inches (2.985 mm) to match the other steels. These bars were then machined into 6-inch (15.24 mm) mults. These mults were the starting condition for all steels used in experiments.

The as received condition for steel M3 is shown in Figure 44. Here, the steel is etched according to the procedure listed in section 4.1.1, revealing a ferrite and bainite constituent microstructure.

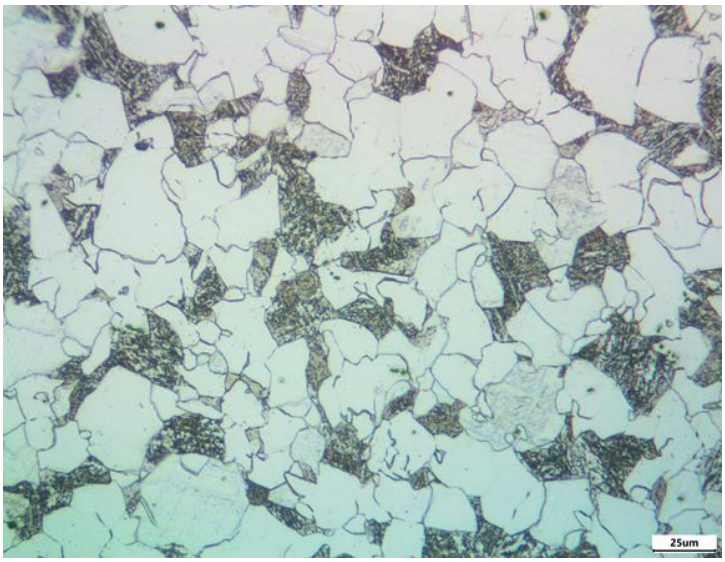

Figure 44: Steel M3 as received condition, showing ferrite and bainite microstructure

4.1 Microstructural Analysis

4.1.1 Optical Microscopy

Optical Metallography was used to investigate the microstructure of the steels throughout the project. Magnifications between 100X to 1000X were typically used. Steel samples were machined using an ALLIED TechCut diamond saw cutter and were subsequently mounted in a bakelite mount. The mounts were then surface ground using 240, 400, 600, 800 and 1200 grit grinding paper. Following grinding with the 1200 grinding paper, the samples were polished in a Buehler Vibromet 2 vibrational polisher with .05 μm Alumina powder for 45 minutes at 60% instrument intensity.

In order to reveal microstructural constituents, several etches were used previous to microscopy. For ferrite/pearlite, bainite and martensitic phase revelation, a 2% Nital Etch was used to etch the grain boundaries of the ferrite phase and the morphology of the structure. This etch was created using 1mL of HCl acid and 49 mL of 190 proof Ethanol alcohol. For etching, the sample surface was submerged in the etchant until the grain boundaries and morphology traits were revealed under optical microscopy (OM), typically between 2 to 5 seconds total.

To reveal the prior austenitic grain boundaries (PAGB) from the quenched martensitic microstructure, a Picric etchant was used. Here, 100 mL of saturated Picric acid was combined with 10g of Sodium DodecylBenzene Sulfonate and 1 mL of HCl acid. Using a hot plate, the solution was heated, and held between 85°C and 90°C. The samples were submerged in this solution until the PAGB structure was revealed, typically between 30 to 90 seconds total. Here, it was important to frequently clean the surface of the sample, to prevent etching of the inner portions

of the austenite grains. The samples were typically rinsed every 10 seconds of etching, allowing for clearer PAGB images for measurement.

To reveal bainite microstructures, a Lepera etchant was used. Here, a solution of 50 ml of 1% $Na_2S_2O_5$ in distilled water and a second solution of 50 ml of 4% Picric acid in Ethanol were used. Samples were first submerged in the Picric acid solution for etching, and subsequently submerged in the $Na_2S_2O_5$ solution to color the phases, allowing for accurate phase identification and calculations.

The locations for optical microscopy are shown in location 1-5 in figure 45, shown in section 4.2.1. Here, location 1 is at the center of the flange with a fast cooling rate, location 2 is near the surface of the flange/column fillet with a fast cooling rate, location 3 is at the center of the column with a very slow cooling rate, location 4 is at the deepest location in the column which is not machined out, and location 5 is at the center of the stamp lip with a moderate cooling rate.

4.1.2 Scanning Electron Microscopy (SEM)

Scanning Electron Microscopy (SEM) was used in the experiment to identify phases present apart from ferrite and martensite. For this purpose, a SEM_FEI Apreo was used. Samples for SEM uses were produced according to the mount preparation procedure explained in section 4.1.1. For observation, 10kV-20kV voltage was used for magnifications up to 50,000X. Secondary electron imaging was used to reveal the surface details. External EDS software was used for the identification and qualitative analysis of composition in imaging.

4.1.3 Transmission Electron Microscopy (TEM)

Transmission Electron Microscopy was used to investigate the precipitates in the steel. For preparation, approximately 1mm thick foils were machined from the bulk material using an ALLIED TechCut diamond saw, following which the foils were ground to approximately 100μm to 150μm thickness, using 400 grit grinding paper. 3 mm diameter discs were punched from the resulting foil, and the resulting discs were then further ground to 25μm to 35μm using 600 grit grinding paper and a disc grinder. Jet Polishing in a Model 120 Fischione Jet Polisher was performed until sample penetration in a solution of 25mL Perchloric Acid and 475mL Acetic Acid (5% Perchloric, 95% Acetic Acid). The precipitates were first observed in bright field, but were identified using Selected Area Diffraction and Center Dark Field Imaging.

4.1.4 Grain Size Measurements

ImageJ image analysis software was used to analyze optical images of etched samples. For ferrite/pearlite microstructures, ferrite grains were outlined, and ImageJ calculated the equivalent circular grain diameter for each grain. A minimum of 100 grains were measured, with 200 grains serving as the target quantity to increase accuracy of results. Microsoft Excel software was used to calculate statistical quantities for each measured condition. For the Picric etched samples, ImageJ was used to outline the austenite grains, allowing for similar calculations. Additionally, for the recrystallization experiments, spreadsheets were generated using ImageJ and Excel for both the recrystallized and non-recrystallized austenite grains, allowing for calculation of recrystallization fractions.

4.2 Mechanical Properties

4.2.1 Tensile Testing

Tensile tests were conducted using an MTS Landmark Testing Frame. For this, sub-size tensile samples with a 25.4mm gage length were machined, according to ASTM standard E 8M-04. The samples were machined from the full forging trials according to the vertical red rectangle in Figure 45 below. Here, the width of the sample is perpendicular to the radial direction of the forging column, while the length of the sample is parallel to the length of the column. Microscopy performed at location 4 was used to characterize the microstructure at the gauge length of the tensile tests.

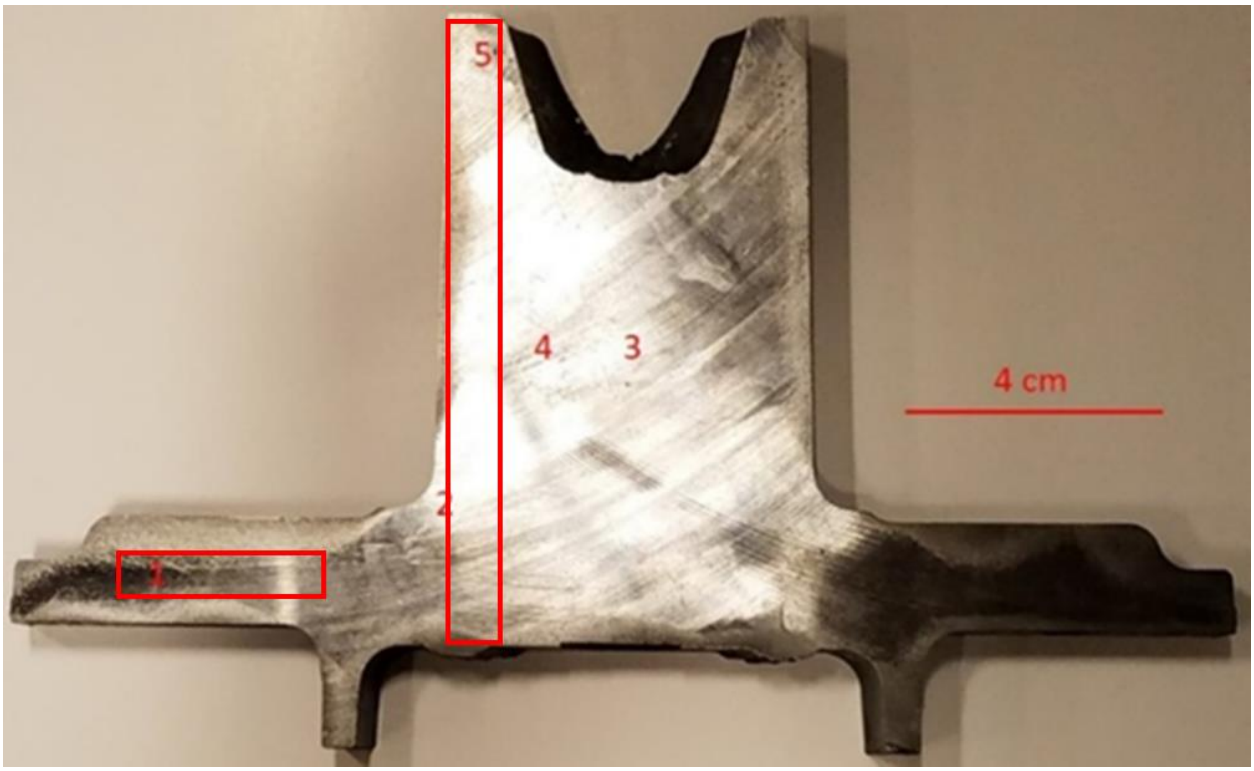

Figure 45: Full forging section with tensile, charpy and hardness locations

4.2.2 Micro Hardness and Nano Hardness

Macro hardness testing for the samples was performed using a 300g force diamond tip hardness tester. Macro hardness testing is more readily performed than tensile testing and can be performed at any location throughout the steel, whereas tensile testing can only be performed in geometrically viable locations. Due to this accessibility of macro hardness testing, macro hardness values were used to characterize the uniformity of the forgings.

Micro hardness testing was used to investigate the hardness of the various phases in the samples. Here, A light Nital etch was performed until the phase morphologies was lightly revealed. Following this, the indentations were categorized according to phase, being labeled as a single phase or a multi-phase indentation. This allowed for generation of average hardness values for the present phases.

4.3 Austenitic Phase Processing

4.3.1 Initial Convection Furnace Heating Trial

Before the experiments to characterize the steels could begin, the initial furnace heating trials needed to be designed to determine the impact of using convection furnaces for the trials. As MFC uses an induction furnace for reheating, which heats to temperature almost instantaneously, the heating time for the BAMPRI laboratory convection needed to be determined. Once determined, all following experiments could be adjusted to compensate for this heat up time.

For these experiments, low carbon steel samples with the geometry detailed in section 4.3.3 were used. Securing the thermocouple in the sample, the sample was inserted into the furnace, preheated to 1150°C. The temperature of the sample was plotted, and the time for the sample to come within 20°C of the target 1150°C was determined. For further experiments, this time was added to the MFC reheating time to determine the proper convection reheating time.

4.3.2 Grain Coarsening Trials

The grain coarsening trials were designed to determine the grain coarsening temperature for each steel. As discussed in section 2.3.3, the grain coarsening temperature, T_{GC}, is the temperature above which abnormal grain growth occurs. For production, this temperature represents the maximum temperature for effective austenitic processing, as coarse austenite microstructures are achieved above this temperature.

Preceding the experiment design, the initial convection furnace heating experiments described in section 4.3.1 were conducted to determine the time for a convection furnace to heat a steel sample to the desired temperature, in comparison with the near instantaneous heating time in the induction furnaces used at MFC. These experiments determined that approximately 3 minutes convection heating time was required to bring the sample to within 25°C of the target temperature. When combined with the 2-minute standard reheating time at MFC, a 5-minute reheating time was selected for the processing experiments.

To determine the grain coarsening temperature, 12mm cubic samples were machined from the hot rolled steels. These samples were encapsulated in quartz tubes under a backfilled Argon atmosphere to prevent oxidation at high temperatures. These tubes were then cold charge inserted into a furnace at temperatures ranging from 1250°C to 950°C, with 50°C intervals. After the

determined 5 minutes holding, the tubes were removed from the furnace and broken in a room temperature water bath within 3 seconds. The resultant martensitic microstructures were etched to reveal the PAGB according to the picric acid technique detailed in section 4.1.1. Statistical analysis of the grain sizes in the microstructure allowed for determination of the grain coarsening temperature as the temperature at which the largest grains differ significantly in size from the average size of all grains in the structure.

4.3.3 Recrystallization Forging Trials

The recrystallization forging trials were designed to determine the T_{95} temperature, also typically referenced to as the T_{RX} temperature, which is as defined in section 2.3.2. For production in the RCF processing schedule, this temperature represents the minimum temperature for hot forging of the steels using RCF processing.

For these experiments, 12mm diameter by 18mm length cylinders were machined from the hot rolled steels. The geometry of these samples is displayed in Figure 46. The steels were first reheated for 5 minutes at 25°C below the grain coarsening temperature determined during the grain coarsening trials. This was accomplished following the procedure established in section 4.3.2. The steel samples were then reheated to 1150°C in a clam shell furnace at a heating rate of 5°C/s and held for 1 minute. Following the holding, the samples were cooled at 10°C/s to the forging temperatures, forged 50% in compression at $5s^{-1}$, starting at 1100°C, and decreasing 50°C each trial, until the recrystallization-stop or T_5 temperature was found. Following forging, the samples were water quenched to room temperature, mounted in Bakelite mounting powder, and picric etched according to the procedure detailed in section 4.1.1. The microstructures were then analyzed to determine the percentage of the microstructure which was non-recrystallized.

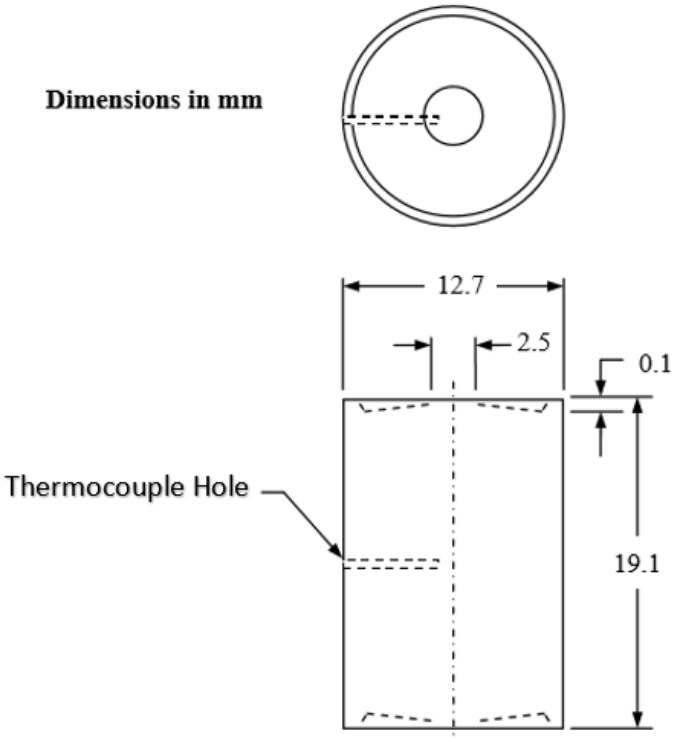

Figure 46: Forging cylinder sample geometry

4.4 Cooling Experiments

4.4.1 Standard Processing Procedure

The cooling experiments were designed to determine the optimal cooling paths for production of the desired microstructure and property combinations: ferrite/pearlite (low strength, high toughness), bainite (medium strength, medium toughness), and martensite (high strength, low toughness). Due to this, the goal of the trials was not to determine the relevant transformation temperatures, but to determine cooling paths which provided significant quantities of the relevant phase.

For these experiments, the sample geometry and procedure detailed in section 4.3.3 was used, up to the conclusion of the forging pass. Having determined that the minimum temperature for full recrystallization after a 50% compression forging blow resided below 900°C in each steel, 900°C was selected as the forging temperature for the standard processing for the cooling experiments. Upon completion of the forging pass, the cooling paths detailed in sections 4.4.2, 4.4.3 and 4.4.4 commenced.

4.4.2 Air Cooling Experiments

The objective of the air-cooling experiments was to produce a predominantly ferrite/pearlite final microstructure, with low strength and high toughness values.

For these experiments, the steels followed the standard processing procedure detailed in section 4.4.1. Following the final forging blow, the steel samples were rotated out of the clamshell furnace to allow them to air cool to room temperature. This cooling path produced an approximate cooling rate of 1°C/s through the transformation temperature regime. Following cooling, the samples were prepared for optical microscopy according to the Nital etching procedure detailed in section 4.1.1. These optical micrographs were analyzed using ImageJ analysis software for ferrite phase percentage, average equivalent grain diameter and standard deviation of the ferrite grains. Finally, the samples were resurfaced according to the procedure in section 4.1.1, and Vickers Hardness testing was conducted according to the procedure in section 4.2.3.

4.4.3 Water Quenching Experiments

The objective of the water-quenching experiments was to produce a predominantly martensitic final microstructure, with high strength and low toughness values.

For these experiments, the samples from section 4.3.3 which were forged at 900°C were utilized, as they had already undergone the required processing to form a martensitic microstructure. These samples were resurfaced and Nital etched according to the procedures in section 4.1.1. Optical micrographs were then recorded. Following this, the samples were resurfaced once more, and Vickers hardness testing was conducted according to the procedure in section 4.2.3.

4.4.4 Bainitic Cooling Experiments

The objective of the bainitic cooling experiments was to produce a predominantly Bainitic final microstructure, with medium strength and medium toughness values.

For these experiments, the steels followed the standard processing procedure detailed in section 4.4.1. Following the forging blow, the steel samples were helium convection cooled in the clamshell furnace at approximately 30°C/s to 500°C. Following the cooling, the steels were held at 500°C for 110 seconds, which is the time required for completion of the bainite transformation at 500°C, as predicted through JMATPro simulation software. After completion of the 500°C holding, the samples were water quenched to room temperature within three seconds. The final samples were prepared for optical microscopy according to the mounting and Laperra etching procedures in section 4.1.1. Optical micrographs were analyzed to determine phase percentages, average equivalent grain diameters and standard deviations of the grain sizes. Finally, the samples

were resurfaced according to the procedure in section 4.1.1, and Vickers hardness testing was conducted according to section 4.2.3.

4.5 Full Forging Trials

4.5.1 Standard Full Forging Procedure

Initially, the hot rolled steels, supplied by TIMKENSTEEL Steel Company, in the form of 2.75” by 6” hot rolled rods, were heated to 1150°C in an induction tunnel furnace for 2 minutes. For forging of the 10V40 full wheel hub forging samples, MFC utilizes a 2-pass hot forging schedule, where the first pass occurs between 1050°C and 1075°C, and the second pass occurs between 1000°C and 1025°C. Following forging, the steels are subjected to a final pass with a trimming die, to produce clean final surfaces and edges. Finally, the forgings are cooled using a batch air cool to room temperature, following which, the center column hole is machined out using a punching procedure.

For the experimental steel forgings, the standard procedure is followed up to the second forging pass. Following this pass, the steels are immediately subjected to the cooling paths described in section 4.5.2 and 4.5.3.

4.5.2 Initial Full Forging Experiments

The initial full forging experiments utilized the standard processing procedure described in section 4.5.1. The cooling schedules selected for the initial full forging experiments comprised of

three cooling paths. These cooling paths were a still-air cool to room temperature, a fan-air cool to room temperature, and a water quench to room temperature.

The slowest cooling path, the still air cool to room temperature, was achieved through removing the forging after the second forging pass to an isolated location, where still air at approximately room temperature cooled the sample to room temperature. This cooling path was designed to produce a low-strength, high-toughness condition with a ferrite/pearlite microstructure.

The second cooling path, the fan air cool to room temperature, was achieved through removing the forging after the second forging pass to a table fan setup used at MFC. This cooling path was designed to produce a medium-strength, medium-toughness condition with a ferrite/pearlite microstructure with a refined ferrite average grain diameter.

The fastest cooling path, the water quench to room temperature, was achieved through removing the forging after the second forging pass to a room temperature water bath. The forging sample was cooled to room temperature within the bath. This cooling path was designed to produce a high-strength, low toughness condition with a predominantly martensite microstructure.

Following each of these procedures, vertical cuts were performed in the sample to produce profiles, shown in Figure 45. As is seen in Figure 45, the 5 locations denoted in section 4.1.1 were selected for metallographic analysis. At these locations, the relevant analysis techniques described in section 4.1.1 were used to characterize the properties and uniformity of the forging.

4.5.3 Submersive Interrupted Quench Trials

The submersive interrupted quench trials were designed to develop a controllable and easily repeatable intermediate cooling method for production of predominantly bainite

microstructures in the final full forging samples. For this purpose, a hot water quench was investigated to provide cooling fast enough to avoid formation of high temperature phases, yet slow enough to allow for controlled halting of the cooling above the martensite start (M_s) temperature. For these experiments, the apparatus in Figure 47, the Submersive Interrupted Quench Unit (SIQU), was developed, tested and used.

In Figure 47 can be seen several important features, denoted 1 through 4. Labeled 1 is the frame of the unit which the forging is inserted into. Feature 2 denotes the holes in the frame through which the two supporting rods are inserted. Using these rods, the unit is lowered and raised into and from the 30-gallon hot water container. Feature 3 denotes the two heating units which, along with the 2 heating units that are permanently contained within the hot water container, heat the water to approximately 85°C. Feature 4 denotes the full sized steel forging, which is inserted into the frame through the opening opposite of the heating units.

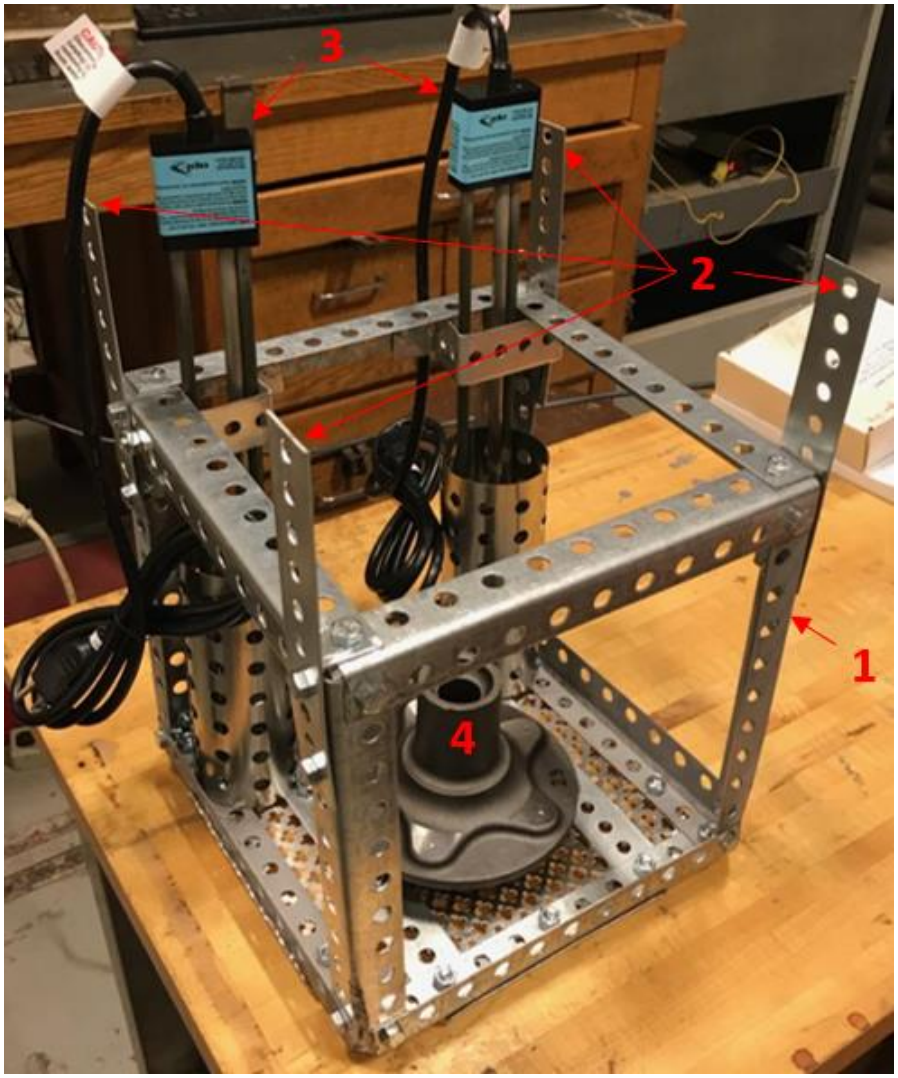

Figure 47: Submersive Interrupted Quench Unit (SIQU)

For these experiments, 2-inch (5.08 cm) diameter by 3 inch (7.62 cm) low carbon steel rods were machined according to Figure 48. The two thermocouple holes were monitored to generate temperature profiles throughout the experiment at the center (1.0-inch hole) and the half radius (0.5-inch hole) depths.

To begin, these steels were brought to 1000°C (the approximate start temperature for the full forging cooling path) in a convection furnace for 20 minutes. Following this heating, the steels were submerged in the 85°C water bath for variable time periods. After quenching for the determined time periods, the samples were removed from the quench and allowed to air cool to room temperature. The temperature profile of these cooling paths was analyzed, and subsequent trial quench times were adjusted until a proper quench time was found. This quench time was determined by choosing the quench time which allowed both thermocouples' positions the largest time within the bainite temperature regime, predicted using JMATPro.

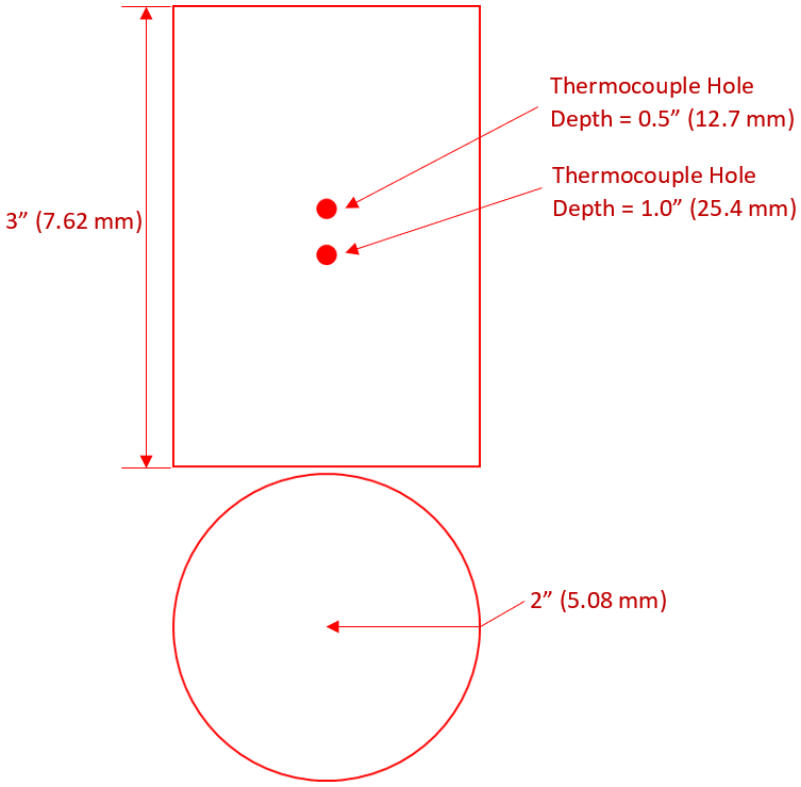

Figure 48: Submersive interrupted quench test samples

4.5.4 Full Forging Hot Water Quench Trials

The hot water quench forging trials were forged according to the standard processing procedure described in section 4.5.1, with a determined goal of producing a predominantly bainite microstructure. The cooling schedules selected for these experiments were selected based upon the results of the experiments detailed in section 4.5.3. Here, 27 seconds was selected as the proper submersion time for producing bainite, and 50 seconds was selected for cooling through the bainite temperature regime.

For the 27 second hot water quenching experiments, the steels were removed from the second forging pass, and immediately transferred into the SIQU frame, as described in section

4.5.3. This process occurred within approximately five seconds. Once inserted, the SIQU unit was lowered into the 85°C water bath, and a timer was started at the moment of complete submersion of the forging. After 27 seconds, the unit was lifted from the bath, and the sample was removed from the unit and allowed to air cool to room temperature. The purpose of this trial was to keep the sample within the bainite regime long enough to produce a predominantly bainite microstructure.

For the 50 second hot water quenching experiments, the steels used a process identical to the 27 second trial, except a 50 second quench time was used in place of the previous 27 second quench time. The purpose of this trial was to cool the sample through the bainite regime at an accelerated rate which is slower than cold water quenching, yet faster than air cooling methods, producing a mixed microstructure of bainite and martensite.

The forgings produced with this method were machined according to the method described in section 4.5.2. The samples produced with this method were then analyzed using the preparation and microscopy techniques detailed in section 4.1.1.

5.0 Results

5.1 BAMPRI Laboratory Simulation Trials

5.1.1 Results of Initial Convection Furnace Heating Trials

The results of the initial convection furnace heating trials consist of thermocouple temperature profiles which are presented in Figure 49. Values extracted from these trials are shown in Table 5. Here it can be seen that the laboratory forging samples reliably come to 1150°C within 180 seconds of insertion into the preheated furnace. Additionally, the experiments demonstrated that laboratory forging samples can be cooled within 7 seconds to room temperature using submersion water quenching.

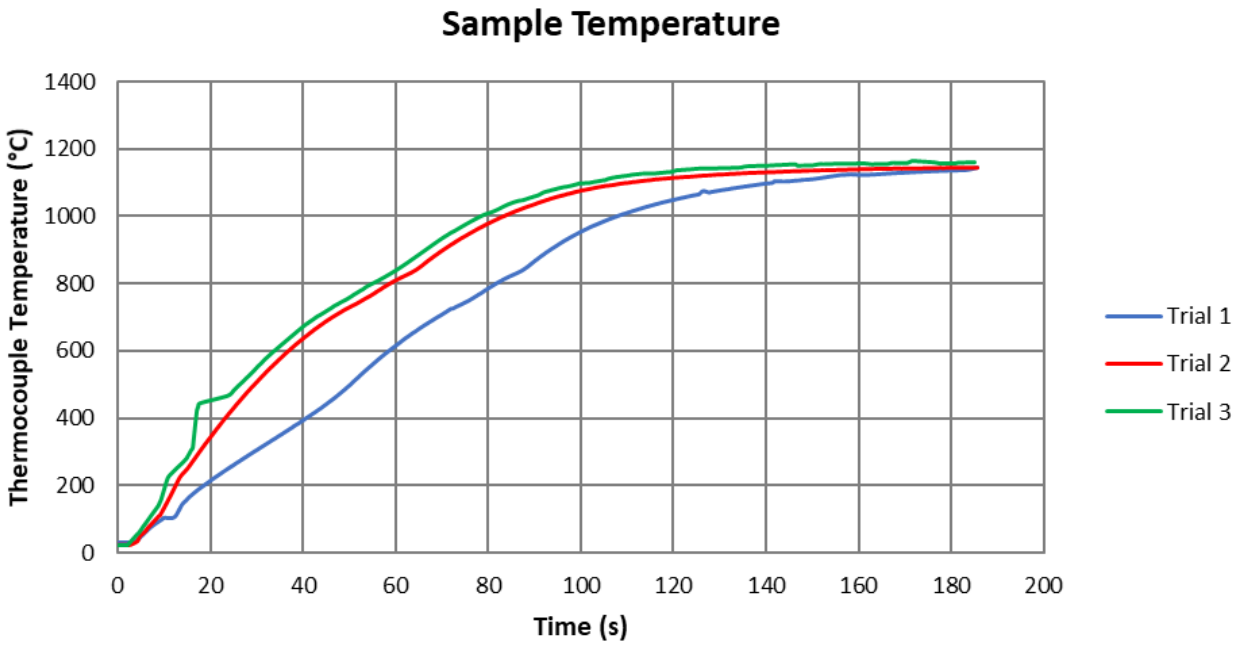

Figure 49: Initial convection furnace heating trial temperature profile

Table 5: Initial convection furnace heating trial temperature profile values

	RT → 1125 time (s)	1125 → 200 time (s)	Linear Heatup Rate (°C/s)	Linear Quench Rate (°C/s)
Test 1	162.2	4.9	6.75	-188.78
Test 2	126.6	6.6	8.65	-140.15
Test 3	109.2	6.65	10.03	-139.10

5.1.2 Results of Grain Coarsening Trials

The results of the grain coarsening trials, detailed in section 4.3.2, are shown in the following.

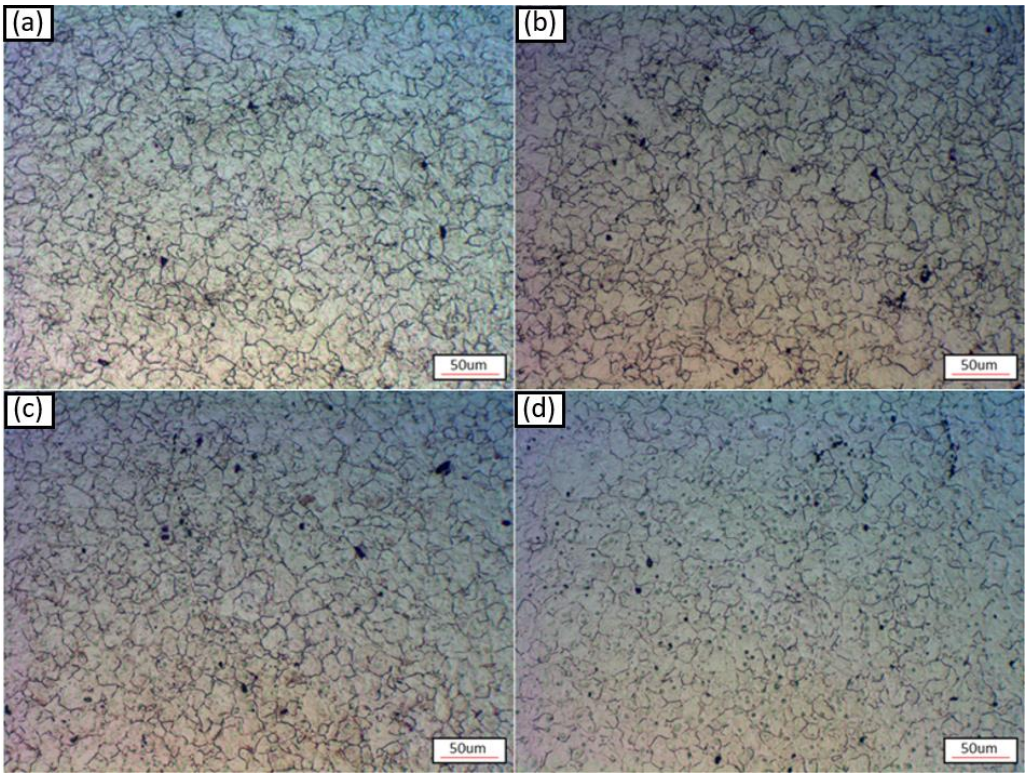

Figure 50: Picric etched steel M1 grain coarsening samples after reheating at (a) 950°C, (b) 1000°C, (c) 1050°C and (d) 1100°C for 5 minutes, and water quenching to room temperature. Images taken at 400 times magnification.

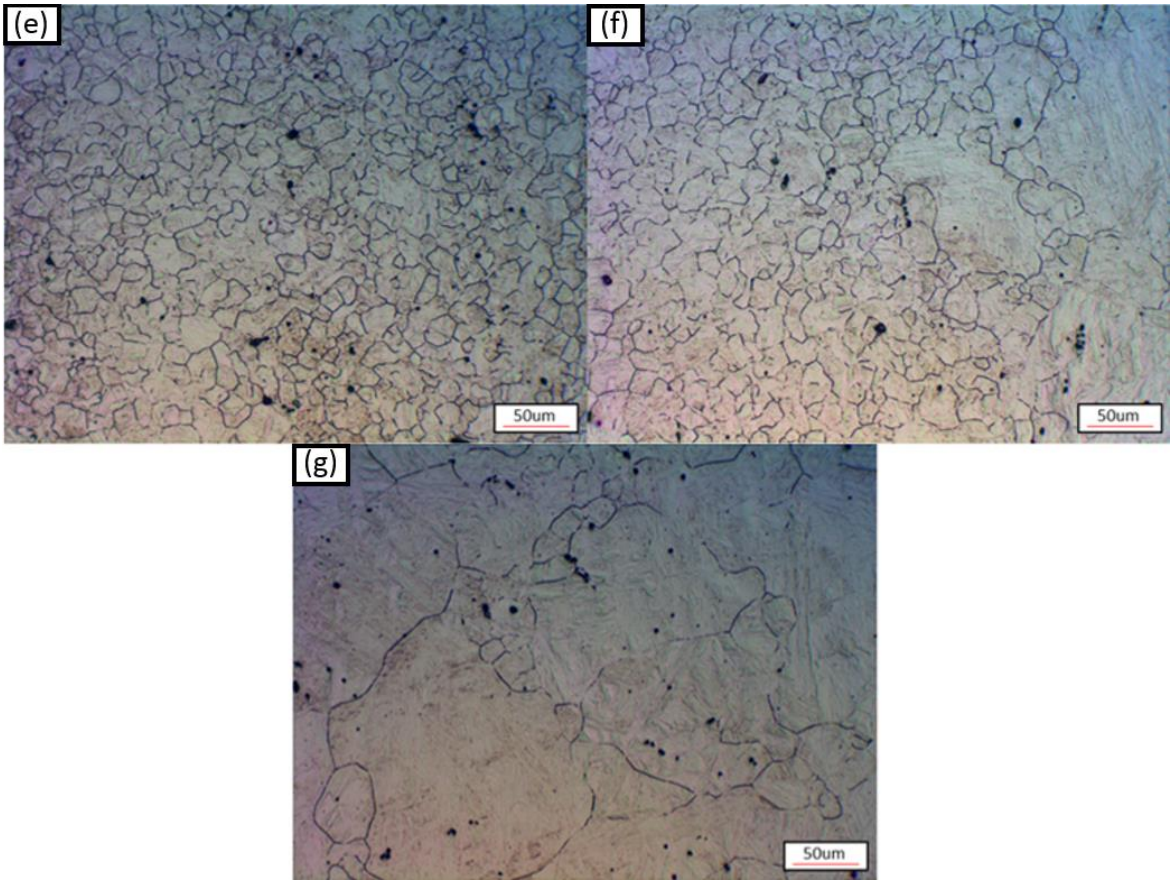

Figure 51: Picric etched steel M1 grain coarsening samples after reheating at (e) 1150°C, (f) 1200°C and (g) 1250°C for 5 minutes, and water quenching to room temperature. Images taken at 400 times magnification.

Figures 50 and 51 show the picric etched images for the reheat trials of steel M1 from temperatures 950°C through 1250°C at 400X magnification. The relevant statistical data for these images, and for the other steels in the project are shown in Table 6. Additionally, Figure 52 plots the average grain diameter of all austenite grains for each temperature in red and the average of the largest austenite grain diameters (all grains two standard deviations larger or more than the average grain diameter) in blue. While the largest increase in grain size occurs from 1200°C to 1250°C, the two curves first deviate significantly from 1150°C to 1200°C. The very large standard

deviations observed at high temperatures in Table 6 is indicative of mixtures of large and small grains suggesting the presence of abnormal grain growth at these temperatures.

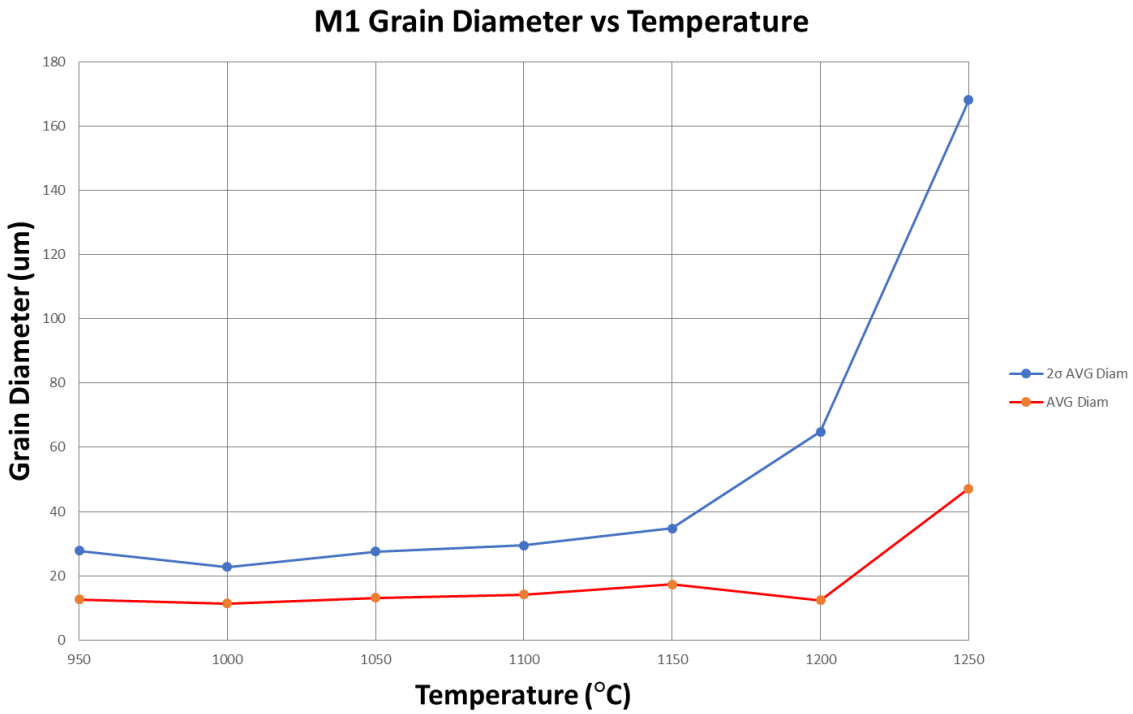

Figure 52: Steel M1 reheat samples prior austenite average grain diameter (Red) and average diameter of austenite grains more than two standard deviations larger than the average diameter of all austenite grains (Blue).

Table 6: Grain coarsening trial average austenite grain diameter and standard deviation for steels 10V40, M1-M3, T1 and T2

	950°C (µm)	1000°C (µm)	1050°C (µm)	1100°C (µm)	1150°C (µm)	1200°C (µm)	1250°C (µm)
10V40	10.95 ± 6.78	11.76 ± 5.76	12.81 ± 5.20	30.64 ± 17.53	59.31 ± 30.47	73.69 ± 27.66	95.90 ± 48.05
M1	12.60 ± 5.43	11.43 ± 4.68	13.21 ± 5.58	14.18 ± 6.05	17.38 ± 6.57	12.38 ± 9.64	47.14 ± 41.43
M2	13.17 ± 5.94	13.52 ± 6.38	13.39 ± 6.12	13.42 ± 5.73	14.84 ± 6.30	21.27 ± 8.83	24.94 ± 13.34
M3	9.82 ± 4.46	9.81 ± 4.69	9.10 ± 3.85	11.25 ± 5.44	10.97 ± 4.79	10.72 ± 5.35	34.22 ± 39.96
T1	7.05 ± 3.12	9.88 ± 4.85	11.55 ± 5.43	22.25 ± 9.76	26.31 ± 15.62	63.34 ± 42.62	-
T2	10.84 ± 5.33	11.06 ± 4.23	12.51 ± 5.72	44.71 ± 25.68	85.45 ± 40.25	88.60 ± 47.99	-

Table 7: Grain coarsening and reheat temperatures for steels 10V40, M1-M3, T1 and T2. The minimum reheat temperature for the MFC processing is 1150°C

	10V40	M1	M2	M3	T1	T2
T_{GC} (°C)	1100	1200	1200	1250	1200	1100
T_{RH} (°C)	1150	1175	1175	1225	1175	1150

Table 7 shows the T_{GC} and T_{RH} for each of the steels in the experiment. Note that the T_{RH} is determined as 25°C below the T_{GC}. However, if the T_{RH} suggested by the laboratory experiment is below 1150°C (the MFC process reheating temperature), the T_{RH} for the steel was instead selected as 1150°C.

5.1.3 Results of Recrystallization Forging Trials

The results of the recrystallization forging trials, detailed in section 4.3.3, are shown here. Figures 53 and 54 reveal the prior austenite grain structure of the samples. As can be seen, as the temperature decreases, the microstructure generally becomes more refined, and additionally becomes less recrystallized. This is seen specifically in Figure 54 in (g), for the M1 steel deformed at 800°C. Here, the majority of grains are not equiaxed/circular in shape, signifying the suppression of recrystallization in the steel at this temperature.

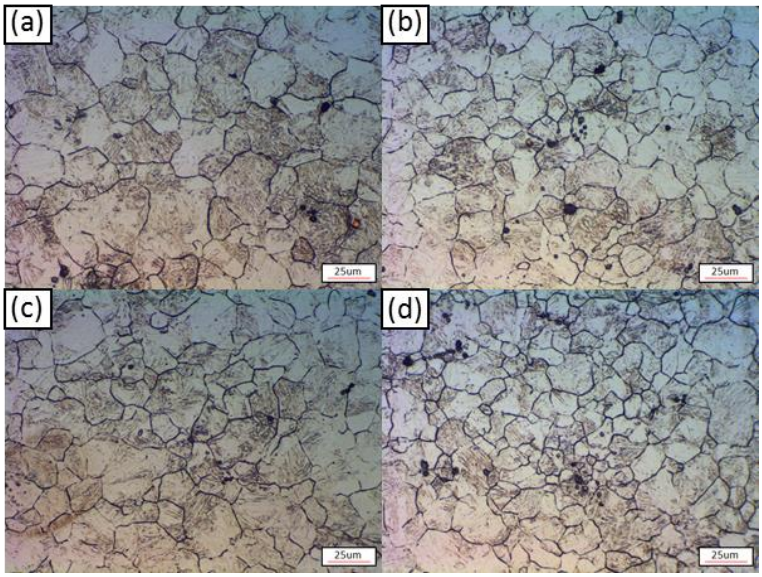

Figure 53: Picric etched steel M1 recrystallization forging trial samples after forging 50% at (a) 1100°C, (b) 1050°C, (c) 1000°C and (d) 950°C, followed by water quenching to room temperature. Images taken at 1000 times magnification.

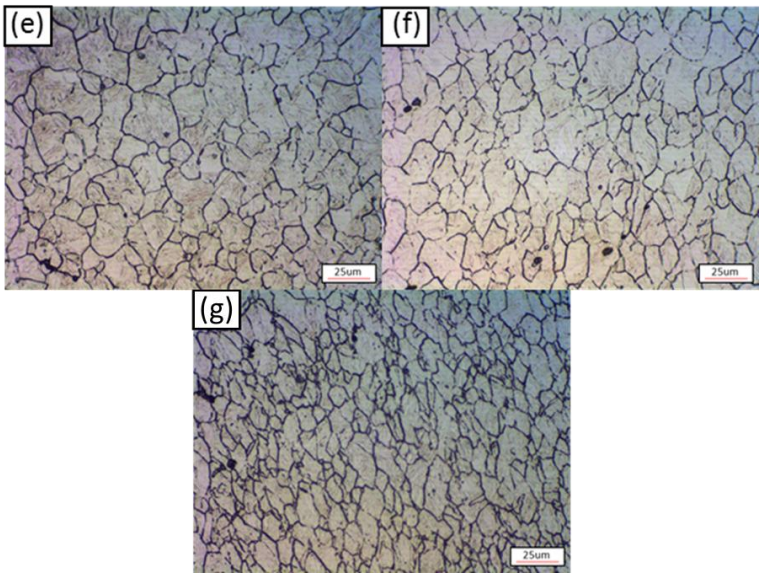

Figure 54: Picric etched steel M1 recrystallization forging trial samples after forging 50% at (e) 900°C, (f) 850°C and (g) 800°C, followed by water quenching to room temperature. Images taken at 1000 times magnification.

Table 8 displays the average diameter of the prior austenite grains for the trials, while Table 9 displays the temperature at which full recrystallization stops (T_{95}) for each of the steels.

Table 8: Recrystallization forging trial post forging prior austenite grain diameter and standard deviation for experimental steels.

	900°C (µm)	850°C (µm)	800°C (µm)	775°C (µm)	750°C (µm)
M1	8.63 ± 6.22	12.05 ± 3.35	8.87 ± 3.13	7.93 ± 3.10	-
M2	11.22 ± 9.71	10.43 ± 4.63	10.73 ± 2.38	9.40 ± 2.87	7.45 ± 3.27
M3	10.24 ± 4.78	8.24 ± 3.73	9.72 ± 4.03	8.09 ± 3.62	-
T1	9.74 ± 5.16	11.23 ± 5.90	11.03 ± 6.55	-	-
T2	11.71 ± 6.11	15.11 ± 9.00	29.70 ± 15.63	-	-

Table 9: Recrystallization forging trial determined T_{95} for experimental steels

	M1	M2	M3	T1	T2
T_{95} (°C)	850	800	850	800	800

5.1.4 Results of Cooling Experiments

The results of the cooling experiments, detailed in section 4.3.4, are presented here. Tables 10 and 11 list the important values determined from the experiments. Here, α denotes the ferrite

samples, α_B denotes the bainite samples, and α' denotes the martensite samples. Additionally, RT represents room temperature, ACRT represents air cooling to room temperature and WQRT represents water quenching to room temperature.

Table 10: Laboratory cooling experiments data for experimental steels M1, M2 and M3

	M1			M2			M3		
Phase	α	α_B	α'	α	α_B	α'	α	α_B	α'
Cool Rate (°C/s)	ACRT	30	WQRT	ACRT	30	WQRT	ACRT	30	WQRT
WET (°C)	RT	500	RT	RT	500	RT	RT	500	RT
VHN	216.1	243.1	444.0	213.5	216.9	446.5	234.0	269.07	437.8

Table 11: Laboratory cooling experiments data for experimental steels T1 and T2

	T1			T2		
Phase	α	α_B	α'	α	α_B	α'
Cool Rate (°C/s)	ACRT	30°C/s	WQRT	ACRT	30°C/s	WQRT
WET (°C)	RT	500°C	RT	RT	500°C	RT
VHN	235.8	264.6	479.4	209.2	244.4	463.8

Figure 55 displays the final microstructures of steel M1 laboratory cooling experiments. Here, (a) shows the ACRT structure processed according to section 4.4.2, (b) shows the bainite structure processed according to section 4.4.3, and (c) shows the martensite structure processed according to section 4.4.4.

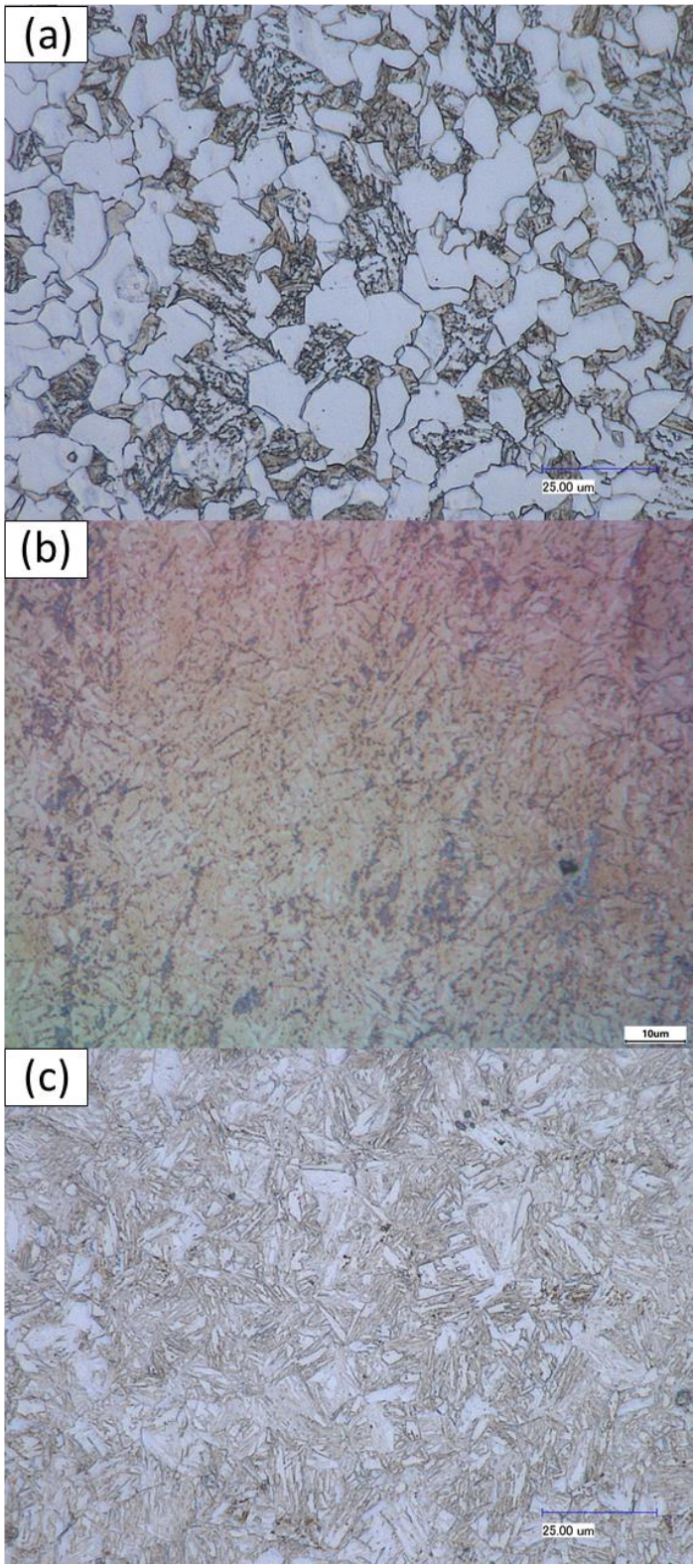

Figure 55: Steel M1 laboratory cooling experiments (a) ferrite ACRT, (b) bainite 30°C/s cool and (c) martensite WQRT

5.1.5 Results of Submersive Interrupted Quench Trials

The results of the subversive interrupted hot water quench trials are shown here. The procedure for these experiments is detailed in section 4.5.3. Figure 56 below shows the initial experiments, where a cold water quench, a long (40 seconds) hot water quench, several short (10 seconds or less) hot water quenches, and air cooling trials were conducted.

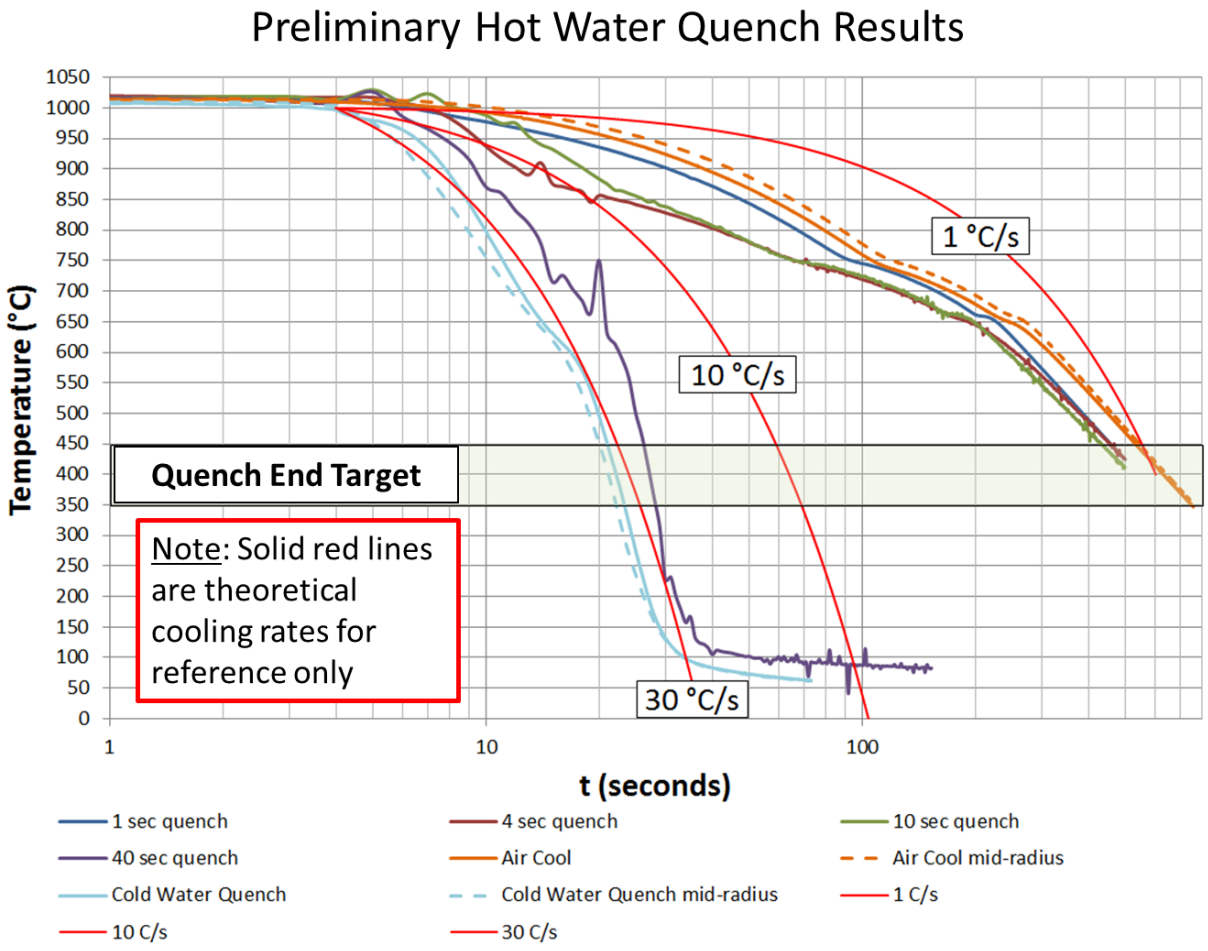

Figure 56: Preliminary hot water quench results with initial quench end target temperature range

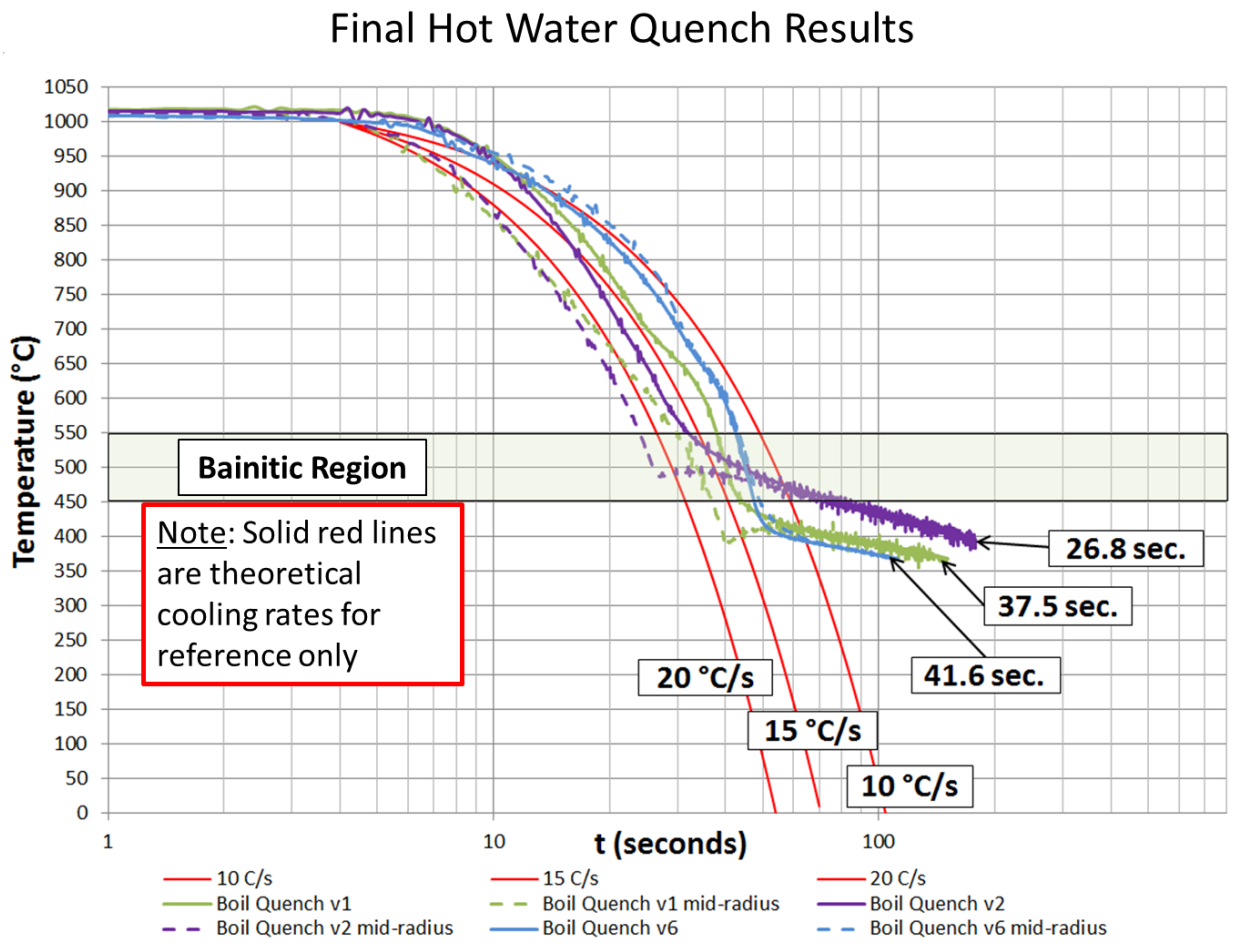

Figure 57: Final hot water quench results with predicted bainite formation region

Figure 57 shows the final hot water quench temperature profiles. These intermediate quench times were designed to determine the optimal quenching time to keep the sample within the bainite formation temperature range for as long as possible. As can be seen, the 27 second hot water quench trial keeps the sample within the target temperature range from 30 seconds (just after removal from quench) to 80 seconds. Additionally, the 42 second trial brings the sample below the M_s temperature within 50 seconds, estimating that a 50 second quench trial would bring the sample below the M_s before the end of the quench.

5.2 MFC Full Forging Trials

5.2.1 Initial Full Forging Trials

The results of the initial full forging trials, detailed in sections 4.5.1 and 4.5.2, are presented here. Figure 45 in section 4.2.1 labels the positions in the forging from which the metallographic micrographs and hardness measurements were taken. Figure 58 shows the micrographs taken from the air-cooled forging for steel M1.

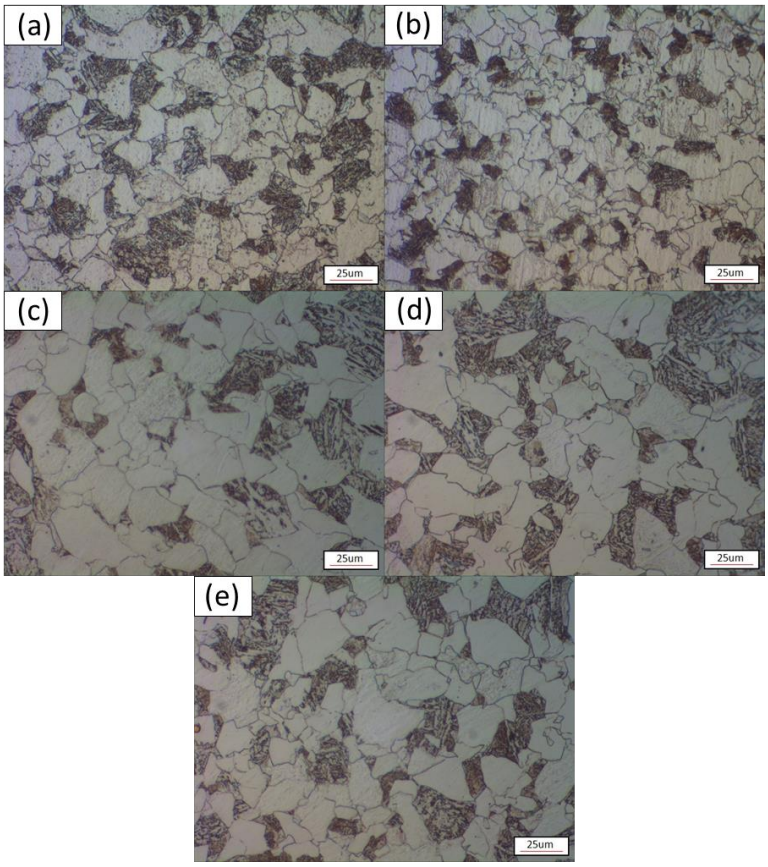

Figure 58: Steel M1 ACRT full forging (a) location 1, (b) location 2, (c) location 3, (d) location 4 and (e) location 5 according to Figure 45

Figure 59 shows the micrographs taken from the fan air-cooled forging for steel M1. Additionally, Figure 60 displays the micrographs taken from the water quenched forging for steel M1. Tables 12, 13 and 14 show the measured Vickers hardness values for each location of each of the steel conditions, with the suffix S representing slow ACRT (still air cool), F representing fast ACRT (fan air cool) and Q representing cold water quenched (WQRT).

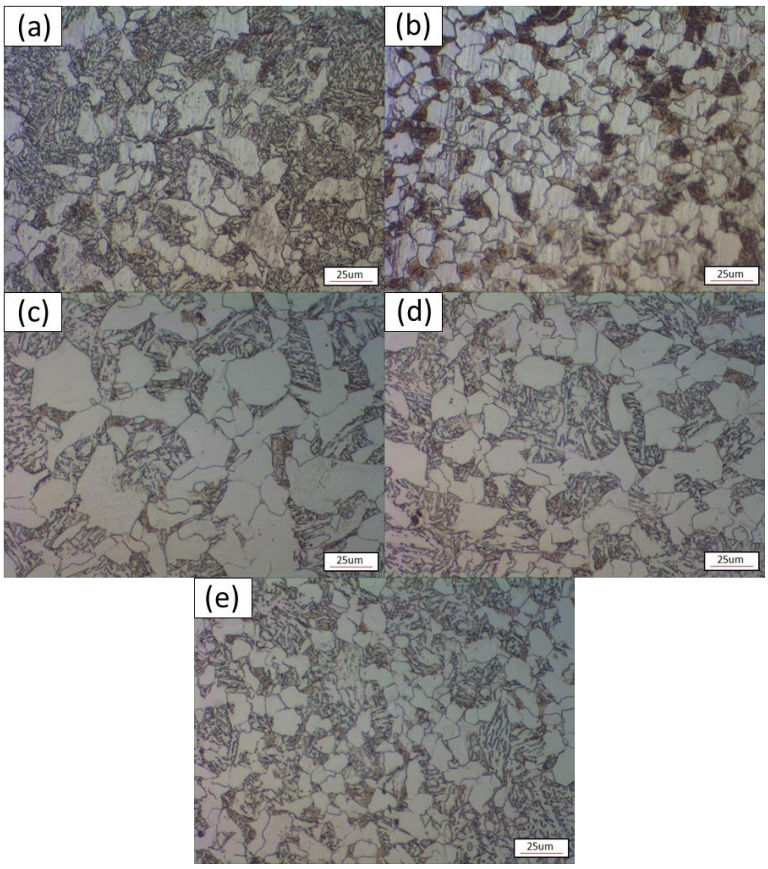

Figure 59: Steel M1 fan ACRT full forging (a) location 1, (b) location 2, (c) location 3, (d) location 4 and (e) location 5 according to Figure 45

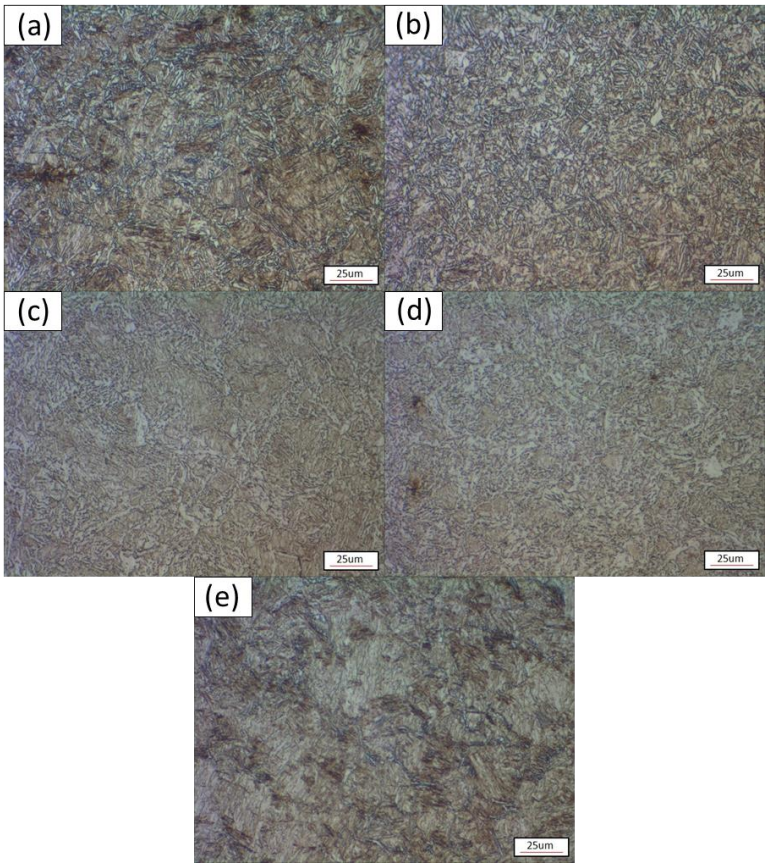

Figure 60: Steel M1 WQRT full forging (a) location 1, (b) location 2, (c) location 3, (d) location 4 and (e) location 5 according to Figure 45

Table 12: Slow ACRT condition forging average hardness values according to Figure 45

	Location 1 (VHN)	Location 2 (VHN)	Location 3 (VHN)	Location 4 (VHN)	Location 5 (VHN)	Average (VHN)
M1_S	234.7	213.7	197.4	228.4	203.7	215.6
M2_S	207.1	206.2	188.0	203.3	171.0	195.1
M3_S	245.8	254.3	227.5	233.8	218.2	235.9
T1_S	214.9	218.9	251.7	222.4	227.5	227.1
T2_S	264.9	255.8	258.5	265.8	255.7	260.1

Table 13: Fast ACRT condition forging average hardness values according to Figure 45

	Location 1 (VHN)	Location 2 (VHN)	Location 3 (VHN)	Location 4 (VHN)	Location 5 (VHN)	Average (VHN)
M1_F	234.7	288.0	219.5	247.9	278.0	253.6
M2_F	212.5	193.0	192.7	208.0	201.3	201.5
M3_F	285.0	266.9	272.7	249.3	270.9	269.0
T1_F	236.3	231.2	234.9	231.9	189.3	224.7
T2_F	256.3	263.1	254.3	253.6	252.9	256.0

Table 14: Cold WQRT condition forging average hardness values according to Figure 45

	Location 1 (VHN)	Location 2 (VHN)	Location 3 (VHN)	Location 4 (VHN)	Location 5 (VHN)	Average (VHN)
M1_Q	405.5	334.0	316.9	314.7	443.6	362.9
M2_Q	359.1	340.5	327.3	301	399.8	345.5
M3_Q	386.5	357.7	302.3	310.5	455.5	362.5
T1_Q	469.8	435.4	380.5	424.5	476.2	437.3
T2_Q	452.2	443.2	353.2	365.8	433.5	409.6

In addition to hardness measurements, tensile and charpy testing were performed according to sections 4.2.1 and 4.2.2. Tables 15, 16 and 17 below display the tensile and charpy data for the experimental steels, compared to the data for the standard steel, 10V40. Here, the suffix of A and B at the end of the sample names represents duplicate trials, taken from the same location and condition.

Table 15: Slow ACRT condition forging mechanical properties, tensile properties extracted at location 4 and charpy properties extracted at location 1, according to sections 4.2.1 and 4.2.2

	Total Elongation (%)	UTS (MPa)	(UTS*TE) (MPa*%)	CVN (J)
10V40_ACRT	25.3	780.2	19800	15.6
				12.9
M1_S_A	34.0	605.4	20600	23.7
M1_S_B	34.5	607.1	21000	20.3
M2_S_A	39.7	555.8	22000	25.8
M2_S_B	39.0	553.4	21600	27.1
M3_S_A	33.1	643.9	21300	20.3
M3_S_B	32.5	645.4	21000	20.3
T1_S_A	32.6	654.9	21400	27.1
T1_S_B	35.0	646.9	22700	25.1
T2_S_A	27.4	777.7	21300	17.6
T2_S_B	29.1	773.3	22500	19.0

Table 16: Fast ACRT condition forging mechanical properties, tensile properties extracted at location 4 and charpy properties extracted at location 1, according to section 4.2.1 and 4.2.2

	Total Elongation (%)	UTS (MPa)	(UTS*TE) (MPa*%)	CVN (J)
10V40_ACRT	25.3	780.2	19800	15.6
				12.9
M1_F_A	34.5	667.2	23000	19.7
M1_F_B	32.7	659.3	21500	
M2_F_A	34.9	604.0	21100	27.8
M2_F_B	38.1	616.3	23500	24.4
M3_F_A	32.0	704.9	22600	21.7
M3_F_B	30.1	718.5	21600	22.4
T1_F_A	31.0	676.3	21000	22.4
T1_F_B	30.5	675.0	20600	25.1
T2_F_A	31.6	762.6	24100	20.3
T2_F_B	33.0	756.2	25000	18.3

Table 17: Cold WQRT condition forging mechanical properties, tensile properties extracted at location 4 and charpy properties extracted at location 1, according to section 4.2.1 and 4.2.2

	Total Elongation (%)	UTS (MPa)	(UTS*TE) (MPa*%)	CVN (J)
10V40_ACRT	25.3	780.2	19800	15.6
				12.9
M1_Q_A	19.8	826.1	16300	16.3
M1_Q_B	21.0	849.9	17900	14.9
M2_Q_A	27.7	795.1	22100	17.0
M2_Q_B	27.3	789.2	21600	17.0
M3_Q_A	19.9	885.3	17600	17.6
M3_Q_B	21.1	938.7	19800	17.6
T1_Q_A	12.6	1297.6	16400	16.3
T1_Q_B	16.9	1397.4	23700	17.0
T2_Q_A	10.7	1417.2	15200	12.2
T2_Q_B	9.0	1412.1	12700	12.9

Figures 61, 62 and 63 display the tensile curves for each steel in the slow ACRT, fast ACRT and cold WQRT condition, respectively. As can be seen, many samples offer various improvements over the currently used 10V40 steel.

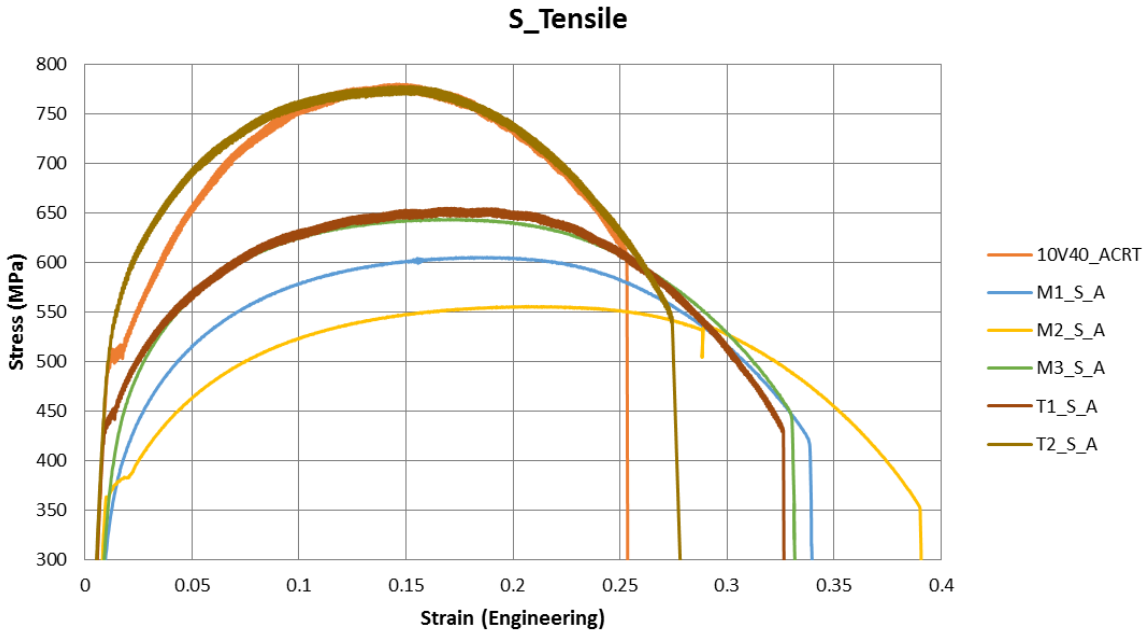

Figure 61: Slow ACRT condition forging tensile curves, extracted at location 4, according to section 4.2.1

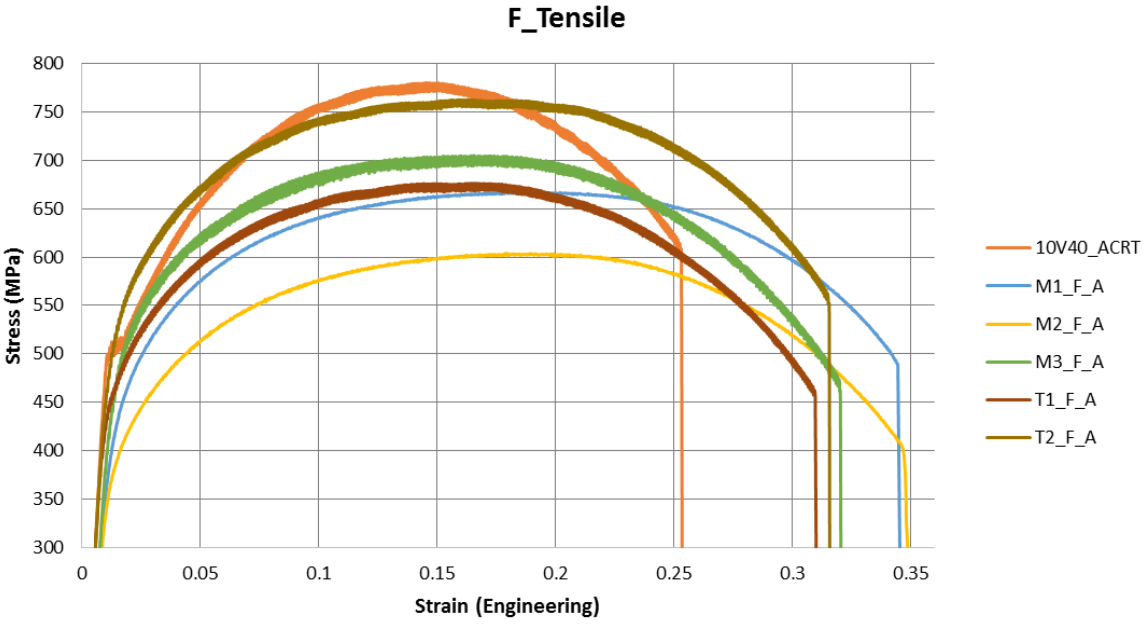

Figure 62: Fast ACRT condition forging tensile curves, extracted at location 4, according to section 4.2.1

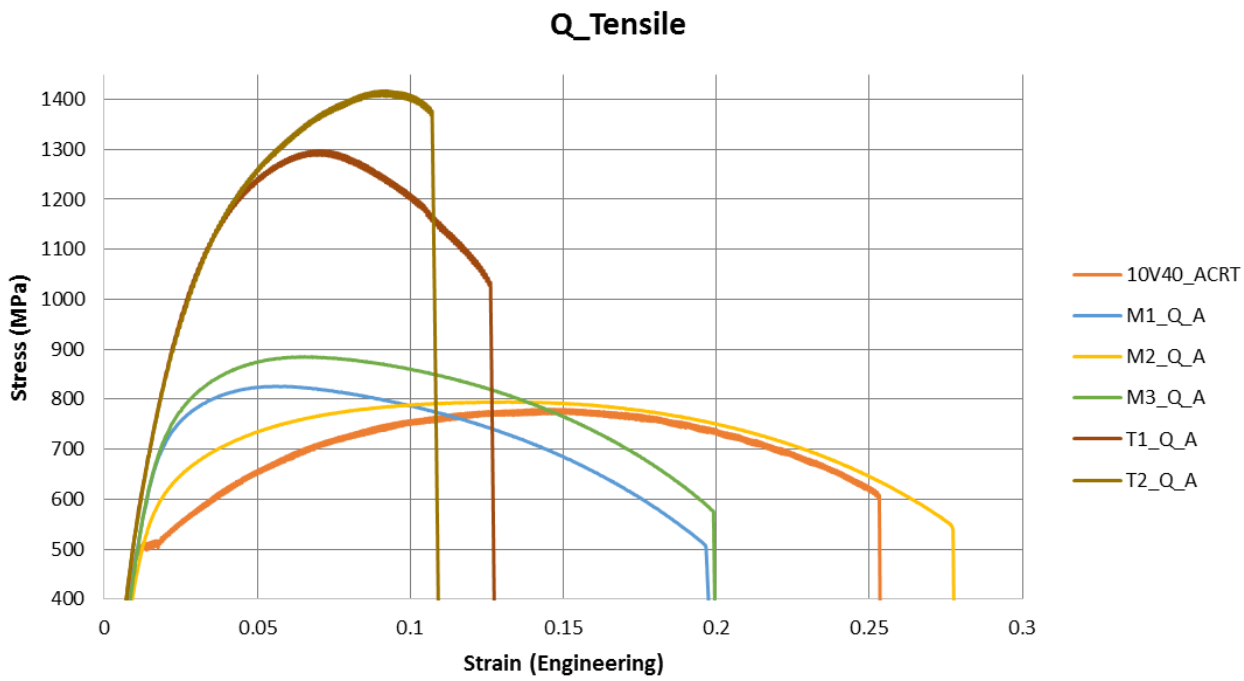

Figure 63: Cold WQRT condition forging tensile curves, extracted at location 4, according to section 4.2.1

Tables 18-21 show the measured data for the ferrite microstructures (slow and fast ACRT conditions) in the steel. Here was measured the average equivalent circular ferrite grain diameter. Additionally, Table 22 displays the measured data for the martensite microstructures (cold WQRT conditions). Here was measured the average equivalent circular prior austenite grain diameter at each location.

Table 18: Slow ACRT condition forging average equivalent ferrite grain diameter at each location for each tested steel

	Location 1 (µm)	Location 2 (µm)	Location 3 (µm)	Location 4 (µm)	Location 5 (µm)	Average (µm)
M1_S	10.12	8.42	14.31	11.50	11.35	11.14
M2_S	8.42	12.03	11.96	11.38	9.30	10.62
M3_S	9.84	8.25	11.11	11.89	8.85	9.99
T1_S	8.71	9.65	13.36	9.21	8.74	9.93
T2_S	7.23	7.00	6.84	7.21	6.41	6.94

Table 19: Slow ACRT condition forging ferrite phase percentage at each location for each tested steel

	Location 1 (α %)	Location 2 (α %)	Location 3 (α %)	Location 4 (α %)	Location 5 (α %)	Average (α %)
M1_S	67.50	78.53	72.56	65.57	69.34	70.70
M2_S	78.20	78.33	79.10	74.07	81.50	78.24
M3_S	69.35	79.74	68.83	71.78	74.60	72.86
T1_S	53.87	61.61	42.56	67.39	70.41	59.17
T2_S	41.10	54.58	25.89	60.37	49.46	46.28

Table 20: Fast ACRT condition forging average equivalent ferrite grain diameter at each location for each tested steel

	Location 1 (μm)	Location 2 (μm)	Location 3 (μm)	Location 4 (μm)	Location 5 (μm)	Average (μm)
M1_F	8.06	8.39	12.55	10.13	8.15	9.46
M2_F	8.36	7.35	11.14	12.66	8.56	9.61
M3_F	8.05	7.68	11.10	10.79	8.01	9.13
T1_F	8.81	8.39	9.67	7.90	7.05	8.36
T2_F	7.98	6.65	8.46	6.87	6.44	7.28

Table 21: Fast ACRT condition forging ferrite phase percentage at each location for each tested steel

	Location 1 (α %)	Location 2 (α %)	Location 3 (α %)	Location 4 (α %)	Location 5 (α %)	Average (α %)
M1_F	74.16	65.77	59.82	49.93	46.78	59.29
M2_F	72.92	76.44	80.65	74.96	73.58	75.71
M3_F	51.97	74.01	55.60	48.86	49.10	55.91
T1_F	31.95	47.65	28.51	50.93	32.24	38.26
T2_F	19.48	40.16	27.03	51.68	34.57	34.58

Table 22: Cold WQRT condition forging average equivalent prior austenite grain diameter at measurable locations for each tested steel

	Location 1 (μm)	Location 2 (μm)	Location 3 (μm)	Location 4 (μm)	Location 5 (μm)	Average (μm)
M1_Q	14.00	12.74	-	-	-	-
M2_Q	14.29	11.55	-	-	-	-
M3_Q	13.06	9.96	-	-	-	-
T1_Q	26.03	22.30	29.00	17.96	19.76	23.01
T2_Q	33.55	22.52	-	20.37	18.03	-

5.2.2 Results of Full Forging Hot Water Quench Trials

The results of the full forging hot water quench trials, detailed in section 4.5.4, are contained here. Figures 64 and 65 show the microstructures of steel M1 for the 27 second hot water quench and the 50 second hot water quench, respectively. Additionally, Table 23 shows the hardness measurements for the 27 second quench trials, while Table 24 shows the hardness measurements for the 50 second quench trials.

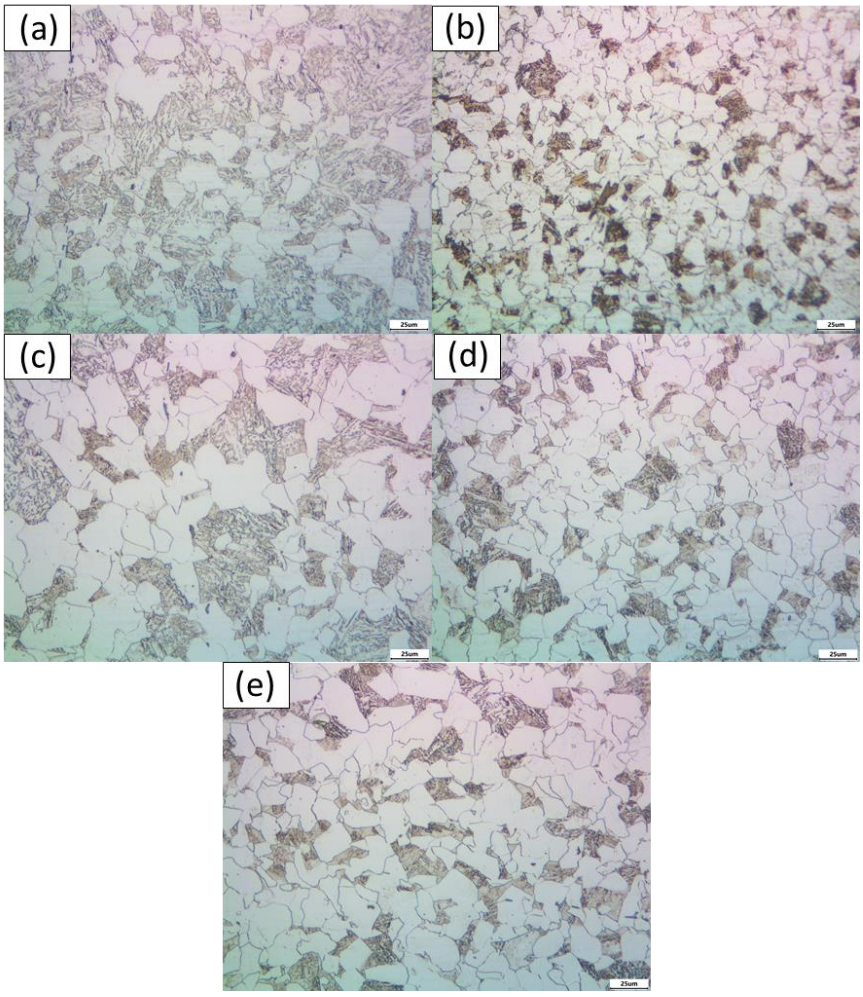

Figure 64: Steel M1 27 second hot water quench (a) location 1, (b) location 2, (c) location 3, (d) location 4 and (e) location 5 according to Figure 45

Table 23: 27 Second hot water quench condition forging bulk hardness values according to Figure 45

	Location 1 (VHN)	Location 2 (VHN)	Location 3 (VHN)	Location 4 (VHN)	Location 5 (VHN)	Average (VHN)
M1_27	233.7	220.9	235.6	220.7	212.8	224.7
M2_27	216.5	186.6	197.3	201.8	203.8	201.2
M3_27	238.2	213.8	221.3	210.4	211.1	219.0

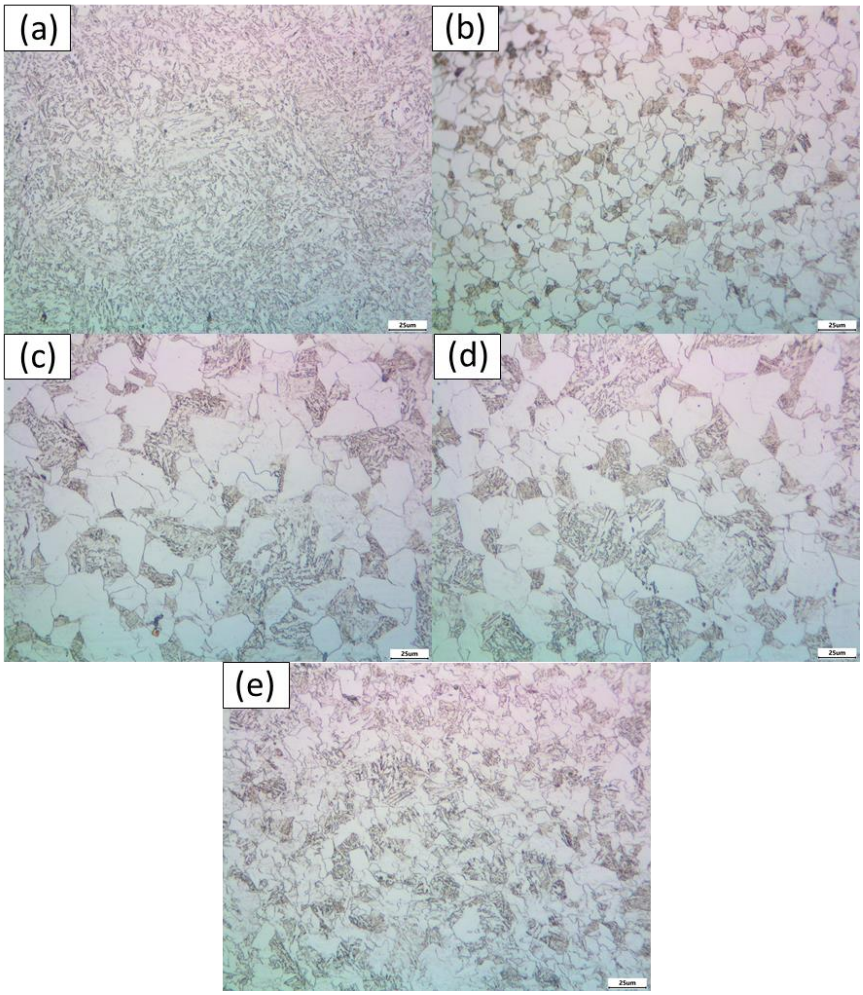

Figure 65: Steel M1 50 second hot water quench (a) location 1, (b) location 2, (c) location 3, (d) location 4 and (e) location 5 according to Figure 45

Table 24: 50 Second hot water quench condition forging bulk hardness values according to Figure 45

	Location 1 (VHN)	Location 2 (VHN)	Location 3 (VHN)	Location 4 (VHN)	Location 5 (VHN)	Average (VHN)
M1_50	252.7	223.3	227.8	223.3	241.3	233.7
M2_50	203.8	184.8	180.3	198.0	211.7	195.7
M3_50	263.0	224.6	256.6	250.8	257.1	250.4

Table 25: 27 Second hot water quench condition forging mechanical properties, tensile properties extracted at location 4 and charpy properties extracted at location 1, according to sections 4.2.1 and 4.2.2

	Total Elongation (%)	UTS (MPa)	(UTS*TE) (MPa*%)	CVN (J)
10V40_ACRT	25.3	780.2	19775.8	15.6
				12.9
M1_27	33.17243	634.2925	21041.02	16.95
M1_27	34.43531	622.4262	21433.44	16.95
M2_27	38.73369	559.2078	21660.18	23.73
M2_27	38.82665	553.74	21499.87	25.08
M3_27	37.23913	645.1774	24025.85	24.4
M3_27	34.16703	640.0062	21867.11	23.73

Table 26: 50 Second hot water quench condition forging mechanical properties, tensile properties extracted at location 4 and charpy properties extracted at location 1, according to sections 4.2.1 and 4.2.2

	Total Elongation (%)	UTS (MPa)	(UTS*TE) (MPa*%)	CVN (J)
10V40_ACRT	25.3	780.2	19775.8	15.6
				12.9
M1_50	33.23477	634.1614	21076.21	24.4
M1_50	31.46286	632.0681	19886.67	24.4
M2_50	36.43452	555.1334	20226.02	22.37
M2_50	36.93526	564.2684	20841.4	24.4
M3_50	29.63402	684.3645	20280.47	21.01
M3_50	31.01222	675.2765	20941.82	21.69

Tables 25 and 26 show the mechanical properties of the forgings in the 27 second hot water quench and 50 second hot water quench conditions, respectively. These properties include the values measured from the tensile and charpy samples from sections 4.2.1 and 4.2.2. Figure 66 plots the tensile curves for the steels in the 27 second hot water quench condition, while Figure 67 plots the tensile curves for the steels in the 50 second hot water quench condition.

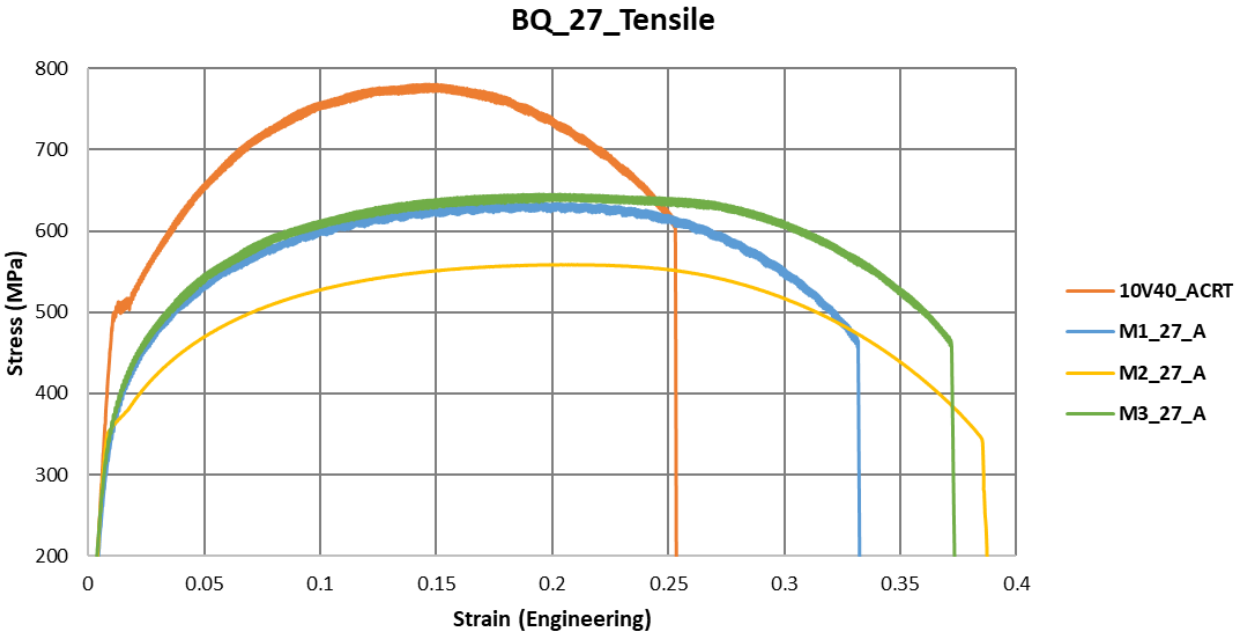

Figure 66: 27 Second hot water quench condition forging tensile curves, extracted at location 4, according to section 4.2.1

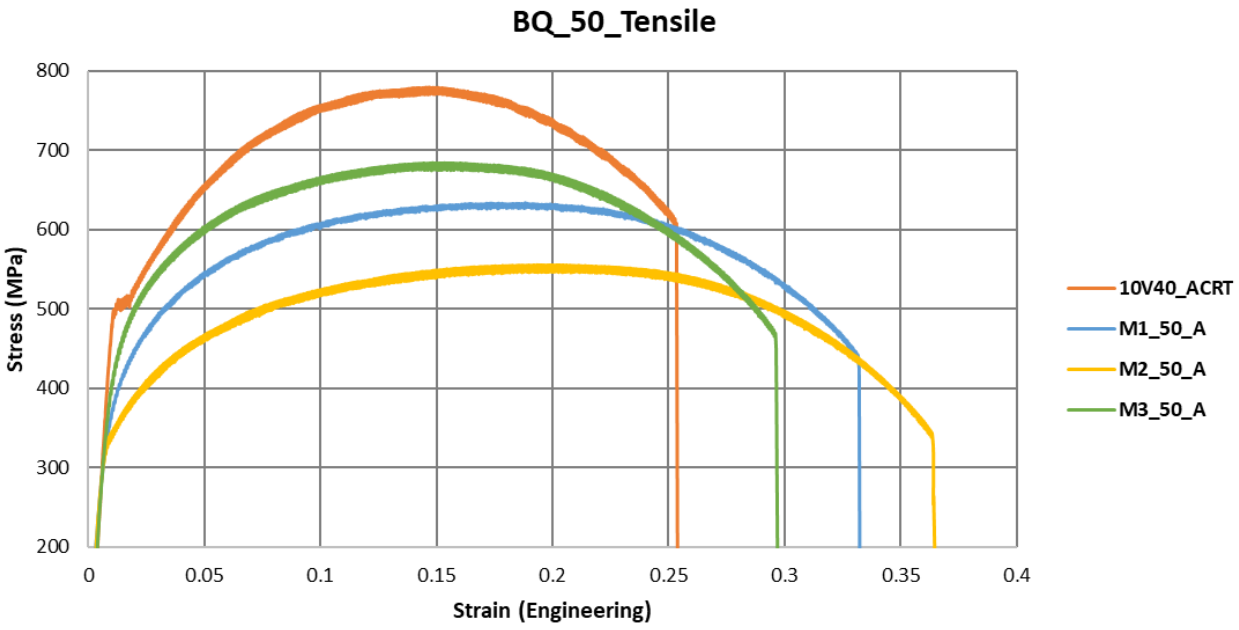

Figure 67: 50 Second hot water quench condition forging tensile curves, extracted at location 4, according to section 4.2.1

Tables 27 and 28 display the measured equivalent circular ferrite grain diameters for the 27 second hot water quench condition and the 50 second hot water quench condition, respectively. Tables 29 and 30 display the polygonal ferrite phase percentage for each hot water quench condition.

Table 27: 27 Second hot water quench condition forging average equivalent ferrite grain diameter at each location for each tested steel

	Location 1 (µm)	Location 2 (µm)	Location 3 (µm)	Location 4 (µm)	Location 5 (µm)	Average (µm)
M1_27	13.02	9.78	14.64	9.66	11.29	11.68
M2_27	14.47	8.21	13.94	10.85	10.43	11.58
M3_27	8.58	9.57	13.47	8.73	8.97	9.86

Table 28: 50 Second hot water quench condition forging average equivalent ferrite grain diameter at each location for each tested steel

	Location 1 (μm)	Location 2 (μm)	Location 3 (μm)	Location 4 (μm)	Location 5 (μm)	Average (μm)
M1_50	-	8.54	12.56	12.90	8.14	10.54
M2_50	10.06	8.21	12.73	9.64	7.38	9.60
M3_50	-	8.66	13.29	8.17	7.34	9.37

Table 29: 27 Second hot water quench condition forging ferrite phase percentage at each location for each steel

	Location 1 (α %)	Location 2 (α %)	Location 3 (α %)	Location 4 (α %)	Location 5 (α %)	Average (α %)
M1_27	44.23	80.15	60.00	75.90	75.82	67.22
M2_27	52.32	81.88	69.58	76.10	81.72	72.32
M3_27	68.00	76.67	57.33	74.50	76.35	70.57

Table 30: 50 Second hot water quench condition forging ferrite phase percentage at each location for each steel

	Location 1 (α %)	Location 2 (α %)	Location 3 (α %)	Location 4 (α %)	Location 5 (α %)	Average (α %)
M1_50	0	78.78	61.92	58.10	40.13	47.79
M2_50	75.01	77.30	73.68	74.32	82.05	76.48
M3_50	0	46.62	31.26	71.88	72.99	44.55

5.3 Results: Advanced Metallographic Analysis

5.3.1 Final Phase Analysis

In analyzing the microstructures of the final samples, proper identification and characterization of the present phases was critical. To this extent, SEM imaging, as well as microhardness measurements, were utilized to analyze each of the intermediate cooling conditions studied. Shown in the figures on the following pages are SEM micrographs for the intermediate cooling conditions for steel M3. As can be seen in Figures 68 through 69, the microstructures are comprised predominantly of polygonal ferrite, bainitic ferrite and bainite. It can be seen here that the composition of the microstructure favors bainite more in the faster cooling conditions (helium convection cooling and the 50 second hot water quench conditions). Additionally, the non-ferritic phase in the slow cooling condition (fast air cool to room temperature) resembles bainitic-ferrite, while in fast cooling conditions comprises of upper bainite, in addition to bainitic ferrite.

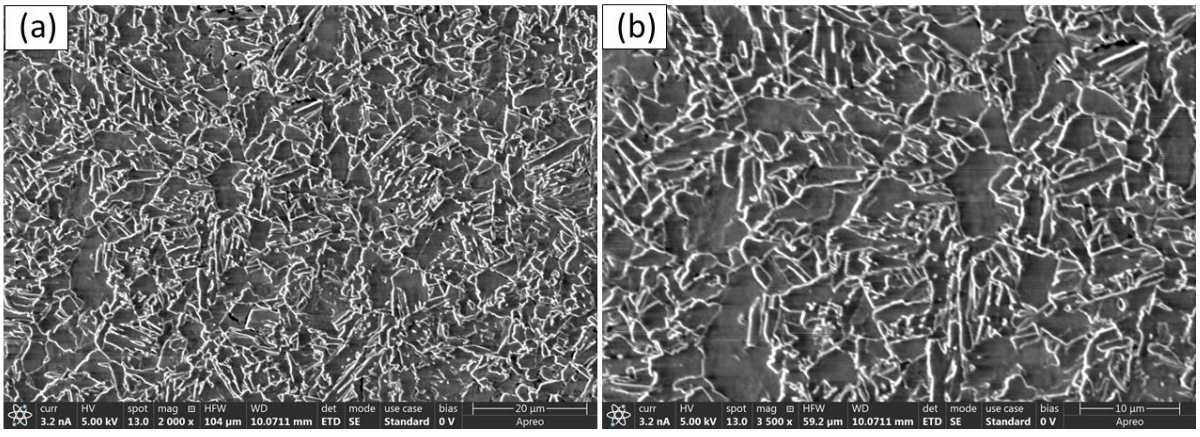

Figure 68: Steel M3 bainite laboratory sample SEM micrographs of non-polygonal ferrite phase (Nital etch) at 2000X (a) and 3500X (b) magnifications

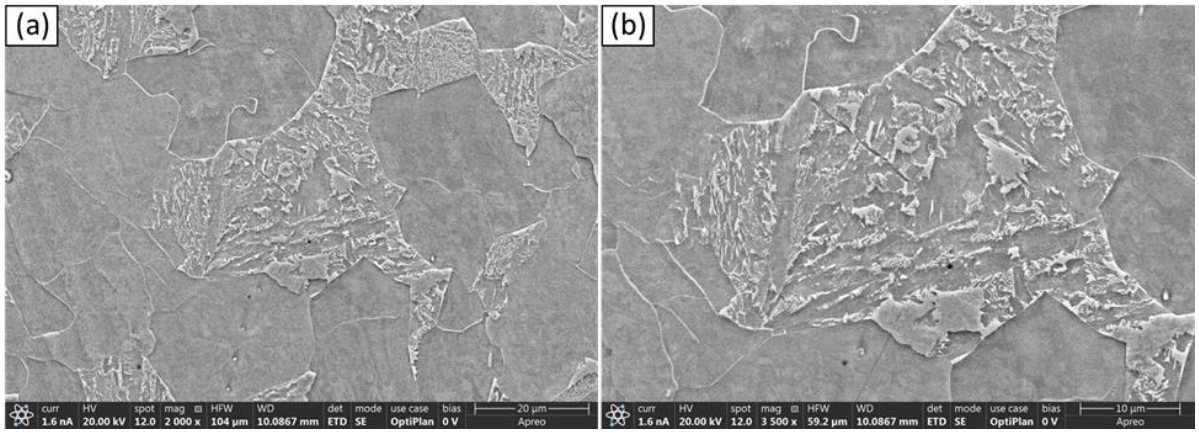

Figure 69: Steel M3 slow ACRT full forging location 4 SEM images of non-polygonal ferrite phase (Nital etch) at 2000X (a) and 3500X (b) magnifications

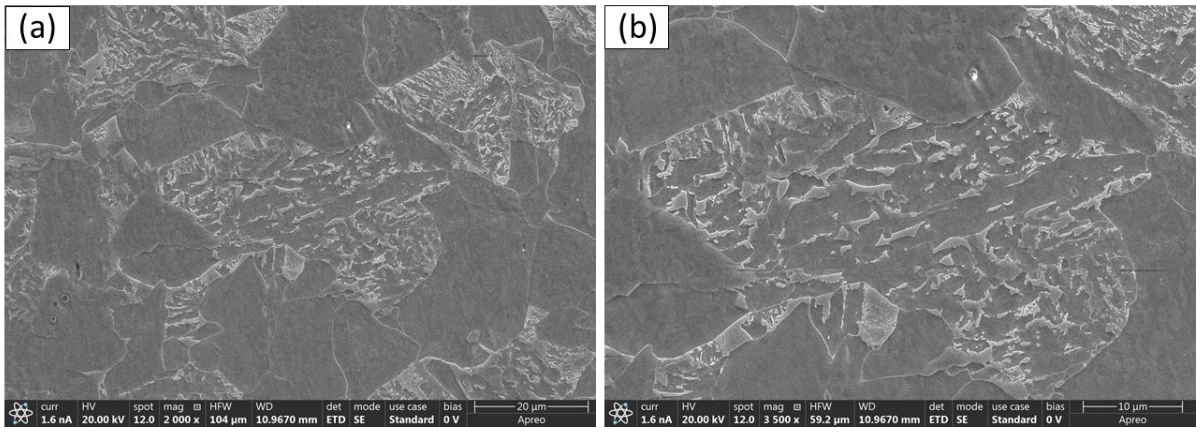

Figure 70: Steel M3 fast ACRT full forging location 4 SEM images of non-polygonal ferrite phase (Nital etch) at 2000X (a) and 3500X (b) magnifications

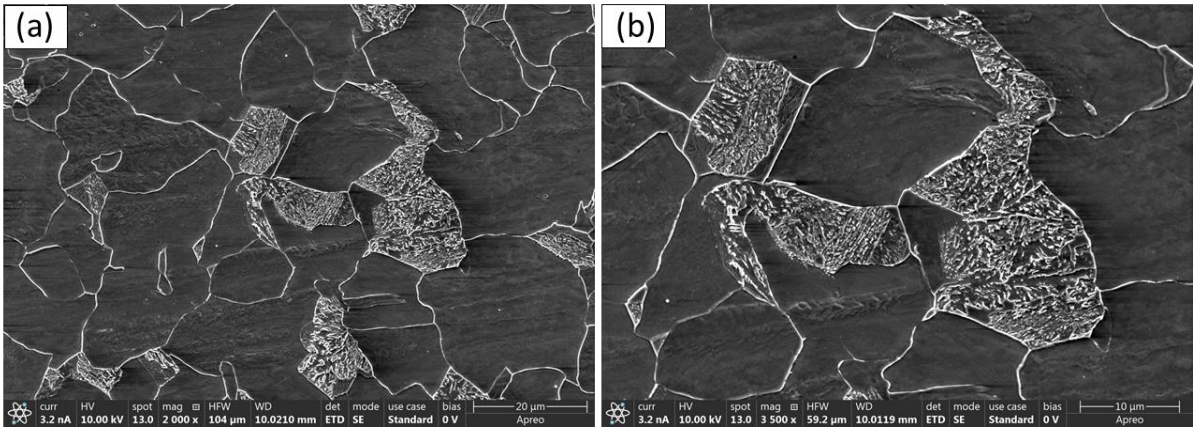

Figure 71: Steel M3 27 seconds hot water quench full forging location 4 SEM images of non-polygonal ferrite phase (Nital etch) at 2000X (a) and 3500X (b) magnifications

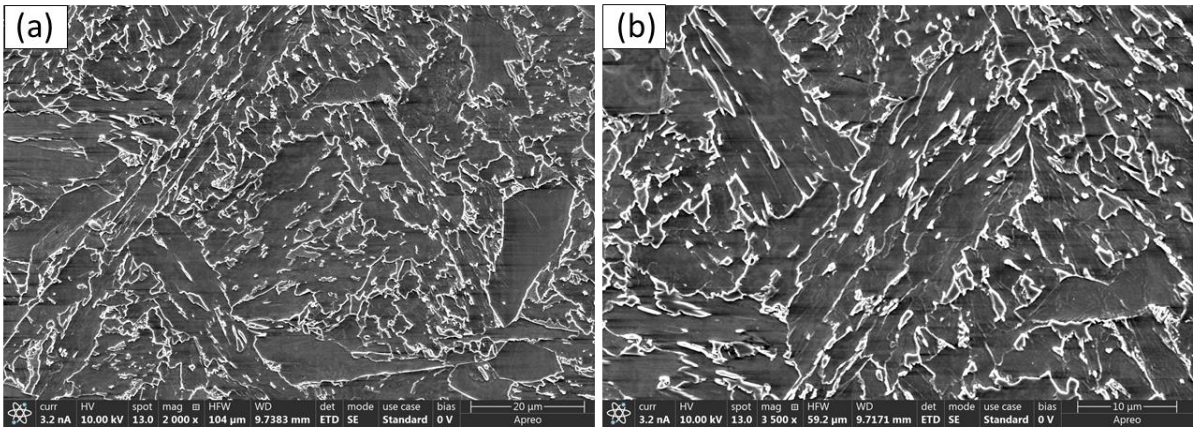

Figure 72: Steel M3 50 seconds hot water quench full forging location 4 SEM images of non-polygonal ferrite phase (Nital etch) at 2000X (a) and 3500X (b) magnifications

Figures 73 through 76 show the results of several micro-hardness (10gf Vickers hardness indents) analysis tests in the intermediate cooling conditions of steel M3. The micro-hardness measurements were made on Nital or Lapera etched samples, in order to selectively test the phases in each steel. Table 31 lists the average micro-hardness values of the phases in each steel, as well as the bulk (300gf) hardness values and the phase percentages at the same location and forging condition.

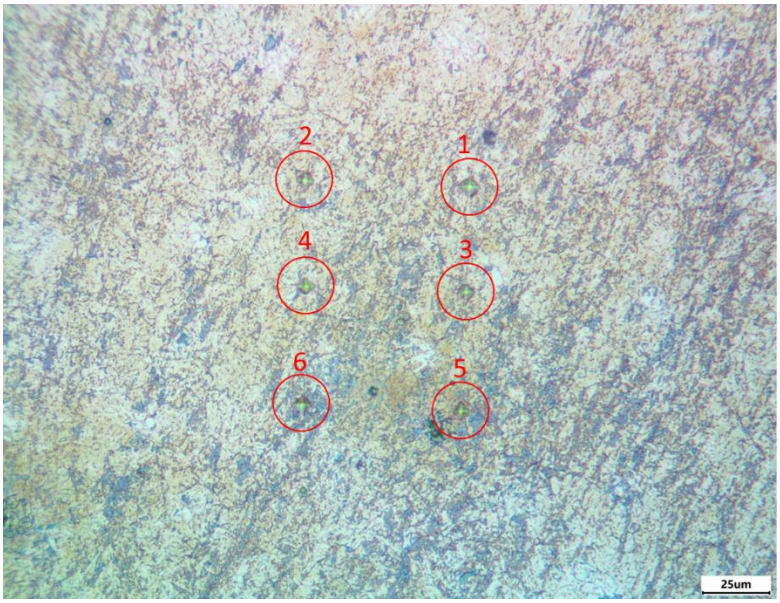

Indent 1 = 285.5 VHN
Indent 2 = 395.8 VHN
Indent 3 = 393.5 VHN
Indent 4 = 411.3 VHN
Indent 5 = 440.3 VHN
Indent 6 = 381.2 VHN

Tested Hardness = 269.07 VHN

Figure 73: Steel M3 bainite laboratory sample (30°C/s Helium convection cooling to 500°C and isothermal holding for 110 seconds) 10gf microhardness indentations in bainite phases (LaPera etch)

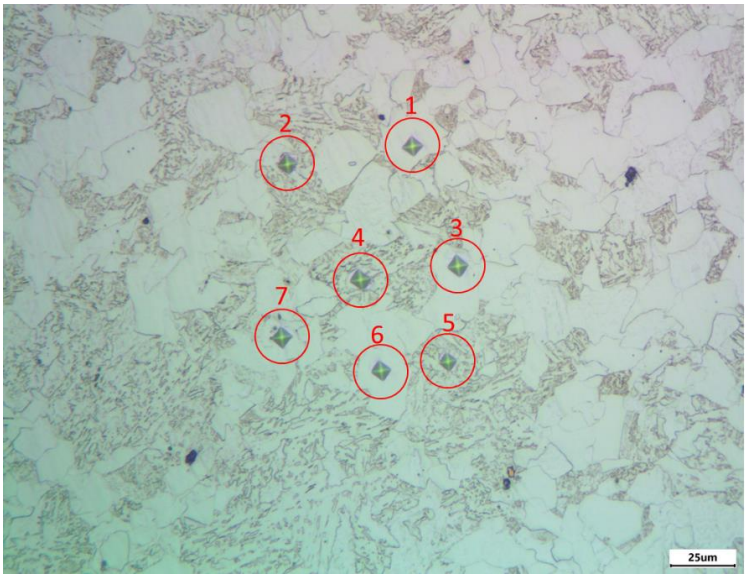

Indent 1 = 253.7 VHN
Indent 2 = 283.7 VHN
Indent 3 = 252.2 VHN
Indent 4 = 244.2 VHN
Indent 5 = 336.4 VHN
Indent 6 = 272.8 VHN
Indent 7 = 253.1 VHN

Location 4 Bulk Hardness = 249.3 VHN

Figure 74: Steel M3 fast ACRT full forging location 4 10gf microhardness indentations in ferrite and bainite phases (Nital etch)

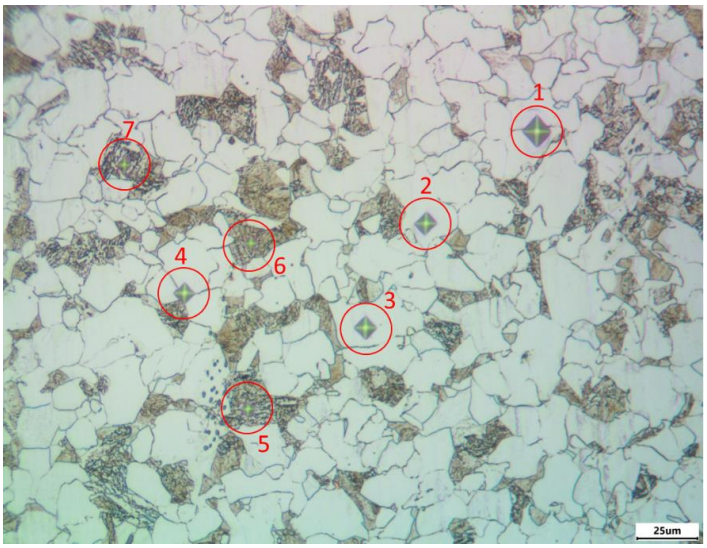

Indent 1 = 121.3 VHN
Indent 2 = 221.0 VHN
Indent 3 = 213.5 VHN
Indent 4 = 229.5 VHN
Indent 5 = 487.9 VHN
Indent 6 = 480.9 VHN
Indent 7 = 409.4 VHN

Location 4 Hardness = 219.0 VHN

Figure 75: Steel M3 27 seconds hot water quench full forging location 4 10gf microhardness indentations in ferrite and bainite phases (Nital etch)

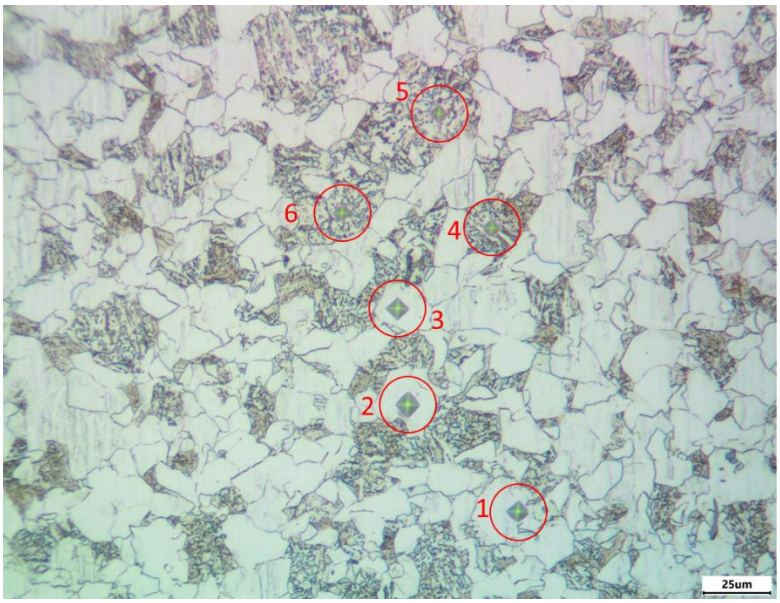

Indent 1 = 266.6 VHN
Indent 2 = 197.9 VHN
Indent 3 = 234.4 VHN
Indent 4 = 397.5 VHN
Indent 5 = 413.7 VHN
Indent 6 = 446.5 VHN

Location 4 Hardness = 250.4 VHN

Figure 76: M3 50 seconds hot water quench full forging location 4 10gf microhardness indentations in ferrite and bainite phases (Nital etch)

Table 31: Steels M1, M2 and M3 full forging microhardness (VHN) phase analysis and phase percentages (%)

M1 Location 4					
	Ferrite (%)	Ferrite (VHN)	Bainite (%)	Bainite (VHN)	Bulk (VHN)
M1_S	65.6	212 ± 14	34.4	389 ± 63	228
M1_F	49.9	238 ± 35	50.1	391 ± 26	248
M1_27	75.9	211 ± 16	24.1	407 ± 46	221
M1_50	58.1	243 ± 11	41.9	379 ± 59	223
M2 Location 4					
	Ferrite (%)	Ferrite (VHN)	Bainite (%)	Bainite (VHN)	Bulk (VHN)
M2_S	74.1	208 ± 19	25.9	400 ± 56	203
M2_F	75	219 ± 24	25	348 ± 46	208
M2_27	76.1	231 ± 17	23.9	379 ± 39	202
M2_50	74.4	239 ± 22	25.7	382 ± 55	198
M3 Location 4					
	Ferrite (%)	Ferrite (VHN)	Bainite (%)	Bainite (VHN)	Bulk (VHN)
M3_S	71.8	209 ± 10	28.2	371 ± 27	218
M3_F	48.9	235 ± 35	51.1	351 ± 39	249
M3_27	74.5	222 ± 8	25.5	441 ± 57	210
M3_50	71.9	241 ± 11	28.1	407 ± 48	251

For reference, in a study by Rodrigues et al.,[67] microstructures consisting of polygonal ferrite, pearlite and granular bainite were obtained at a cooling rate of 1.4°C/s, with a hardness of 224VHN. Additionally, as the cooling rate in the study by Rodrigues et al. increased from 1.4°C/s to 11°C/s (approximately equal to the cooling rates predicted from the hot water quench experiments), the granular bainite in the microstructure increases to 60-70%, and the polygonal ferrite in the steel decreases to 12-20%. It should be noted however that these steels were in a 19mm slab condition, which allows for more accurate controlled cooling throughout the steel.

Figures 77 through 82 display the microhardness (10gf) values for the polygonal ferrite and bainite phases in the steels graphically. In the steels, the 50 second hot water quench condition typically has the highest microhardness in the ferrite, with the slow ACRT condition tending to have the lowest microhardness in the ferrite. For the bainite, steels M1 and M3 have the highest bainite microhardness in the 27 second hot water quench condition, while steel M2 has the highest bainite microhardness value in the fast ACRT condition. The lowest bainite microhardness for each steel in the full forging conditions tends to be in the slow ACRT cooling condition.

Figures 83 through 88 display the microhardness values for the polygonal ferrite and bainite phases as a function of the phase percentage of the respective phase in each condition. Steel M2 shows minimal changes in the phase percentages between the cooling conditions and as such shows no clear trend involving the microhardness values and phase percentages of ferrite and bainite. In contrast, steels M1 and M3, with higher hardenability values than steel M2, show significant changes in phase percentages with cooling rate, and additionally exhibit trends between microhardness and phase percentage, specifically in the bainite. As seen in Figures 86 and 88, as the bainite phase percentage in the steel at location 4 increases, the hardness of the bainite decreases. Additionally, in steel M1, with the standard Vanadium level, the ferrite phase

microhardness decreases as the phase percentage of the ferrite increases. However, this same trend is not observed in steel M3, with the higher Vanadium levels.

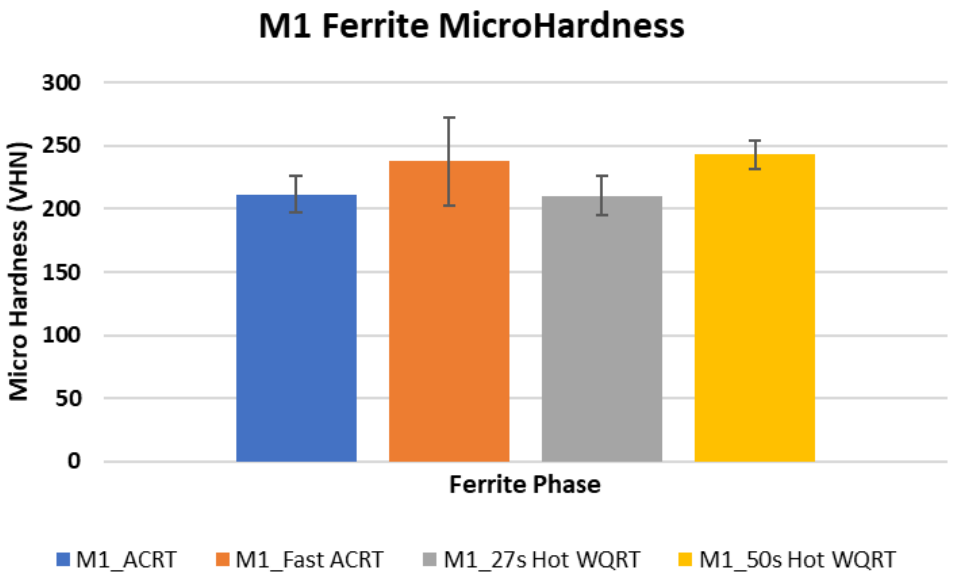

Figure 77: Steel M1 ferrite microhardness values (VHN) at location 4 for ACRT (Left), fast ACRT (Second from left), 27 seconds hot water quench (Second from right) and 50 seconds hot water quench (Right) forging conditions

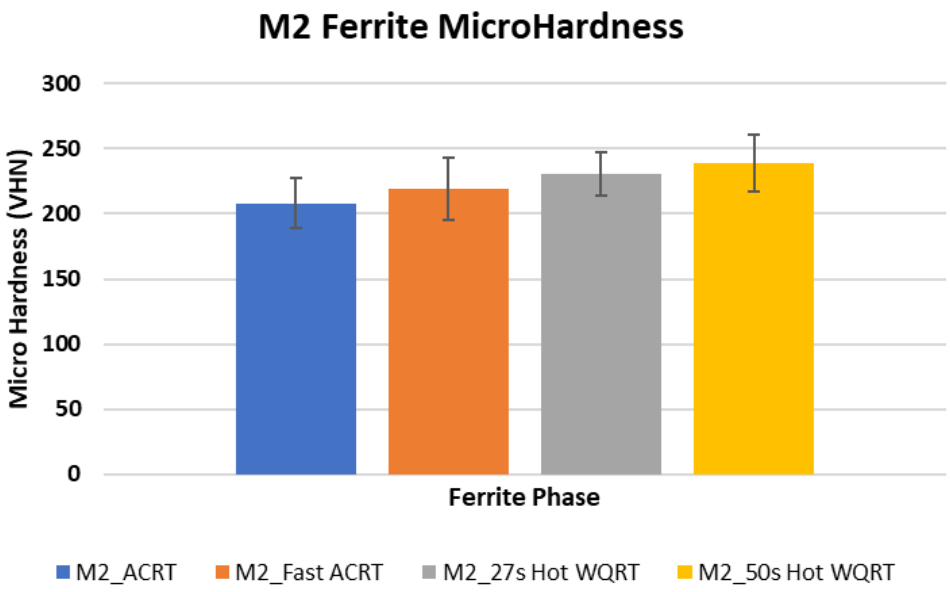

Figure 78: Steel M2 ferrite microhardness values (VHN) at location 4 for ACRT (Left), fast ACRT (Second from left), 27 seconds hot water quench (Second from right) and 50 seconds hot water quench (Right) forging conditions

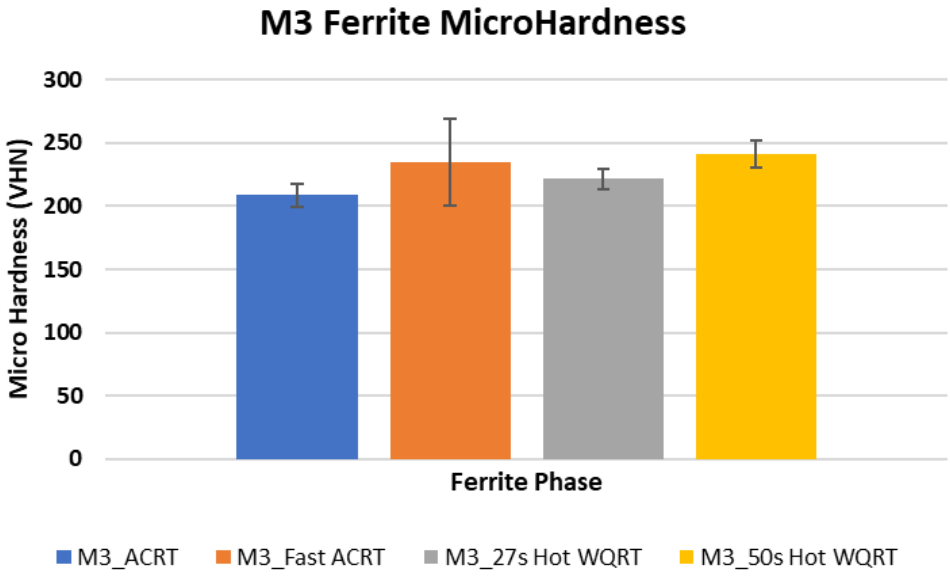

Figure 79: Steel M3 ferrite microhardness values (VHN) at location 4 for ACRT (Left), fast ACRT (Second from left), 27 seconds hot water quench (Second from right) and 50 seconds hot water quench (Right) forging conditions

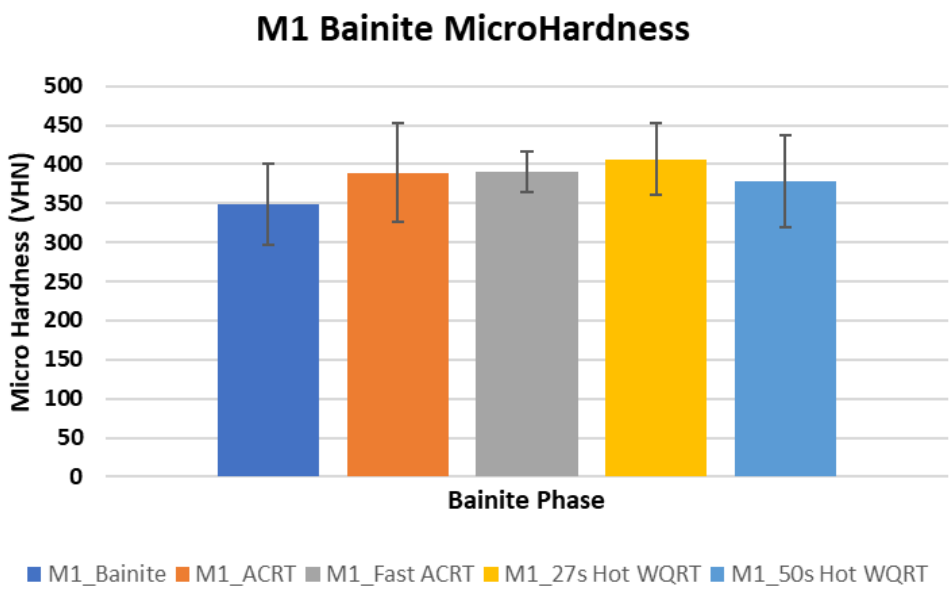

Figure 80: Steel M1 bainite microhardness values (VHN) at location 4 for ACRT (Left), fast ACRT (Second from left), bainite laboratory sample (Center), 27 seconds hot water quench (Second from right) and 50 seconds hot water quench (Right) forging conditions

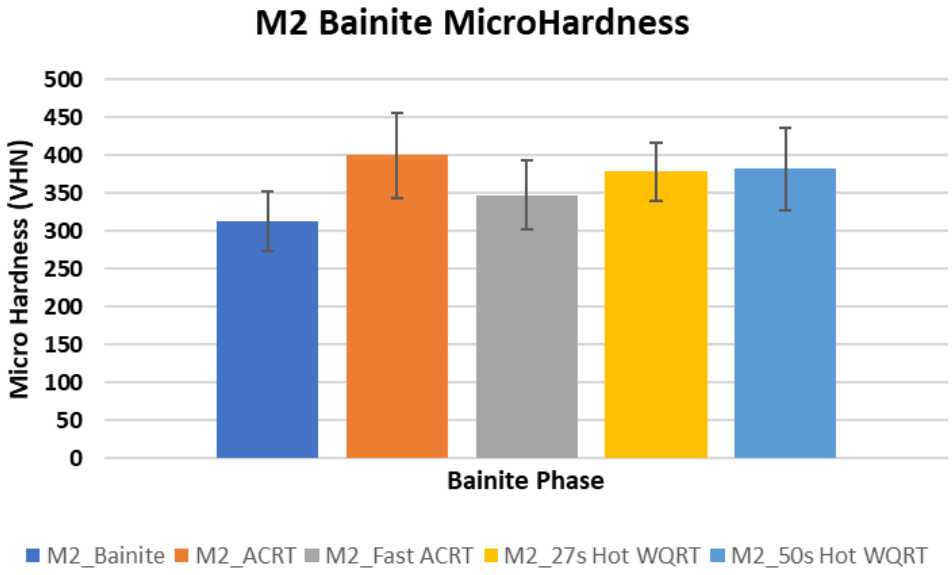

Figure 81: Steel M2 bainite microhardness values (VHN) at location 4 for ACRT (Left), fast ACRT (Second from left), bainite laboratory sample (Center), 27 seconds hot water quench (Second from right) and 50 seconds hot water quench (Right) forging conditions

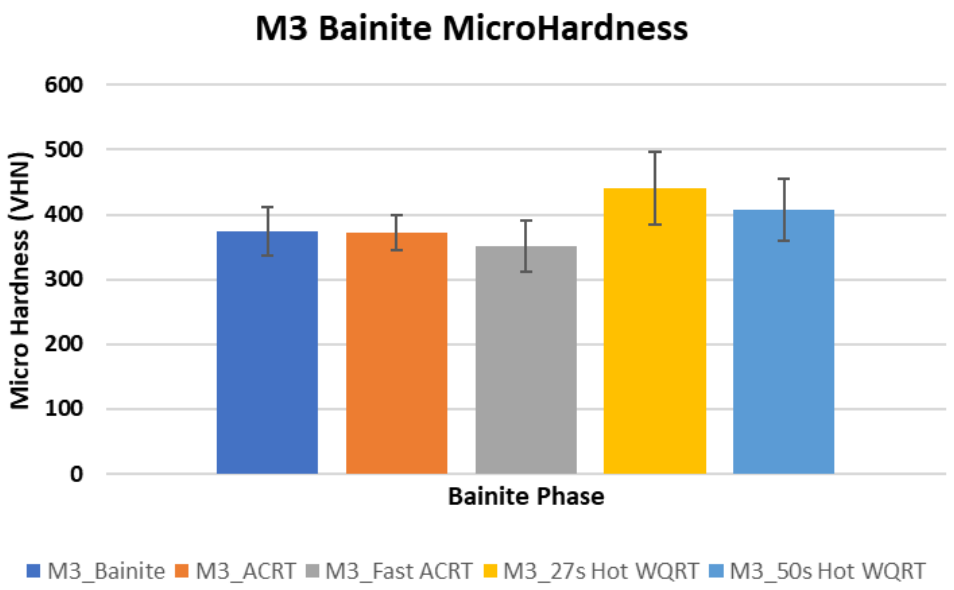

Figure 82: Steel M3 bainite microhardness values (VHN) at location 4 for ACRT (Left), fast ACRT (Second from left), bainite laboratory sample (Center), 27 seconds hot water quench (Second from right) and 50 seconds hot water quench (Right) forging conditions

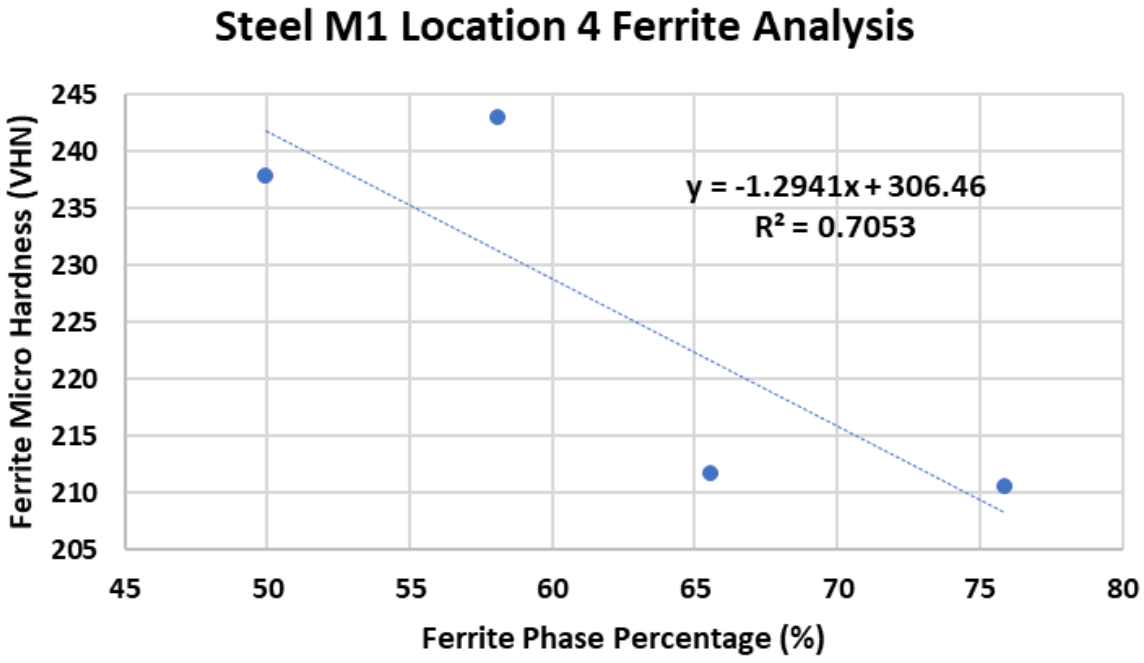

Figure 83: Steel M1 ferrite microhardness values (VHN) vs ferrite phase percentage (% area)

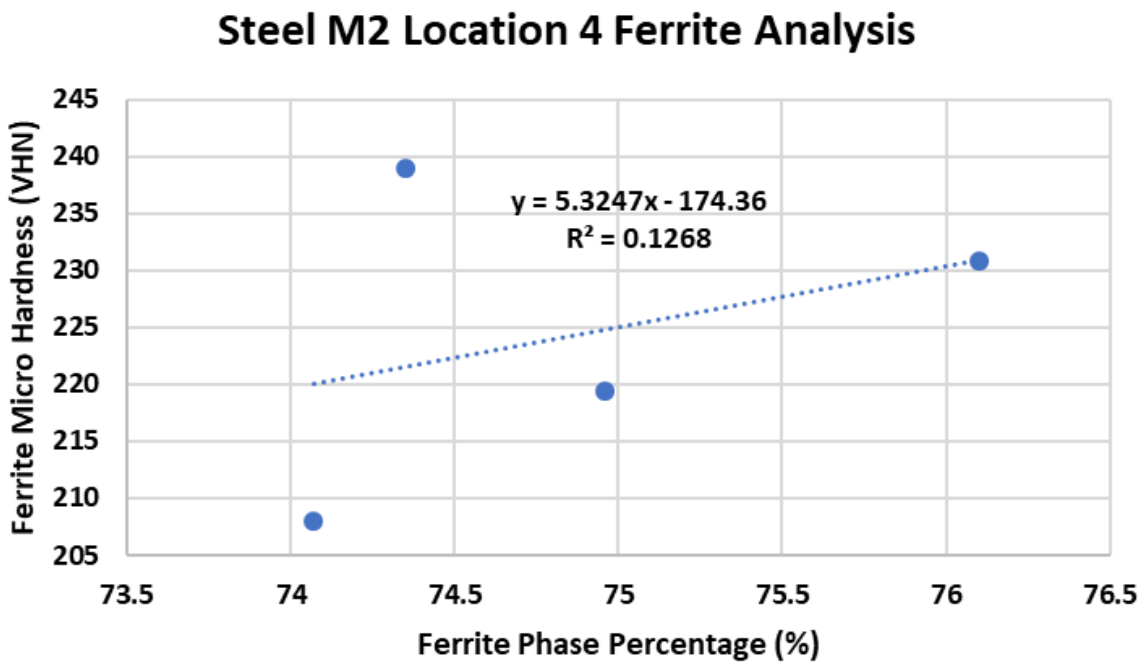

Figure 84: Steel M2 ferrite microhardness values (VHN) vs ferrite phase percentage (% area)

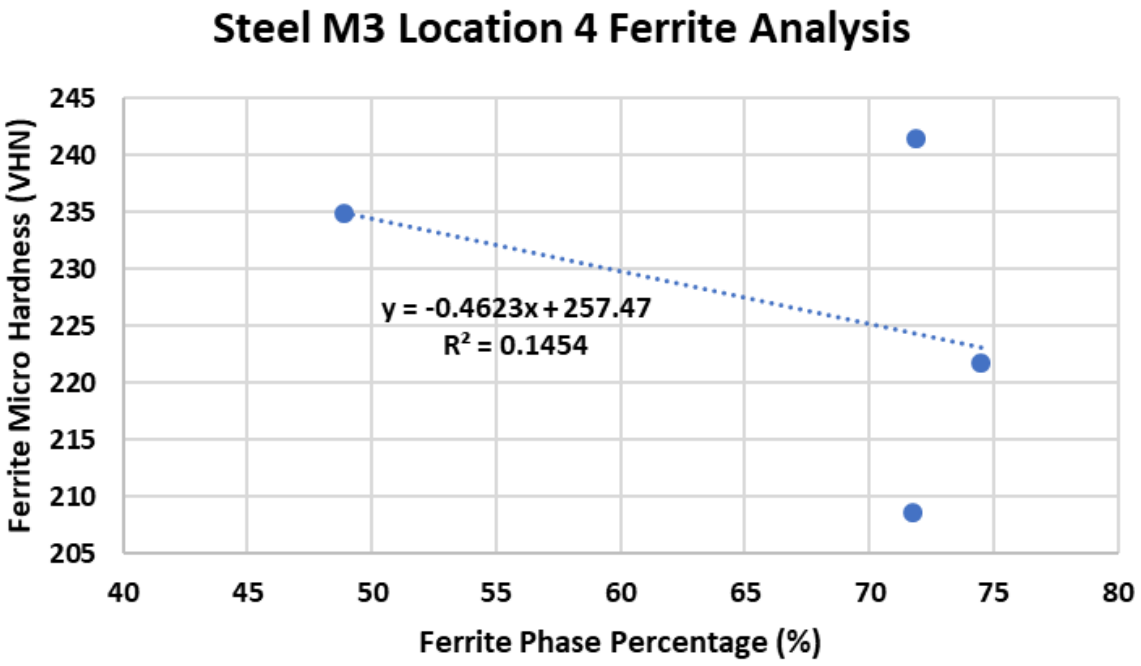

Figure 85: Steel M3 ferrite microhardness values (VHN) vs ferrite phase percentage (% area)

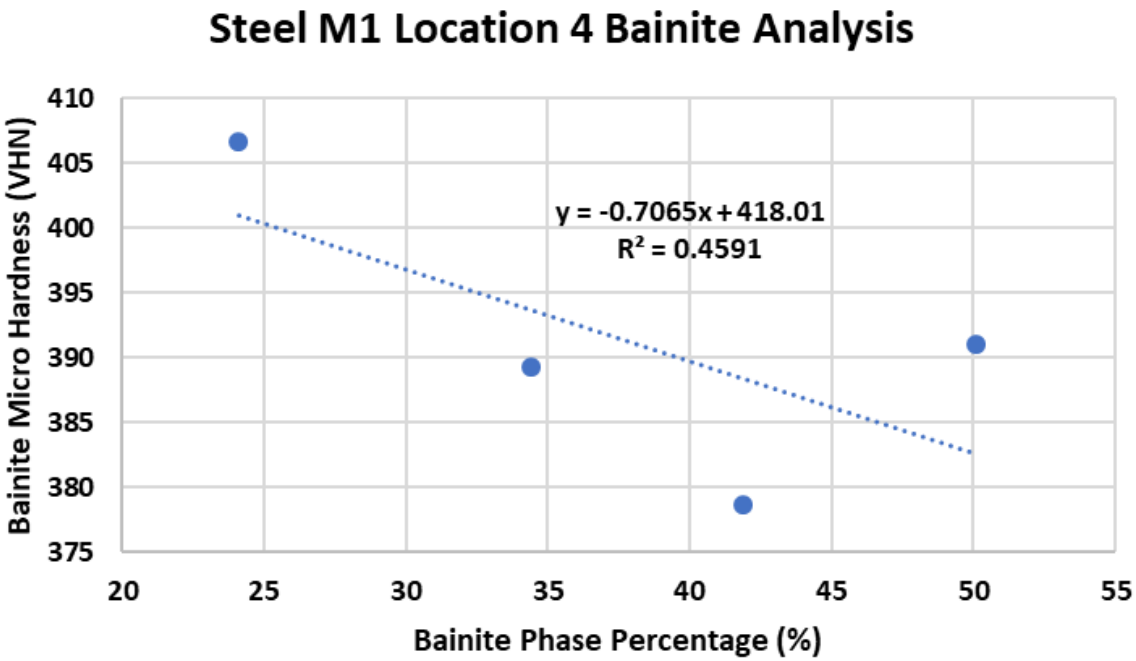

Figure 86: Steel M1 bainite microhardness values (VHN) vs bainite phase percentage (% area)

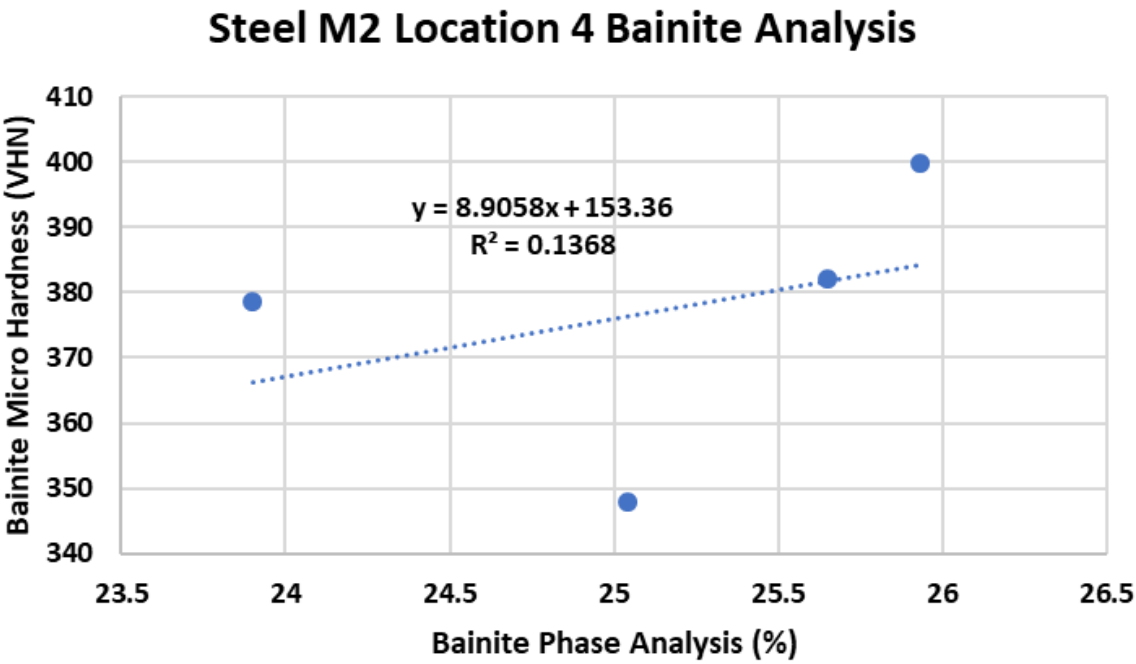

Figure 87: Steel M2 bainite microhardness values (VHN) vs bainite phase percentage (% area)

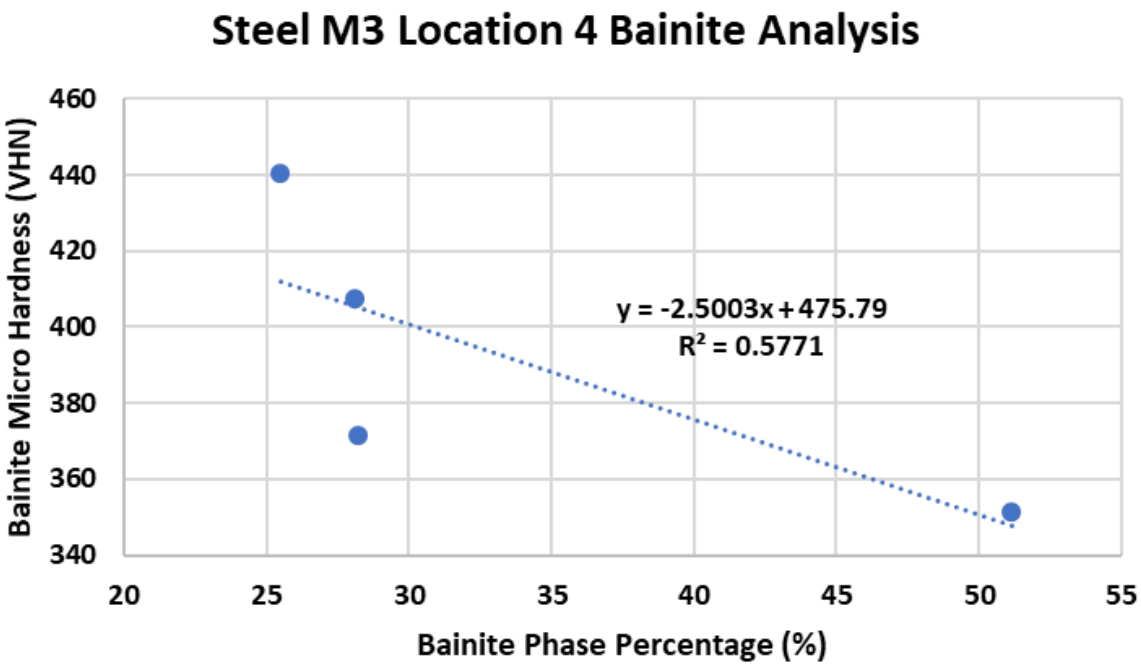

Figure 88: Steel M3 bainite microhardness values (VHN) vs bainite phase percentage (% area)

5.3.2 Precipitation Analysis

In order to investigate the precipitation behavior occurring in the steel, scanning electron microscopy (SEM) with external energy dispersive spectroscopy (EDS), as well as transmission electron microscopy (TEM) with selected area diffraction and dark field imaging were utilized for analysis.

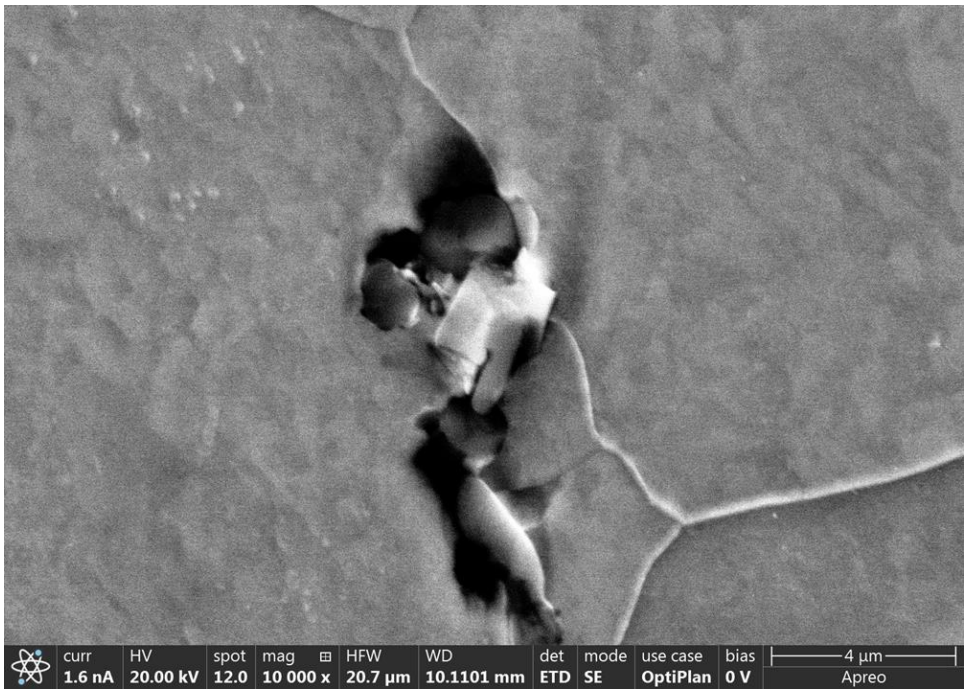

Figure 89: TiN and MnS precipitation in slow ACRT forging condition for steel M3

Figure 89 shows coarse titanium nitride and manganese sulfide precipitation in the slow ACRT forging condition for steel M3. The precipitates were identified using EDS technology, and elemental maps and point analysis data were generated.

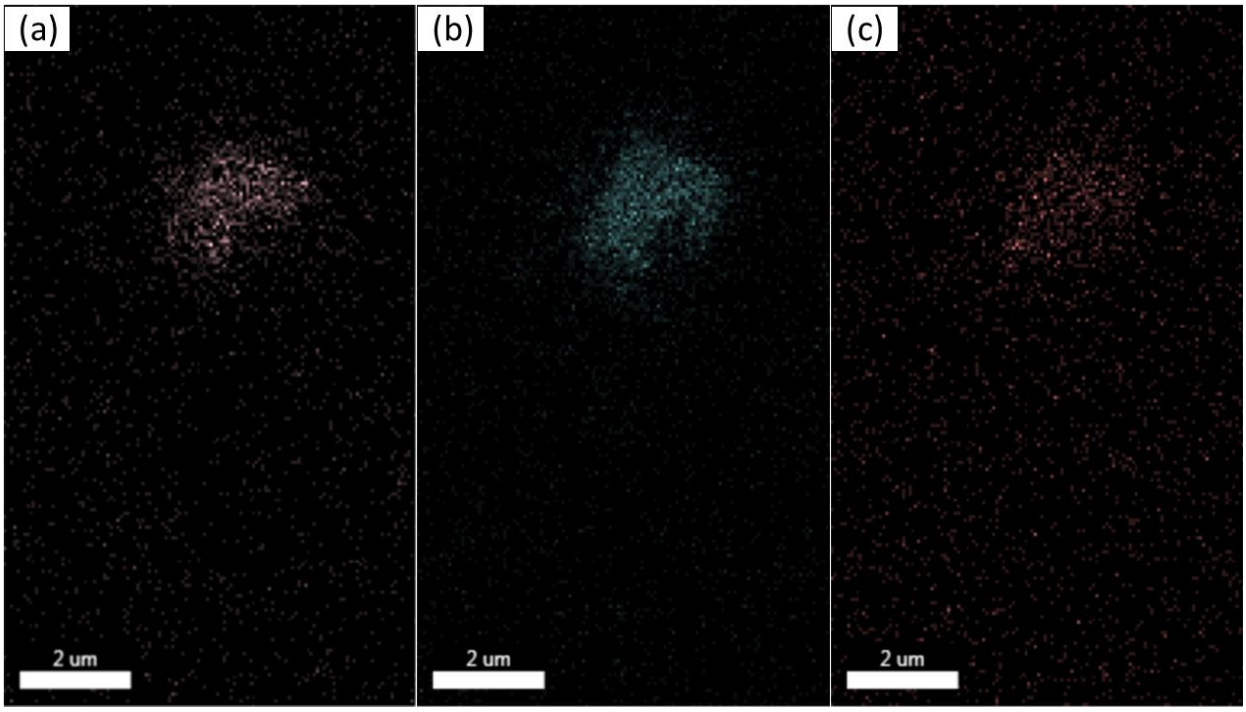

Figure 90: Nitrogen (a), Titanium (b) and Vanadium (c) EDS element maps for the SEM micrograph shown in Figure 89

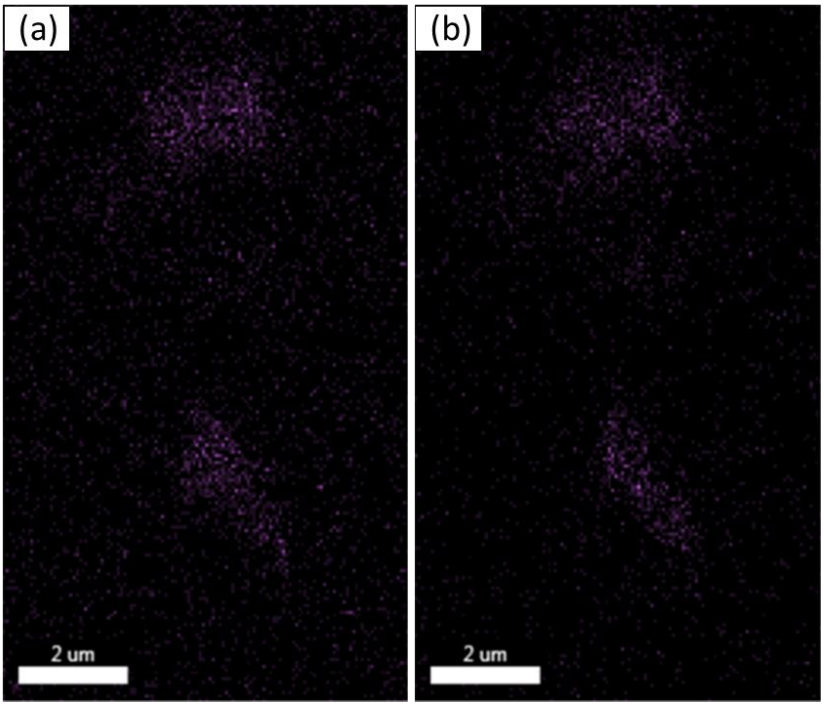

Figure 91: Manganese (a) and Sulfur (b) EDS element maps for the SEM micrograph shown in Figure 89

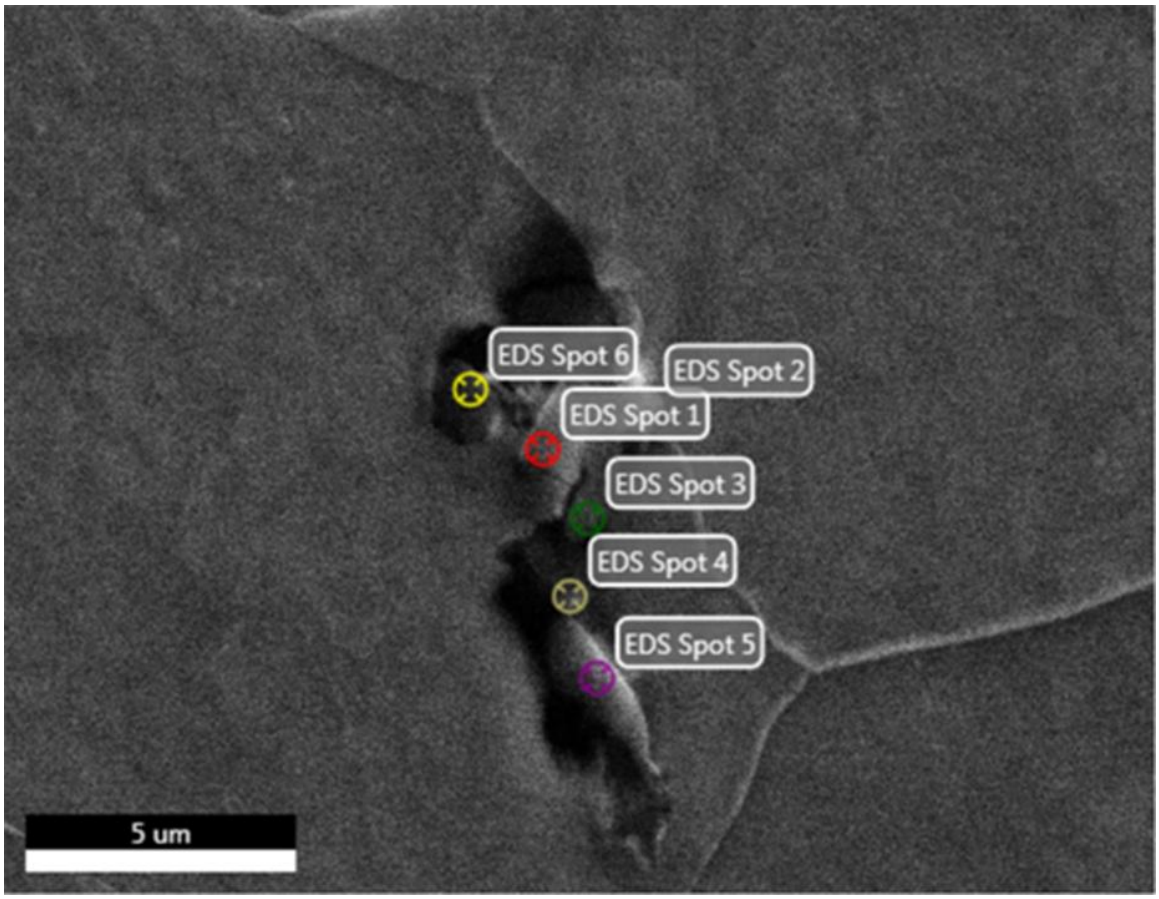

Figure 92: EDS point analysis locations from the SEM micrograph shown in Figure 89

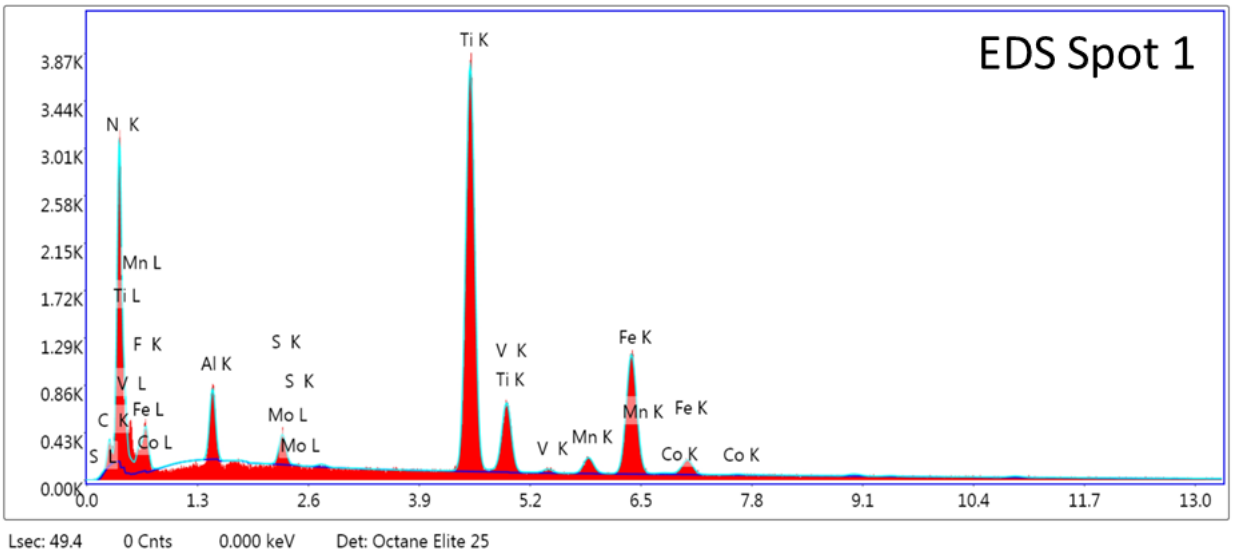

Figure 93: EDS point analysis of EDS spot 1 from Figure 92

Table 32: EDS point analysis of EDS spot 1 from Figure 92

Element	Weight %	Atomic %	Net Int.	Error %	Kratio	Z	A	F
C K	2.41	6.76	30.76	11.02	0.0132	1.1099	0.4911	1.0000
N K	14.84	35.63	302.70	5.81	0.0970	1.0881	0.6009	1.0000
F K	0.35	0.62	6.14	31.75	0.0010	0.9968	0.2996	1.0000
AlK	3.14	3.91	117.20	6.61	0.0208	0.9659	0.6842	1.0025
MoL	0.21	0.07	3.92	62.16	0.0016	0.7623	1.0250	1.0034
S K	1.48	1.55	54.66	7.39	0.0132	0.9754	0.9030	1.0111
TiK	45.71	32.10	980.10	1.93	0.4062	0.8678	1.0022	1.0217
V K	2.57	1.70	46.73	11.52	0.0225	0.8492	0.9988	1.0306
MnK	2.92	1.79	41.17	13.23	0.0246	0.8495	0.9673	1.0244
FeK	26.24	15.80	330.12	2.97	0.2235	0.8661	0.9766	1.0072
CoK	0.14	0.08	1.51	79.02	0.0012	0.8496	0.9793	1.0112

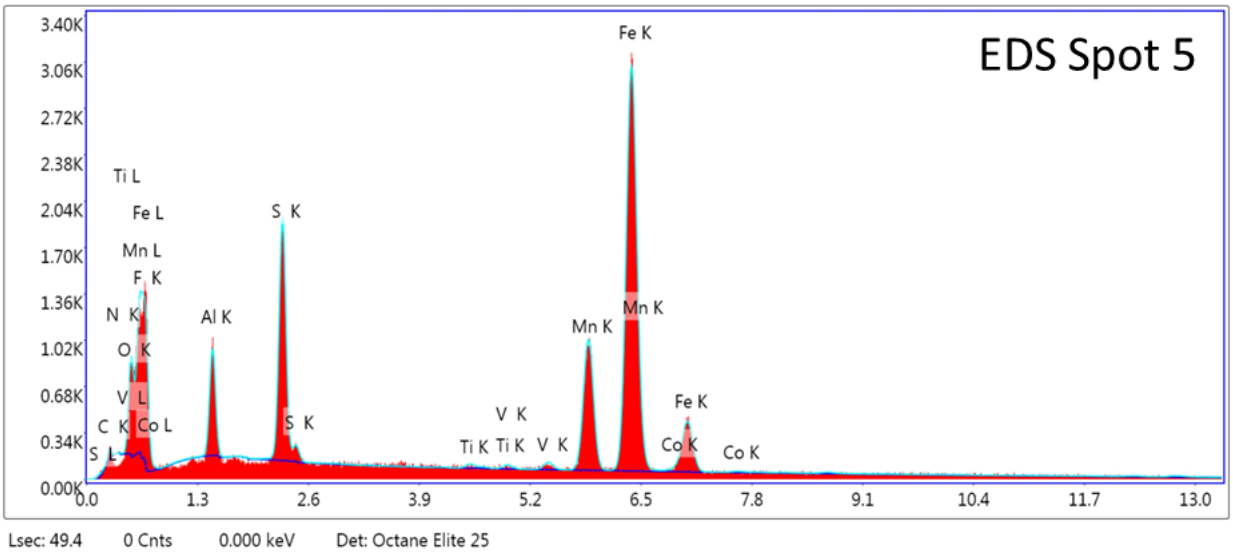

Figure 94: EDS point analysis of EDS spot 5 from Figure 92

Table 33: EDS point analysis of EDS spot 5 from Figure 92

Element	Weight %	Atomic %	Net Int.	Error %	Kratio	Z	A	F
C K	1.46	5.44	12.80	20.59	0.0051	1.1384	0.3102	1.0000
N K	0.00	0.00	0.02	99.99	0.0000	1.1153	0.4337	1.0000
O K	2.47	6.92	83.06	8.18	0.0164	1.0954	0.6056	1.0000
F K	0.77	1.82	24.49	16.24	0.0039	1.0210	0.4956	1.0000
AlK	3.91	6.49	141.73	6.89	0.0236	0.9889	0.6106	1.0019
S K	9.49	13.28	363.04	3.45	0.0822	0.9989	0.8604	1.0070
TiK	0.30	0.28	7.25	50.81	0.0028	0.8900	0.9864	1.0758
V K	0.36	0.31	7.55	24.35	0.0034	0.8712	0.9929	1.1048
MnK	17.20	14.04	281.13	3.18	0.1579	0.8724	0.9999	1.0525
FeK	63.68	51.14	893.41	2.01	0.5685	0.8901	1.0006	1.0024
CoK	0.37	0.28	4.44	69.30	0.0032	0.8738	0.9867	1.0050

As is seen in Figures 89-94, and in Tables 32 and 33, the precipitate at EDS spot 1 and 2 is a TiN precipitate, while the precipitate at EDS spot 5 is an MnS precipitate. Additional precipitation analysis can be seen in Figure 95, where further TiN and MnS precipitation can be observed. Figure 96 shows the EDS point analysis of the precipitation, where EDS spots 3 and 7 evidence TiN precipitation, and EDS spots 2,4,5,6 and 8 again evidence MnS precipitation. Of note in these figures is the size and shape of the TiN precipitation. Through the steel, TiN precipitates from 1 to 3μm in size are observed commonly, with fine (less than 1 μm in size) TiN, like that seen at EDS spot 7 in Figure 96, also observed (shown commonly through TEM). Additionally, the coarse TiN precipitates are not of the standard, cubic shape commonly found in TiN precipitation, as is seen at EDS spot 1 and 2 in Figure 92, and EDS spot 3 in Figure 96.

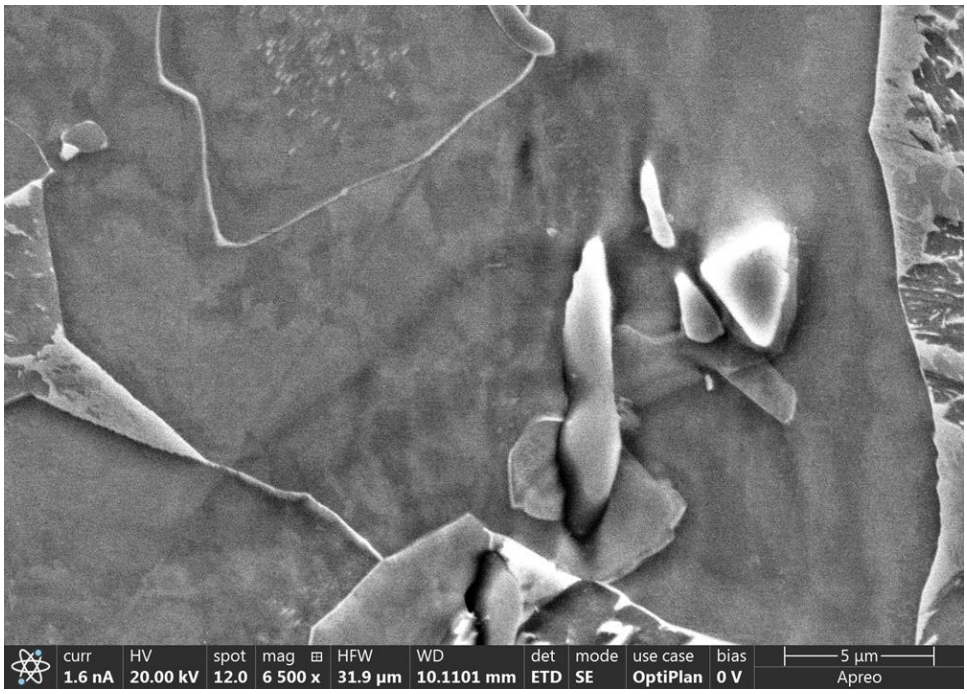

Figure 95: TiN and MnS precipitation in slow ACRT forging condition for steel M3

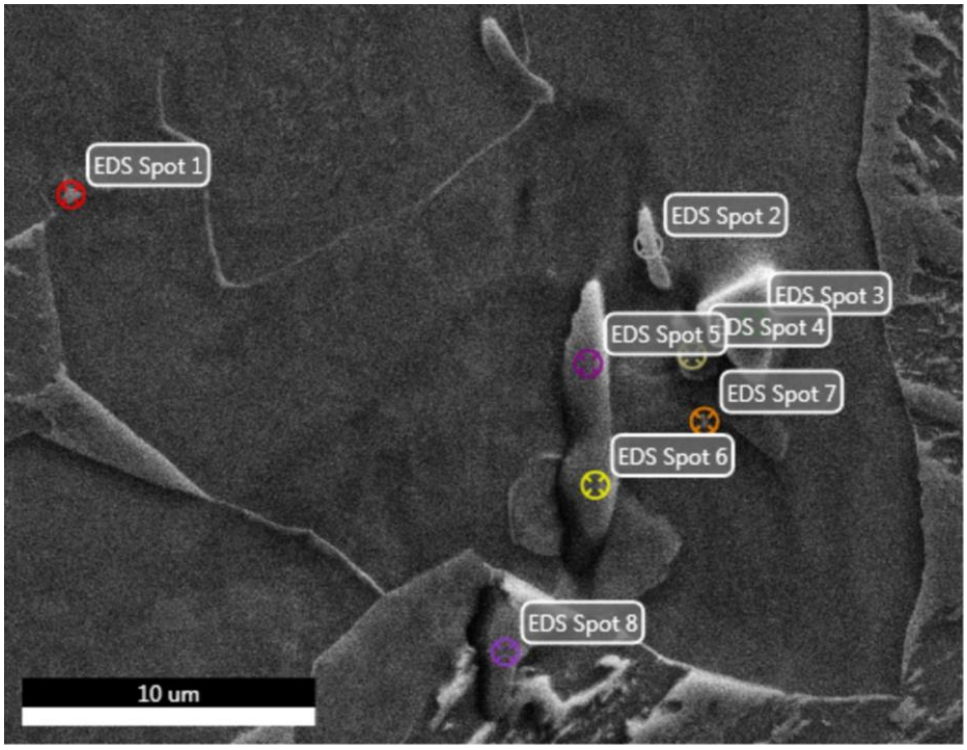

Figure 96: EDS point analysis locations from the SEM micrograph shown in Figure 95

Although some TiN and MnS precipitation was typically coarse enough to be observed using SEM techniques, TEM was necessary to observe the finer precipitates in the steel. To this extent, thin foil samples were prepared according to the procedure detailed in section 4.1.3. These precipitates were first imaged in a standard bright field image, following which, diffraction spot patterns and dark field images were generated at the same location. Figure 97 shows a V(CN) precipitate in the ferrite of the fast ACRT condition of steel M3. Figure 98 shows the spot diffraction produced from the location in Figure 97. Following indexing, the spot pattern most closely resembles a $[\bar{1}12]$ zone axis from a V(CN) precipitate, overlaid on the spot pattern for a $[\bar{1}33]$ zone axis from the ferrite host matrix.

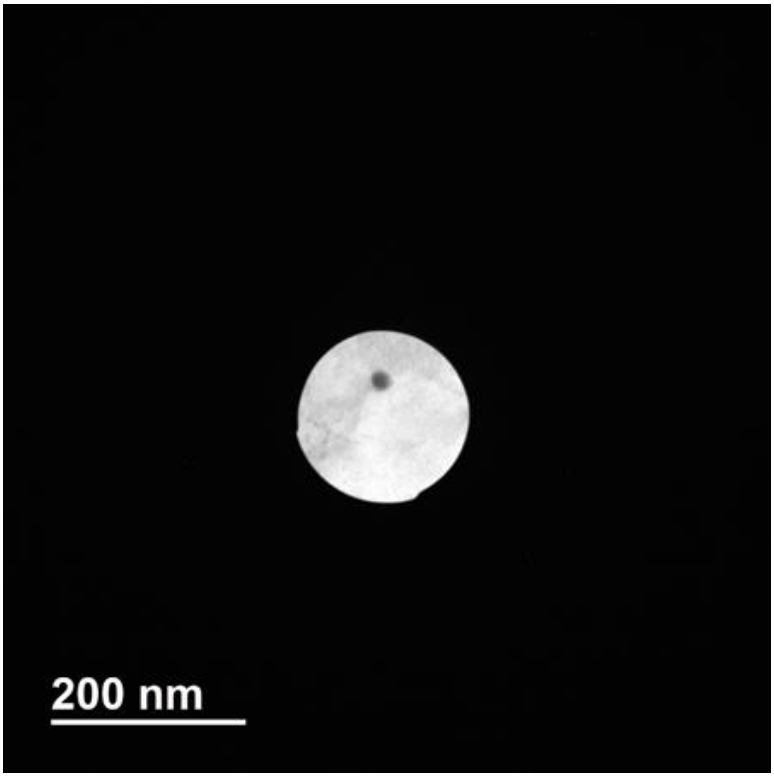

Figure 97: V(CN) precipitate in ferrite phase in TEM bright field selected area image for steel M3 fast ACRT condition

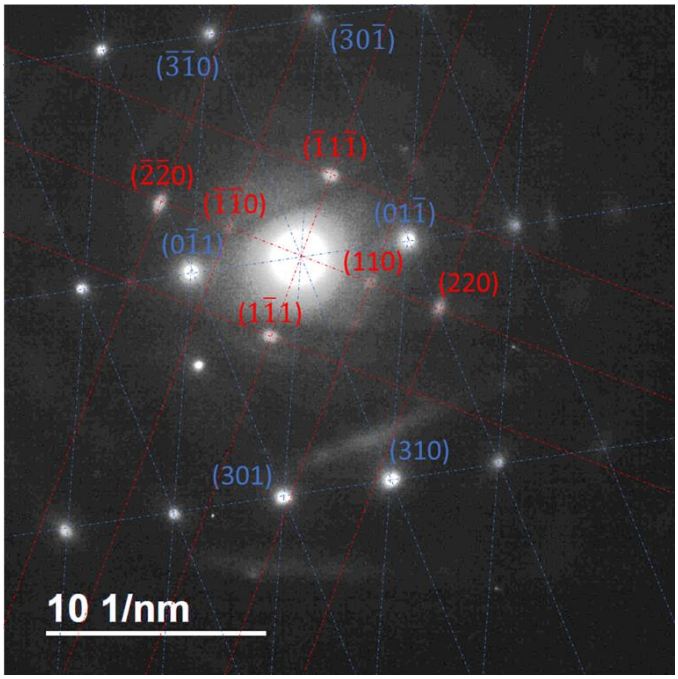

Figure 98: Diffraction spot pattern produced from V(CN) precipitate in Figure 97. Blue pattern shows diffractions from the [1$\bar{3}$3] zone axis in the ferrite matrix and the red pattern shows diffractions from the [1$\bar{1}$2] zone axis in V(CN) precipitate.

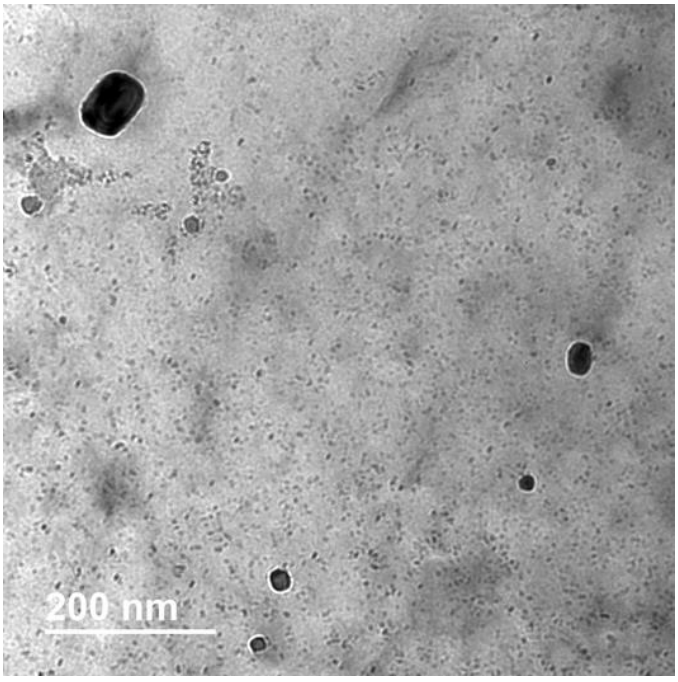

Figure 99: Fine VN precipitation in TEM bright field image for steel M3 fast ACRT condition

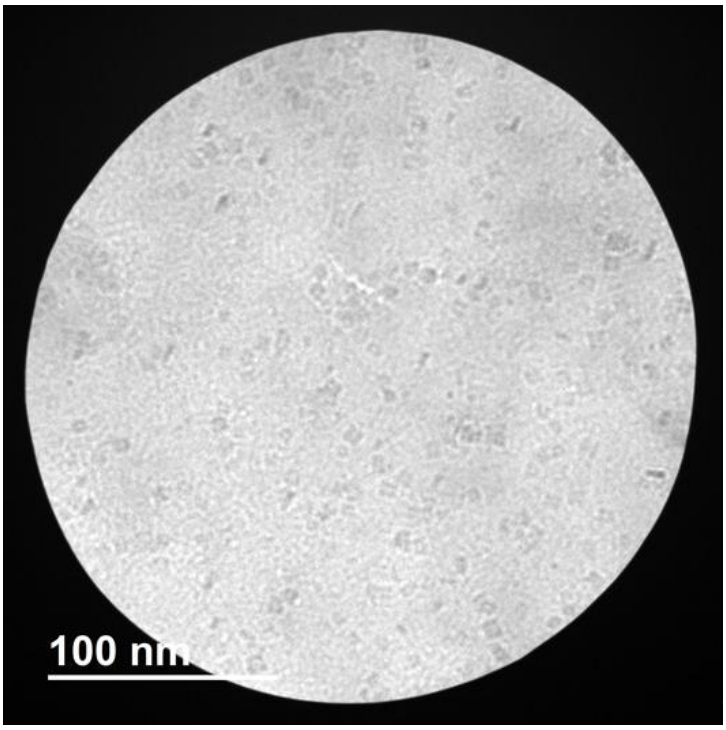

Figure 100: Fine VN precipitation selected area bright field TEM image for steel M3 fast ACRT condition

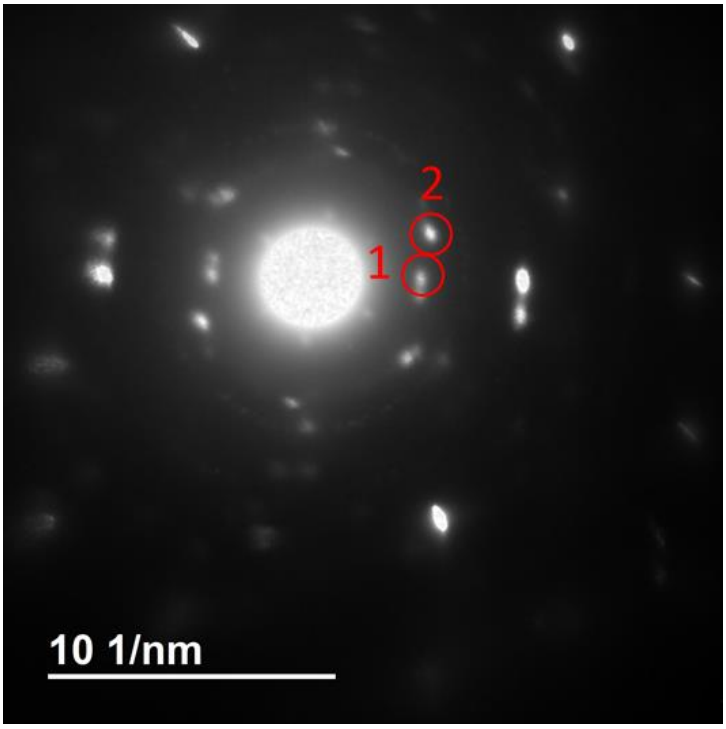

Figure 101: TEM diffraction spot pattern from Figure 100 with selected dark field imaging spots

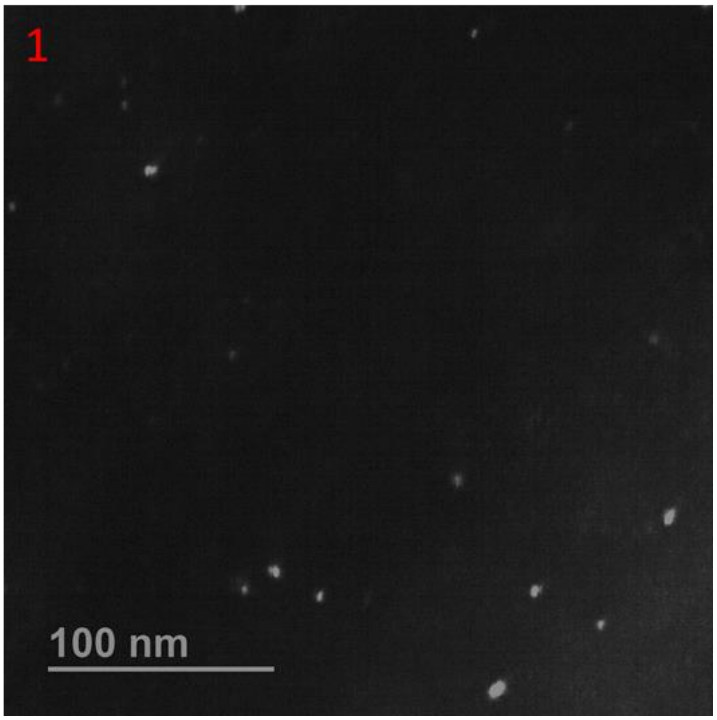

Figure 102: TEM center dark field image from diffraction spot 1 in Figure 101, showing VN precipitation

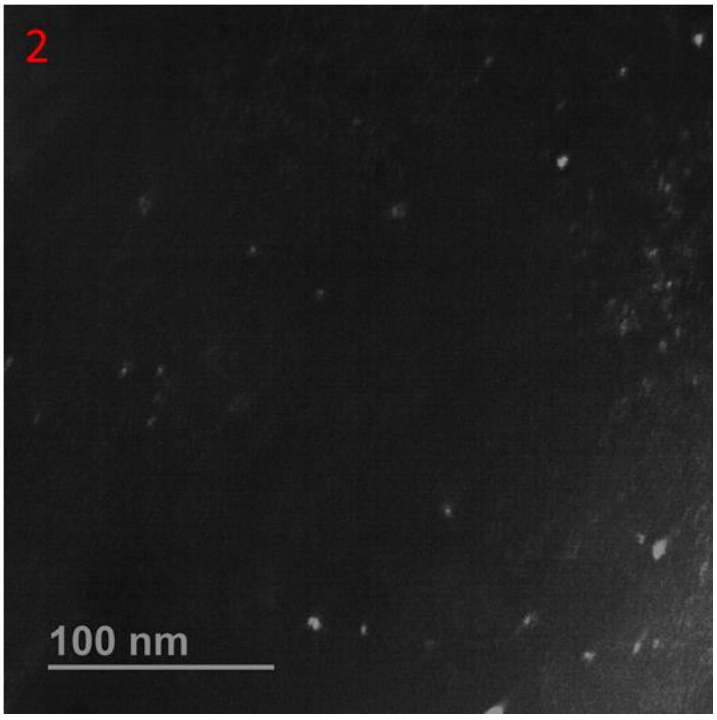

Figure 103: TEM center dark field image from diffraction spot 2 in Figure 101, showing VN precipitation

Figure 99 shows the fine V(CN) precipitation dispersion observed in the ferrite in steel M3 fast ACRT condition. Here can be observed larger precipitates, but also the very fine precipitation, present as the dark spots scattered throughout the image. A higher magnification, selected area bright field image of this location is seen in Figure 100. Here the fine precipitation dispersion is more readily observed. Figure 101 shows the diffraction spot pattern for this location, with center dark field imaged spots labeled 1 and 2. Additionally, the center dark field images for Figure 101 are shown in Figure 102 and 103. Here can be seen that a large amount of fine (<10nm) V(CN) precipitates are present in the steel.

In addition to the fine V(CN) precipitates observed, also seen in the steel are fine (50μm-200μm) TiN precipitates. Several of these precipitates, cuboidal in shape, are seen in Figures 104 and 105. Additionally, shown in Figure 106 is another TiN precipitate, for which indexed selected area diffraction images, as well as center dark field images are shown in Figures 107-110. Here, the precipitate appears to lie on a ferrite grain boundary, illustrated in Figure 110 by the precipitate residing on the edge of the illuminated ferrite region.

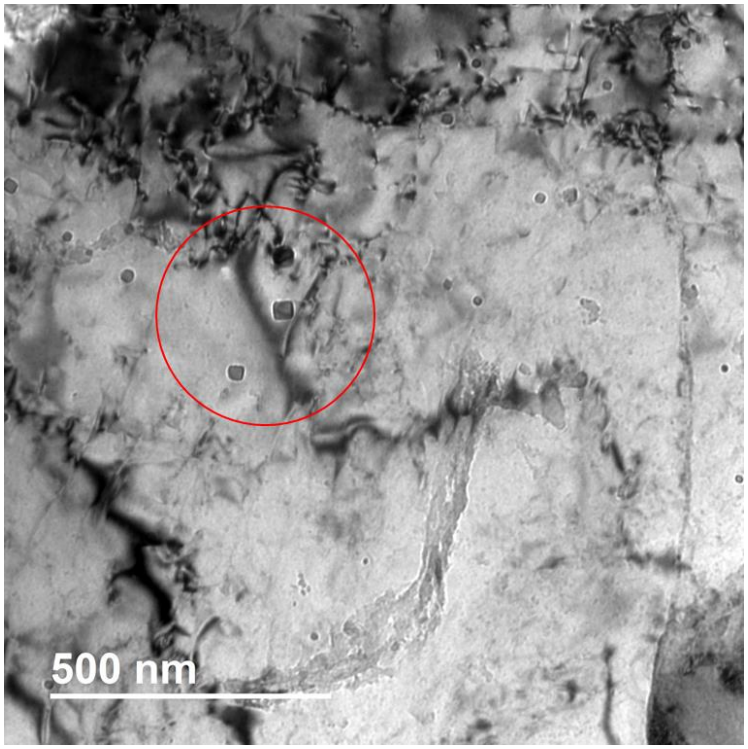

Figure 104: Titanium nitride precipitates from thin foil in steel M3 fast ACRT forging condition at location 4

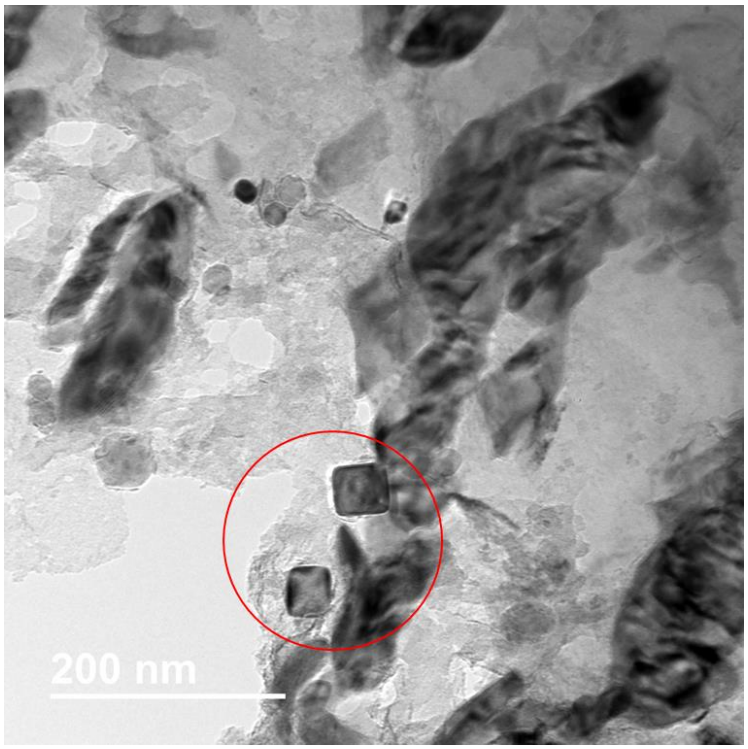

Figure 105: Titanium nitride precipitates from thin foil in steel M3 fast ACRT forging condition at location 4

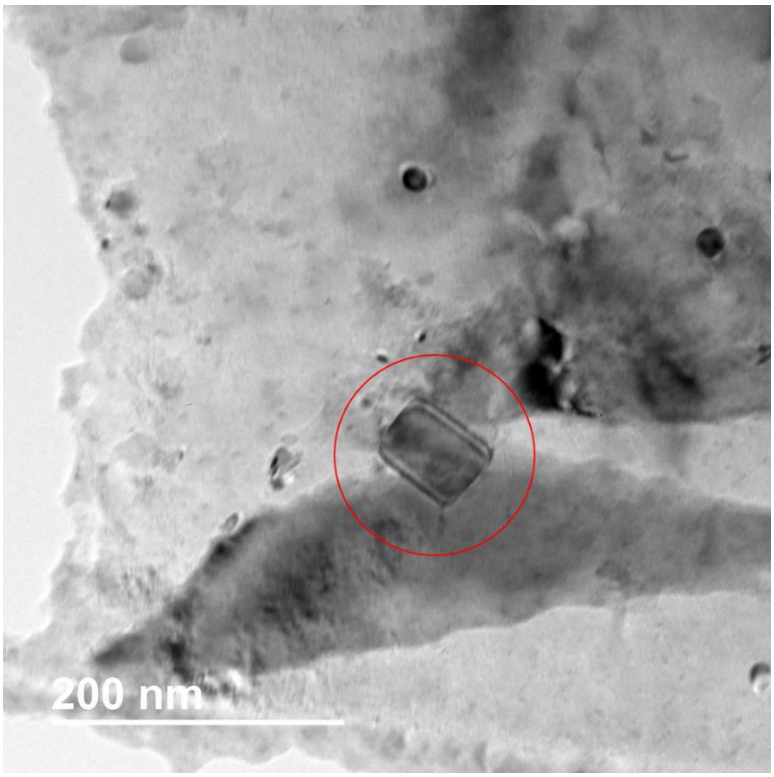

Figure 106: Titanium nitride precipitate from thin foil in steel M3 fast ACRT forging condition at location 4

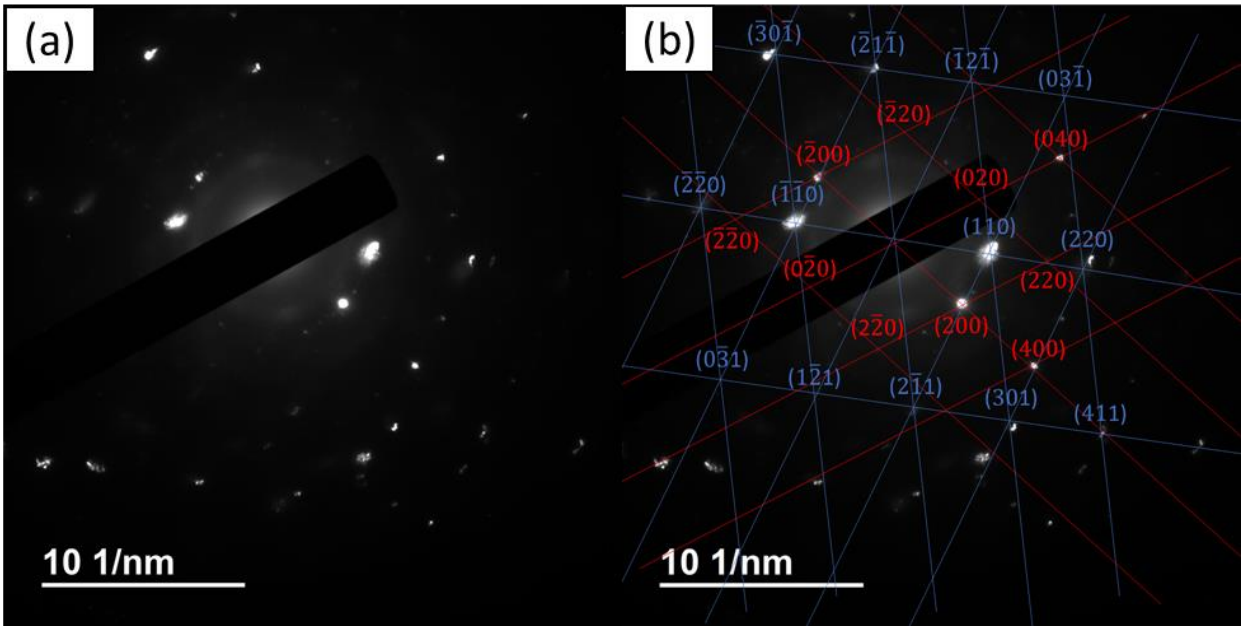

Figure 107: Long exposure with transmitted beam blocked diffraction pattern from TiN precipitate in Figure 101

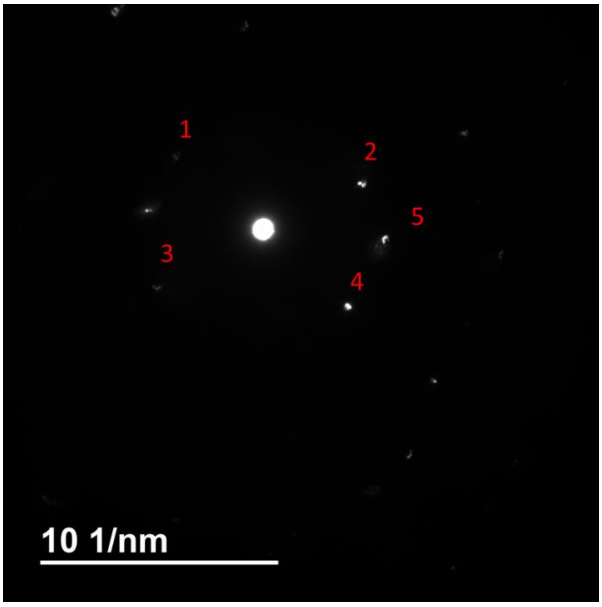

Figure 108: Short exposure diffraction pattern from TiN precipitate in Figure 88 with labeled center dark field image locations corresponding to the images seen in Figures 109 and 110

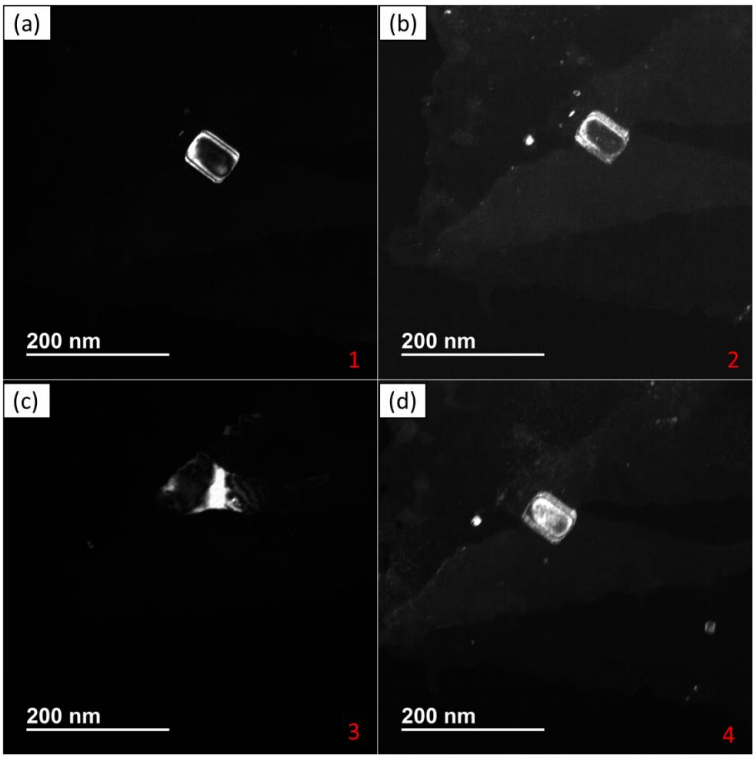

Figure 109: Center dark field image at TiN diffraction spots in Figure 108, taken at spots 1 (a), 2 (b), 3 (c) and 4 (d), illuminating TiN precipitate

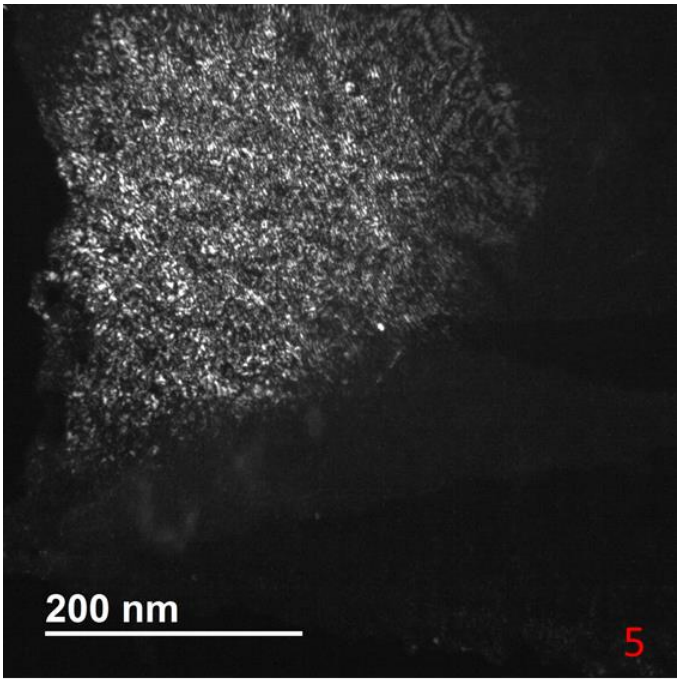

Figure 110: Center dark field image at ferrite matrix spot 5 in Figure 108, illuminating ferrite matrix

A synopsis of the observed precipitation behavior in the steel is shown in Table 34, where the type of precipitate, precipitate size and precipitate shape is listed. Here, the shape of the coarse TiN is described as "Quasi-Cuboidal" since the precipitates (shown in Figures 89 and 95) are not completely cuboidal, but show aspects of cuboidal geometries (straight edges, corners).

Table 34: Precipitation types, sizes and shapes observed in thin foil of steel M3 fast ACRT forging condition

Precipitate:	Precipitate Size:	Precipitate Shape
MnS	1µm-3µm	"Varies"
Coarse TiN	1µm-3µm	"Quasi-Cuboidal"
Fine TiN	<200nm	"Cuboidal"
V(CN)	<50nm	"Spherical"

6.0 Discussion

In the present study, the primary objectives were to both characterize the proposed steels M1, M2 and M3, as well as establish processing techniques suitable for production in an industry setting. Core to these objectives were the laboratory experiments conducted at BAMPRI facilities at the University of Pittsburgh. As explained in sections 2.3 through 2.5, optimal processing of these steels is dependent upon the identification of the quantities determined through the experiments. With this knowledge, processing schedules which successfully employ RCF techniques can be generated.

The first experiments, the grain coarsening experiments, detailed in sections 4.3.2 and 5.1.2, determined the T_{GC} (grain coarsening temperature) of each steel. As stated previously, this temperature denotes the temperature above which the microstructure undergoes abnormal grain growth.[17] In section 2.3.3, this process was explained as the growth of the structure's largest grains, at the expense of the smallest grains in the structure. The results of this process can be seen in Figure 51, image (f), where several grains in the right of the image have grown significantly and are surrounded by smaller grains. Image (g) in Figure 51 shows the results of heating of the structure above the grain coarsening temperature, resulting in a coarse, uniform austenite microstructure, in contrast to the heterogeneous microstructure in (f). In considering post cooling steel properties, the microstructure in (g), though less optimal than those in (a) – (e), is far less detrimental than the microstructure in (f), which produces heterogenous properties. Due to this, charts such as Figure 52 were generated, to easily identify the temperature where this heterogeneous transition occurs. Without abnormal grain growth, all grains in the steel should grow uniformly, meaning that the slope of the upper curve, which represents the average of all

grains larger than 2 standard deviations larger than the average of all grains measured, should stay consistent with the slope of the lower curve, which represents the average of all grains. Thus, the position at which the slopes of the curves differ denotes the T_{GC}. This method is of similar concept to the "2 curve" identification method used in Figure 31, where the appearance of the upper curve, representing the coarsened grains, identifies the T_{GC}.[17]

In analyzing the results of the grain coarsening experiments, contained in section 5.1.2, several things can be noted. First, steel 10V40, the standard steel, currently used at MFC, has a T_{GC} of 1100°C, while the reheating of the steel occurs at 1150°C. This means that the 10V40 standard steel is immediately incompatible with the RCF processing technique. Additionally, steels M1 and M2 have identical grain coarsening behaviors, implying that the reduction of Cr and Mo in steel M2 is not impactful in the grain coarsening. Steel M3, however, has a higher grain coarsening temperature than steel M1, indicating that the higher V content provides benefits for grain coarsening. As vanadium is in solution at these temperatures, per the solubility data provided in Figure 17 and Table 2,[39, 42, 43] this benefit is likely provided through additional solute drag effect of vanadium in solution, impeding the motion of the prior austenite grain boundaries which is necessary for grain coarsening.

The recrystallization forging experiments, detailed in sections 4.3.3 and 5.1.3, determined the T_{95} temperature for the steels. This temperature defines the temperature below which full recrystallization of the austenite no longer occurs, i.e. less than 95% recrystallization occurs. This temperature is critical for the project, as recrystallization of the deformed austenite grains is the primary method through which austenite grain refinement is achieved. A primary pitfall of this austenite grain refinement is the reduced hardenability which results from this. This is due to the increased nucleation rates of high temperature final phases during cooling, causing ferrite to form

more quickly, limiting the remaining austenite to form low temperature phases such as martensite. This phenomenon was part of the reason for the introduction of the hardenability increasing elements, predominantly Cr and Mo, to offset this possible negative impact. The hardenability impact of these elements, as well as Mn, is seen in Figure 23.[56] These elements help to impede the formation of the high temperature phases, increasing the possibility of obtaining low temperature final phases in accelerated cooling conditions.

The results of the recrystallization forging experiments, shown in section 5.1.3, bring several conclusions to the forefront. First, the low T_{95} values of 800°C – 850°C allow for flexibility in effective processing, with a 300°C or more range between the T_{RH} and the T_{95}. In an industrial setting, this temperature range is more than enough to reliably reproduce results. Second, the decreased T_{95} of 800°C for the M2 steel implies that Cr and Mo have appreciable impacts on the recrystallization behavior of the steels. Similarly, although steel M3 has double the V addition of steel M1, the T_{95} for the two steels is equivalent. Thus, it is implied that V, at the levels studied in the project, is not impactful in terms of the recrystallization behavior of the steels. Finally, analyzing the grain structure of the steels at 900°C shows fine grain sizes, approximately 10 μm equivalent grain diameter, providing a successful starting condition for steel cooling. This result is similar to the results observed in Figure 13,[17] where prior austenite grain sizes between 10μm-20μm are obtained immediately anteceding deformation.

The final laboratory experiments, the cooling trials, detailed in sections 4.4 and 5.1.4, as stated, were designed to produce final microstructures consisting of ferrite/pearlite, ferrite/bainite and ferrite/martensite. For this purpose, JMATPro simulation software was used to generate CCT curves, and from the results of these curves, cooling paths which would be achievable in an industry setting were selected for production of each phase. An air cooling to room temperature

cooling path was selected to produce a ferrite/pearlite microstructure, while a water quenching to room temperature was selected to produce a martensite microstructure. However, through SEM analysis of the ACRT sample, pearlite was not found significantly in the final microstructure, as indicated in Figure 111. These samples are the slowest cooled samples in the experiment, and as such the steels are not expected to form pearlite at the cooling rates used in this study.

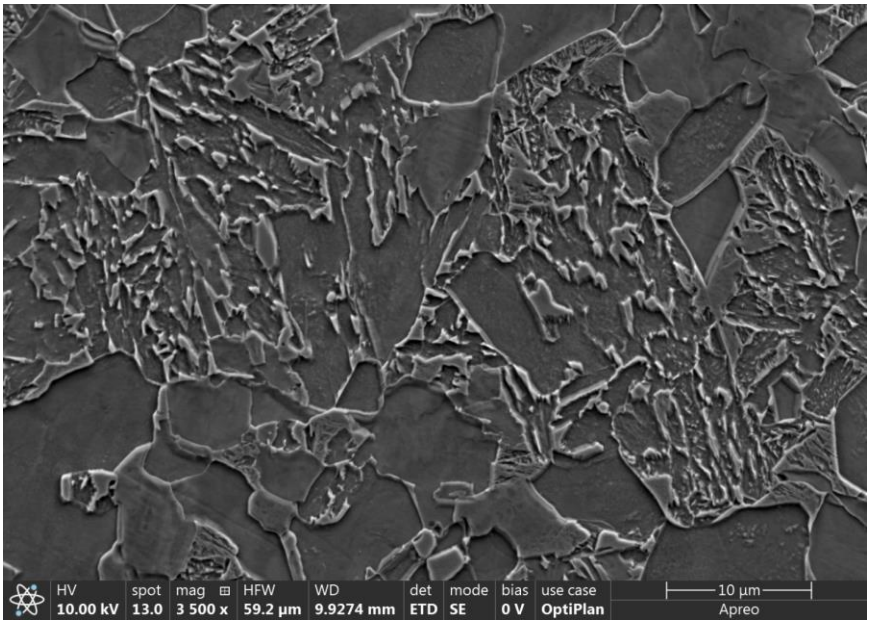

Figure 111: Steel M3 slow ACRT microstructure under SEM at 3500X, showing lack of pearlite in slowest cooled samples

While the microstructures comprising predominantly of ferrite and martensite were relatively simple to achieve, and can be easily implemented in an industrial setting, the production of a bainite microstructure is more difficult. A sample bainite cooling schedule from the literature is seen in Figure 41,[18] which shows an accelerated cooling schedule to 400°C, where an ACRT cooling path is then applied. This accelerated cooling rate was unattainable for the geometries studied in this project with the given equipment. In the laboratory, an accelerated cooling rate of

approximately 30°C/s was accomplished using forced helium convection cooling to 500°C, and the samples were then held at 500°C for 110 seconds, long enough for the predicted completion of the austenite to bainite transformation. Due to the scarcity of helium, this process is not economical on an industrial scale, and thus, more acceptable accelerated cooling methods were needed. This was the reason for the hot water quench trials later in the project, which were hypothesized to provide adequate cooling rates, yet allow for enough control to be reliably reproduced and maintain low environmental and economic impacts in production.

The results of the cooling trials, shown in section 5.1.4, made clear several conclusions. First, steels M1 and M3 both show a marked increase in hardness when the cooling path is accelerated from the ACRT (air cool to room temperature) to the helium cooling. This implies that the microstructure consists of harder phases, namely bainite, when subjected to the helium cooling. The analyzed optical micrographs of these conditions confirm this, as the blue regions revealed by the LaPera etch process indicate bainite phases. Additionally, steel M2 did not respond similarly to this cooling schedule, implying that the reduction in the hardenability elements Cr and Mo present in M2 has negative impacts when attempting to achieve harder microstructure phases. When comparing steels M1 and M3 in the slow ACRT and bainite conditions, M3 was found to be harder in both conditions. As M3 differs only in its doubled V content, it is likely that its precipitation behavior of V solute hardening is providing strengthening of the ferrite present in both the polygonal ferrite and bainite phases, as this is often a reason that V is implemented in steel design. However, this same behavior is not noted when analyzing the martensite samples. In fact, M1, M2 and M3 all have roughly equivalent martensite hardness levels, implying that the present differences in V, Cr and Mo have little to no effect for samples of the tested geometry. This is expected as V is implemented for its benefits in the polygonal ferrite phases, where VN

precipitation is plentiful,[68] and not for low temperature phase benefits, while Cr and Mo primarily allow for low temperature phase acquisition. The results of these experiments indicated that steel M1 and M3 would likely be the more successful steels for the acquisition of a bainite microstructure in the final forging samples.

The initial full forging trials, detailed in sections 4.5.2 and 5.2.1, were designed to investigate the response of the steel to several simple processing schedules, including the current, 10V40 processing schedule in use at MFC. Here, the standard cooling schedule, an ACRT cooling, provided the low strength, high toughness ferrite/bainite microstructure. A second cooling path which used a fan cooling schedule used by MFC, was expected to provide a moderately higher strength ferrite/bainite sample. Finally, a cold WQRT cooling path produced a majority martensite/bainite microstructure, for the purpose of property determination in the martensite forging condition. All full forging samples were compared to the standard 10V40 wheel hub used by MFC, to provide a baseline value, and to be able to provide recommendations for process changes to MFC correspondents.

A final note for the initial full forging samples concerns the locations for metallographic analysis throughout the sample. As is seen in Figure 45, 5 locations were selected for measurement for various reasons. Location 1, in the center of the “Flange”, is one of the fastest cooling locations in the forging, and thus should have the highest hardness, and lowest toughness. For this reason, it was also selected as the location of the Charpy samples, as it not only provided the minimum toughness in the sample, but also provided a convenient location for Charpy machining. Location 2, taken within 1mm of the surface of the fillet, was selected as a location of critical geometry, where higher stress concentrations are present, and where MFC had noted the most failures throughout the lifetime of the product. This location has a slower cooling rate than location 1, but

much faster than the column. Location 3, taken at the center of the column, was selected as the location of slowest cooling rate within the forging, thus providing a minimum measurement of the hardness of the steel. Location 4, taken at the half radius in the column, was selected as a location near the gauge length of the tensile sample. Additionally, this location is approximately the deepest location in the steel which is not machined out for the final product, representing the slowest cooling rate in the final product. Finally, location 5, taken from the center of the "Lip", has a moderately fast cooling rate, and is the location of a stamping procedure which MFC customers perform.

In analysis of the initial full forging samples, the results of which are detailed in section 5.2.1, several important trends were observed. First, the ACRT samples for the steels can be seen to be comprised of mixtures of predominantly ferrite and bainite for each steel. Here, the percentage of polygonal ferrite in the steel trends to decrease with increasing cooling rate. In the slow and fast ACRT conditions, the non-polygonal ferrite phase is comprised of bainitic ferrite as well as upper bainite. This trend, which is quite significant for steels M1 and M3, is largely absent when analyzing steel M2, demonstrating the impact of steel M2's lack of hardenability. This displays the impact of Cr and Mo additions, through the lack of ferrite formation suppression provided by Cr and Mo in the steel. The microstructures present in the cold WQRT forgings are comprised of a mixture of martensite and phases resembling lower bainite morphologies. Here, the insufficient hardenability in steels M1, M2 and M3 is evident in the inability to form predominantly martensitic microstructures throughout the forging. This observation fits expectations, as the ideal diameter values of steels M1, M2 and M3 are 3.86mm, 2.18mm and 4.19mm, respectively, while the thickest portions of the forging exceed this value, with the column of the forging having an approximately 5.72mm diameter.

The mechanical properties of the initial full forgings show that all three experimental steels M1, M2 and M3 have lower strengths, but higher toughness values than the standard 10V40 ACRT forging. Specifically, in each condition, (slow ACRT, fast ACRT and WQRT) steel M3 has the highest strength, and steel M2 has the lowest strength. In the slow and fast ACRT conditions, the differences in the strengths of the steels are explained clearly through the composition differences. Steel M3, the strongest steel, has increased vanadium over steel M1, the intermediate strength steel. Here, vanadium is included in the steel for precipitation strengthening of the ferrite, as is observed in section 5.3.2 as well as in the literature.[68] This is evidenced in the increased strength of the M3 ACRT conditions over the equivalent M1 conditions. Steel M2, the lowest strength steel, has decreased Cr and Mo when compared to steel M1 and M3, and less V than steel M3. Here again can be seen that the individual phases of steel M2 are typically less hard than the corresponding phases of steel M3, but of additional interest are the impact of the decreased Cr and Mo in the steel. Cr and Mo, again, are alloying elements, added to increase the hardenability of the steel, through the suppression of formation of ferrite. This effect can be seen in analysis of the phase balance in the ACRT conditions of the steels, where steel M2 forms higher percentages of polygonal ferrite than the same conditions for steels M1 and M3. As polygonal ferrite has lower strength and hardness than the phases which form at lower temperatures (bainite and martensite), this, in addition to the effects of the decreased vanadium, account for the lower strength and hardness of steel M2 in the ACRT condition.

The analysis of the WQRT condition is consistent with that of the ACRT conditions, with an added element. The WQRT cooling rates are fast enough to form martensite, but not fast enough to avoid formation of higher temperature phases completely, primarily bainite. In martensite, vanadium precipitation is not a consideration, as this effect is only present in the high temperature

phases, i.e. ferrite. In these forgings, vanadium precipitation strengthening occurs in the ferrite that is present, but the predominant strengthening derives from the Cr and Mo alloying differences. As stated before, Cr and Mo suppress the formation of high temperature phases, and thus, higher levels of these elements allow for increased martensite formation in the steel. This can be seen in the D_I calculations of the steels, where steel M2 has nearly half the hardenability of steels M1 and M3.

The full forging hot water quench trials, detailed in section 5.2.2, employed the cooling methods determined in the submersive interrupted quench trials, detailed in section 5.1.5. In comparing these forgings to the initial full forgings, the first trend of note is that the strength values of the hot water quench forgings are lower than the strengths of the fast ACRT forgings, and higher than the slow ACRT forgings strength values. Conversely, the toughness of the hot water quenching forgings tends to exceed that of the fast ACRT forgings. While these steels have differences in phase composition (shown in Table 31), the strength differences between the fast ACRT forgings and the hot water quench forgings is best explained through the micro hardness value differences between the cooling conditions. These differences are displayed graphically in Figures 77 through 88. In the faster cooled, hot water quenched forgings, and the fast ACRT forging, the micro hardness of the polygonal ferrite for steels tends to be slightly higher than the microhardness of the polygonal ferrite in the slow ACRT condition. This hardness difference can be explained through differences in vanadium precipitation behavior. As vanadium predominantly precipitates in ferrite in the high temperature region (480°C – 815°C), the steel conditions which cool optimally through this region take further advantage of vanadium precipitation strengthening. As is seen in Figure 112, faster cooling rates allow for finer dispersion of VN precipitates in ferrite, in a similar steel composition to the 10V40 steel in this project.[68] A finer dispersion of precipitates allows for higher strengthening over a coarser distribution of precipitates of the same total volume

fraction. An additional trend which can be initially be noted in these steels is the apparent insignificance of the micro hardness of the bainite phases in impacting the bulk strength and hardness of the forgings. Although the hot water quench steels have higher micro hardness values in the bainite, this trend is not seen, and often contradicted, in the trends of the bulk hardness and tensile strength.

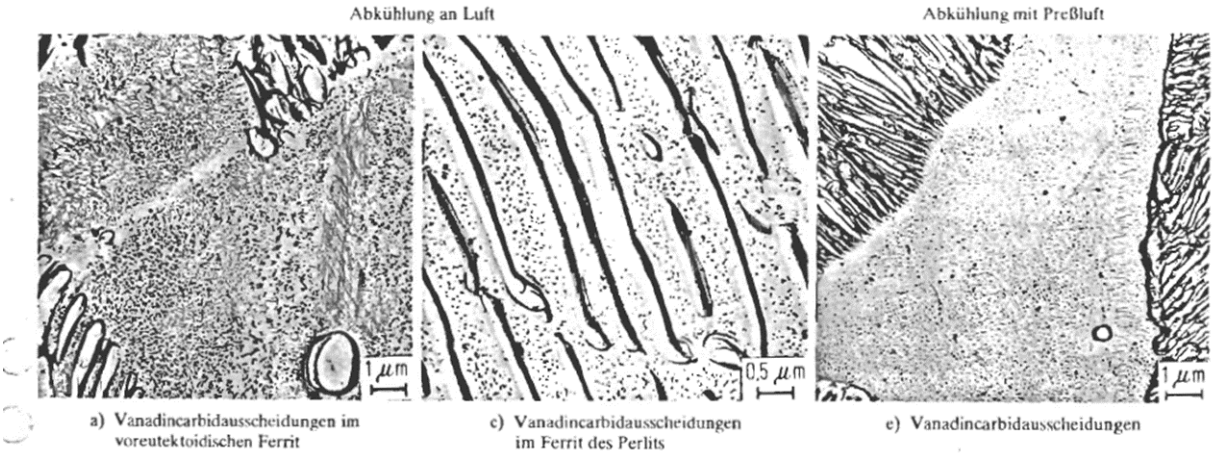

Figure 112: VN precipitation in ferrite in a CK 45 steel + 0.10%V in air-cooled conditions (a) and (c), and fast air-cooled condition (e), demonstrating precipitation refinement with cooling rate increases[68]

In further analyzing the full forging hot water quench trials, additional trends can be seen. For steels M1 and M3, as the quenching time increases from 27 seconds to 50 seconds, the microhardness of the polygonal ferrite increases notably (Figures 77 and 79), as well as the bulk hardness and strength of the forging. In contrast to this, as the quenching time increases from 27 seconds to 50 seconds, the microhardness of the bainite decreases. These trends can be reasonably explained when the phase percentages of the respective phases are also considered. As can be seen in Figures 83-88, the micro hardness values of each of the phases is influenced by the percentage of the microstructure which that phase comprises, aside from in steel M2 (Figures 84 and 87)

which does not vary significantly in phase percentage. Thus, as the amount of ferrite or bainite increases, the microhardness of that individual phase decreases. This phenomenon arises due to the limited amounts of carbon and vanadium in the steel, which harden and provide strength to the bainite and ferrite phase in the steels, respectively. As the volume fraction of bainite increases in the steel, the carbon per unit volume of bainite necessarily decreases. This specific phenomenon can be seen in Figures 70 and 71, which display the bainite phase in an SEM image for the M3 fast ACRT and M3 27 seconds hot water quench conditions, respectively. These forgings differ significantly in bainite phase percentage, with the fast ACRT condition comprising 51% bainite, and the 27 second hot water quench condition comprising 28% bainite. The microhardness of the 27 second hot water quench condition is significantly higher than the fast ACRT condition and is clearly seen in the differences in the morphology of the bainite in the two figures. While the 27 second hot water quench condition has a fine, upper bainite microstructure in the non-polygonal ferrite phase with large amounts of fine, dispersed cementite, the fast ACRT condition resembles a more bainitic ferrite microstructure in the non-polygonal ferrite phase, with large region of ferrite and cementite in the phase. Although the hardness of the bainite phase may be lower in the fast ACRT condition, the much higher phase percentage of the bainite, as well as the higher microhardness of the remaining polygonal ferrite phase contributes to the higher bulk strength and hardness in the fast ACRT condition forging. These results are consistent when considering the knowledge that bainite and martensite microstructures increase in strength and hardness with increases in carbon content in the phase.

As is seen in the results, the accelerated cooling conditions of the steels in the full forging geometry did not achieve the high phase percentages of bainite and martensite which were expected. Two primary factors are believed to have influenced this effect. First, the compositions

of the steels were decided with calculations of the hardenability having assumed a prior austenite grain size of ASTM 7, or approximately 30μm grain diameter. The grain refinement that was observed in the project exceeded the expectations, providing prior austenite grain sizes approaching ASTM 10, or approximately 10μm grain diameter. These decrease the hardenability of the steels, through the increased quantity of nucleation sites present in the refined microstructure for the high temperature phases. This effect can be seen in Figures 113 and 114, where the CCT diagrams for a 30μm average equivalent prior austenite grain diameter and a 10μm average equivalent prior austenite grain diameter, respectively, are shown. Here, the smaller prior austenite grain diameter causes a slight left shift in the phase curves, implying formation of high temperature phases at faster cooling rates. The second factor is the geometry of the part which was used. In partnering with MFC, who's assistance was indispensable in completing the project, who produces large section automotive forgings, the decreased hardenability of the steels was further exploited. The steels would likely have been more successful on smaller section forgings, where the decreased hardenability would not have been as great a factor in attaining low temperature phases throughout the geometry.

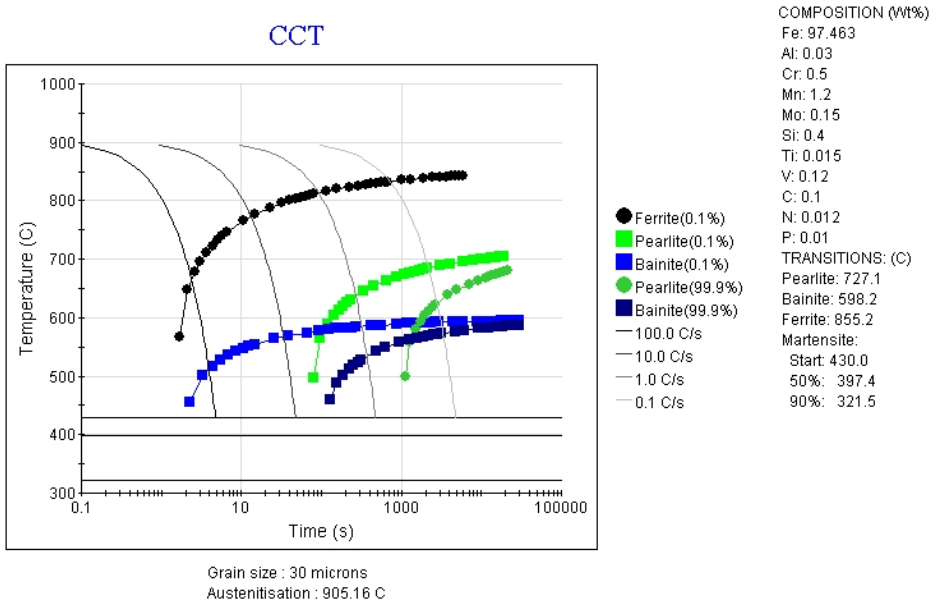

Figure 113: Steel M3 CCT diagram predicted by JMATPro with a 30µm average equivalent austenite grain diameter

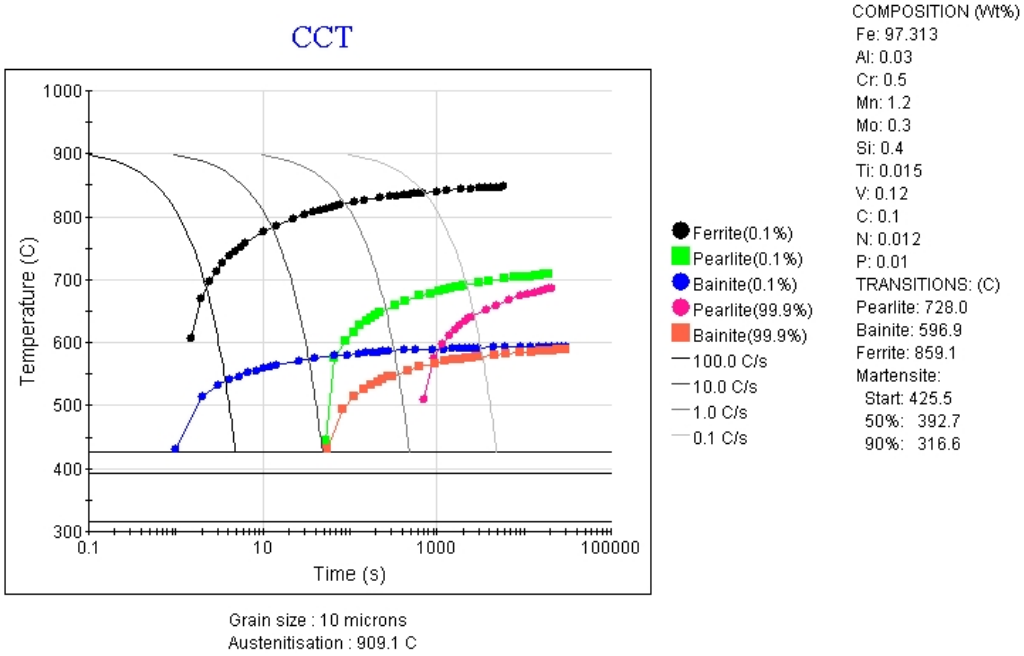

Figure 114: Steel M3 CCT diagram predicted by JMATPro with a 10µm average equivalent austenite grain diameter

The precipitation in the steel gives rise to several conclusions about the performance of the steels. Initially, as is expected from the achieved, fine prior austenite grain size, fine TiN precipitates were found throughout the steel, along with small V(CN) precipitates. TEM analysis, specifically selected area diffraction, was used to identify these precipitates, according to the lattice parameters for TiN, VN and VC, listed in the literature. [69, 70] It should be noted that the fine V(CN) precipitates were not identified in specific composition, as per Baker,[70] the lattice parameters of many vanadium containing precipitate structures are nearly identical, making specific precipitate identification near impossible. Following selected area diffraction, center dark field images were captured centered on the diffraction spots, to identify the precipitates generating the spot. In this manner, the TiN precipitation was observed, and found to precipitate with sizes ranging from 50nm-200nm. These precipitates are moderately coarser than those observed in the literature, where precipitates ranged in size from approximately 8nm-70nm.[24, 71] This is intriguing, as in the literature, many of the steels which produced these fine precipitates are of hyper stoichiometric ratios,[71] which conflicts with other literatures,[14, 17, 24-28] where sub stoichiometric Ti:N ratios (<3.42) are effective in refining TiN precipitation.

The presence of the coarse TiN particles in the steel implies TiN precipitation occurs in the liquid, where diffusion rates are high, facilitating coarsening of the particles. Additionally, the particles are not of cuboidal shapes, though they have cuboidal aspects. Since the solubility of TiN is very low, even at high temperatures,[39, 42, 43] it is unlikely that the precipitates underwent dissolution during the 3-minute reheating to 1150°C. Although it is difficult to discern prior austenite grain boundaries under TEM, evidence of TiN on grain boundaries has been found. Specifically, Figures 106-110 display a TiN precipitate which resides on a ferrite grain boundary, as the TiN precipitate resides on the edge of the illuminated region in Figure 110.

Analysis of the fine TiN precipitation in the steel is important for discussing the performance of the steels, as the fine TiN precipitates are the primary agent responsible for the fine PAGS seen in the experiments. To this end, the Ti and N in the steels are analyzed with the solubility equations present in Shanmugam[39] and Gladman[42]. Here, at the levels present in the studied steels, the solubility equations do not predict precipitation in the liquid:

$$\log([Ti][N]) = 3.82 - \frac{15{,}020}{T} \quad \text{(Austenite: 870°C – 1480°C)} \tag{6-1}$$

$$\log([Ti][N]) = 5.9 - \frac{16{,}586}{T} \quad \text{(Liquid: >1480°C)} \tag{6-2}$$

Here, the precipitation in the liquid for a composition of [Ti] = 0.015wt% and [N] = 0.012wt% predicts precipitation at 1450°C, which is out of range of this equation, and is predominantly within the solid phase, as can be seen in Figure 108, which shows the percentage of the solid phase as the steel cools from the liquid, as predicted by JMATPro. Additionally, the precipitation in the austenite was predicted at 1710°C, well outside of the limit of the equation, and above the solid. As such, the precipitation in the steel appears to first occur when the solid first forms, when the solubility decreases significantly from the solubility in the liquid.

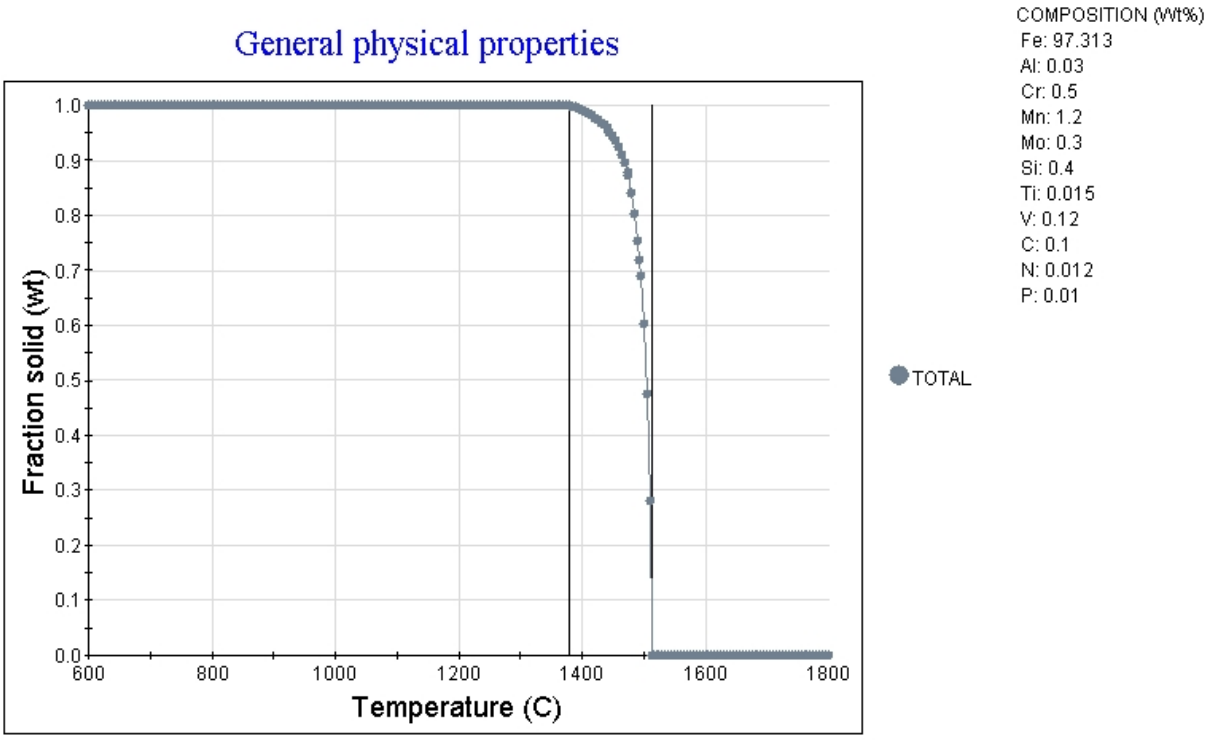

Figure 115: Steel M3 solid phase fraction vs temperature during cooling from liquid phase

For this reason, although some coarse TiN particles are seen in the steels, implying some precipitation in the liquid,[72] these will be excluded in this analysis, as they make up a small volume fraction of the total TiN precipitation distribution.

Additionally, the precipitation equations predict that at 1150°C, the maximum temperature the forgings are reheated to in processing, the titanium and nitrogen remaining in the solid solution is $2.4 * 10^{-5}$wt% and $7.6 * 10^{-3}$wt%, respectively, while the titanium and nitrogen precipitated is $1.5 * 10^{-2}$wt% and $4.4 * 10^{-3}$wt%, respectively. Considering this, at 1150°C, 99.8% of the titanium, the substoichiometric element in the TiN, has precipitated. Thus, for this analysis, the full precipitation capacity of TiN in the steels will be assumed to have precipitated in the solid austenite as a fine dispersion of TiN particles, present for pinning of austenite grain boundaries throughout the thermomechanical processing of the steels.

From analysis of the fine TiN observed in the TEM imaging, the average volume of the TiN particles (assuming a cubic geometry) approaches 110,000nm^3. For simplification purposes, these particles were modelled as spherical particles of identical volumes, with an average radius of 29.6nm. To investigate the pinning capabilities of particles in this size range, this was compared to values for grain boundary pinning observed in the literature. The critical particle radius for pining of grain boundaries is given by the equation: [33, 47]

$$r_c = \frac{6R_0 f_v}{\pi} * \left(\frac{3}{2} - \frac{2}{z}\right)^{-1} \quad (6\text{-}3)$$

Where r_c is the critical particle radius below which pinning can occur, R_0 is the mean radius of the matrix grain and f_v is the volume fraction of the precipitates. Here, z is a term which describes the growth of the grains and can change in value throughout the process from $\sqrt{2}$, providing a maximum particle size, to 2, providing the smallest maximum particle size for pinning. In computing this value for a grain size of 10μm equivalent circular radius, the critical particle size can be seen to vary from approximately 10.8nm in radius to 62.9nm in radius. The average size of the particles observed in this experiment are sufficiently below this value, and thus are determined to possess strong pinning effects.

The distribution of the TiN particles is calculated from an analysis of the average particle size, determined from TEM imaging, and the volume fraction of TiN, calculated from the equation:

$$F_v = \frac{[Ti] + {}^{[Ti]}/_{3.42}}{100} * \frac{\rho_M}{\rho_{TiN}} \quad (6\text{-}4)$$

Where f_v is the volume fraction of the precipitates, [Ti] is the titanium content in wt%, ρ_M is the density of the metal and ρ_{TiN} is the density of TiN. Here, 3.42 is the stoichiometric ratio of titanium to nitrogen, and is used to calculate the nitrogen required to precipitate with the titanium. The volume fraction calculated from this equation is $2.8 * 10^{-4}$. Thus, assuming an average particle volume of 110,000nm^3, the density of fine TiN precipitates in the steel approaches $2.6 * 10^{12}$ particles/cm^3.

For a particle to interact with a grain boundary, it is suggested that the center of the particle must be within one particle radius of the grain boundary.[46] Taking this into consideration, the volume fraction of particles which interact with boundaries is calculable. For a 10μm average diameter equivalent circular austenite grain structure, the volume of the microstructure which resides within one average particle radius (29.6nm here) comprises 0.89% of the microstructure. Thus, for a random precipitation of TiN particles, 0.89% of the particles on average interact with grain boundaries (assuming rigid grain boundaries). Taking this percentage of the total density of particles in the material provides a particle density of $2.3 * 10^{10}$ particles/cm^3 pinning austenite grain boundaries in a 10μm average equivalent austenite grain diameter structure.

To evaluate this particle density for pinning, the density of austenite grain boundaries is calculated, assuming an average equivalent grain radius equal to 10μm. At this grain size, the density of austenite grains is equal to $2.6 * 10^8$ austenite grains/cm^3. Comparing these values, it is noted that there are on average, approximately 88 particles within effective pinning distance of the grain boundaries for a 10μm radius austenite grain structure. Important to note however, is that this approximation excluded the pinning particles residing on the outer side of the boundary. Thus, since every grain boundary is shared between two austenite grains, this approximation is doubled to 176 pinning particles residing within effective pinning distance of the grain boundaries for the

average austenite grain in a 10μm radius austenite grain structure. A final note for this approximation must be clarified. As this argument modeled the austenite structure as being comprised of purely spherical grains, which geometrically have the lowest possible grain boundary area to grain volume ratio. Thus, this approximation underestimates the grain boundary volume percentage of the microstructure for real austenite microstructures, and thus, underpredicts the quantity of effective pinning particles in the microstructure.

The interparticle distance of the precipitates can be calculated from a general approximation, assuming a three-dimensional array of particles. This distance is calculated by:

$$d = \frac{1}{n^{1/3}} \tag{6-5}$$

Where d is the interparticle distance, and *n* is the number density of particles in the steel. This calculates an interparticle distance equal to 0.73μm. This value compares very favorably to the diameter of the austenite grain structures observed in the project, which ranged from approximately 7μm to approximately 100μm. Due to the large difference between the grain size and the interparticle distance, very few grains in the microstructure are expected to lack sufficient particle pinning.

In considering the pinning of this quantity of particles, an approximation is calculated using the Zener pinning force for an individual particle, in an austenite grain structure with 29.6nm radius particles and 10μm average equivalent austenite grain radius. Here, the Zener pinning force for a single particle of radius 29.6nm is calculated at approximately $7 * 10^{-8}$ N. The pinning pressure of 176 pinning particles, exerted on the grain boundary area for a 10μm radius austenite grain, is thus calculated at 10,400Pa.

Analysis of the pinning pressures of the fine TiN in the steel can be conducted using the equations presented by Palmiere[47]. In this work, the pinning pressure of the TiN precipitation distribution observed was calculated using the rigid boundary model:[29-33]

$$F_{PIN}^{R} = \frac{6\,\sigma\,f_{\mathrm{v}}}{\pi\,r} \tag{6-6}$$

Where σ = 0.8 J/m^2 in austenite [34], f_{v} is the volume fraction of precipitates, and r is the average particle radius. Here, the pinning pressure is estimated as approximately 14,600Pa.

The rigid grain boundary model is simplistic and makes assumptions which are not realistic. To this extent, the pining value of the flexible boundary model was also calculated:[30, 35]

$$F_{PIN}^{F} = \frac{3\,\sigma\,f_{\mathrm{v}}^{\,2/3}}{\pi\,r} \tag{6-7}$$

Here, the pinning pressure is estimated as approximately 111,000Pa, exceeding the pressure calculated from the rigid boundary model, as this model assumes the austenite grain boundaries flex indefinitely, until complete pinning is achieved. As a rough approximation, the average of the values predicted by these models is taken. Thus, the calculated pinning pressure is 70,100Pa.

To put this value into perspective, the driving pressure for grain coarsening has been calculated for a 20μm average equivalent austenite grain diameter microstructure. The equation for the driving pressure for grain growth is: [73, 74]

$$P_d = \alpha\,\frac{\gamma}{D} \tag{6-8}$$

Where $_{\gamma}$ = 0.5 J/m^2, [75] α = 4 [76] and D is the average equivalent austenite grain diameter. For D=20μm, the driving pressure equals 100,000Pa.

Of key interest here is the significant difference between the pinning pressure provided by the TiN distribution and the driving pressure for grain growth. It is noted here that the calculated pinning pressure of the observed particles does not equal the driving pressure for grain growth for grain sizes similar to those found in the project. This difference can be attributed to one of two sources. The first is due to errors in the calculation of pinning force. Note that the equations assumed spherical particles, and TiN precipitates are overwhelmingly non-circular. This could be significant, as the shape of particles is known to have impacts on the pinning forces generated by those particles.[46] The second source of this difference is present in error in the values used in these calculations, specifically the average particle radius. As fine precipitates are very difficult to observe, even with TEM technologies, it is possible that only the coarsest nanoscale TiN particles were observed. If this is true that the smallest, most effective for pinning particles, were not found, the calculations from this distribution would change significantly. A larger quantity of finer particles would increase the pinning pressure generated by the TiN particles, as is seen from analysis of the pinning equation. This is expected to be the source of the difference between the pinning pressure and the grain growth driving pressure in the steels, suggesting that the precipitation in the steel is even finer than that which was observed in this project.

Apart from the fine TiN in the steel, the other fine precipitate is the fine V(CN) in the steel. Here, VN precipitation is assumed to proceed until the nitrogen in solution is depleted. These particles were observed to be of an average size less than 10nm in diameter, taken as 5nm in diameter for estimation. The volume fraction of VN precipitates in the steel is calculated according to:

$$F_v = \frac{[N]+3.64[N]}{100} * \frac{\rho_M}{\rho_{VN}} \quad (6\text{-}9)$$

Where F_v is the volume fraction of the precipitates, [N] is the nitrogen content remaining in solid solution after TiN precipitation in wt%, ρ_M is the density of the metal and ρ_{VN} is the density of VN. Here, the volume fraction is calculated at $4.5 * 10^{-4}$. Through this precipitation, approximately 0.028 wt% of the vanadium is removed from solution. For further precipitation, the remaining 0.092 wt% of vanadium is assumed to precipitate as VC, according to the following equation:

$$F_v = \frac{[V] + {}^{[V]}/_{4.25}}{100} * \frac{\rho_M}{\rho_{VC}} \quad (6\text{-}10)$$

Where [V] = 0.092 wt%, and ρ_{VC} is the density of VC. Here, the volume fraction of VC is calculated as $1.54 * 10^{-3}$. Thus, the total vanadium precipitation volume fraction is the sum of the two volume fractions, equaling $1.99 * 10^{-3}$.

Taking the average particle diameter as 5nm, the particle density can be calculated as $3.04 * 10^{16}$ particles/cm^3. Using the same interparticle estimation as was used for the TiN particles, it is found that the interparticle distance of VN in the steel is equal to 32nm.

Finally, from the equation set forth by Gladman[11], the precipitation hardening increment from the VN precipitation in steel M3 is calculated as such:

$$\Delta\sigma_y = (0.538Gbf^{1/2}/X) \ln(X/2b) \quad (6\text{-}11)$$

Where $\Delta\sigma_y$ is the yield strength change due to precipitation (MPa), G is the shear modulus (MPa), *b* is the burgers vector (mm), *f* is the volume fraction of particles, and X is the real (spatial) diameter of the particles (mm). Here, from Gladman[11], the values of G (81,600MPa) and b (0.248nm) are taken. Taking *f* as $1.99 * 10^{-3}$, and X as $5 * 10^{-6}$mm gives a precipitation strengthening increment equal to approximately 220MPa for steel M3 in the fast ACRT condition.

All precipitation analysis in the steel was conducted on the fast ACRT forging condition. If, however, similar precipitation sizes are assumed in steel M1, precipitation strengthening increments at a lower vanadium level can be calculated. Here, the volume fraction of VN is calculated as $4.5 * 10^{-4}$, and the volume fraction of VC calculated as $5.3 * 10^{-4}$. Thus, the total volume fraction is $9.8 * 10^{-4}$.

Again, from the equation set forth by Gladman[11], the precipitation strengthening increment for steel M1 can be calculated as 158MPa. This difference aligns well with the results found in the project, and roughly coincides with the strength differences observed between steels M1 and M3 in the ACRT and fast ACRT conditions.

7.0 Conclusions

1. Titanium and vanadium microalloyed steels with sub stoichiometric Ti:N ratios (Ti < 3.42 N) were characterized in laboratory hot forging simulations. High T_{GC} temperatures of 1200°C to 1250°C were observed in the titanium nitride bearing steels, exceeding the observed T_{GC} of the non-titanium bearing control steel, 10V40, with T_{GC} = 1100°C. Recrystallization temperatures, T_{95}, as well as post deformation prior austenite grain sizes, were determined, and found to be 800°C to 850°C for the T_{95} temperatures, and approximately 10μm in equivalent circular prior austenite grain diameter for the steels deformed at 900°C. Finally, laboratory cooling experiments demonstrated the possibility of attaining ferrite, bainite and martensite microstructures in the final sample, following thermomechanical processing, with pearlite being mostly unattainable in the studied cooling schedules and steels.

2. Full forging deformations were performed at cooperative industrial partner MFC facilities and compared to the standard 10V40 ACRT forging condition. Mechanical testing was conducted in the forgings, providing both tensile and Charpy data for comparison. Ultimate tensile strengths for the steels showed the ultimate tensile strength of the 10V40 in the ACRT condition to be 780 MPa. The TiN bearing steels in similar conditions had UTS values lower than this by varying degrees, ranging from approximately 550 MPa to 720MPa. These same steels however, saw improvements in forging toughness, with increases in toughness of 20% to 50% commonly seen. Finally, a cold WQRT condition was tested, and found to attain higher UTS values (790MPa – 940MPa) than the 10V40 ACRT condition, while retaining higher toughness values. This cold WQRT condition, however, was incapable of attaining a majority martensite microstructure, evidencing the insufficient hardenability additions for the project steels.

3. Hot water quenching was tested as a method to produce an accelerated cooling rate, which could be reliably stopped at intermediate temperatures to allow the formation of bainite in the forgings. Large quantities of bainite were found in the steels, but the UTS values of these steels (550MPa – 680MPa) did not manage to reach the levels attained in the fast ACRT forging condition. This was attributed to the low hardenability elements hampering the volume fraction of bainite attainable in the steel, as well as the low carbon levels, limiting the strength of the bainite when higher volume fractions are attained. High toughness values, similar to or exceeding the fast ACRT conditions are found in these conditions.

4. TEM and SEM imaging was used to analyze the precipitation in the M3 fast ACRT forging condition, which had the highest UTS (710MPa – 720MPa) of the non-cold WQRT TiN bearing steels. In the steel, both coarse MnS and TiN precipitates of a 1μm-3μm size were observed. Additionally, fine TiN precipitates, with a size range of 50nm to 200nm, were found. These precipitates have the typical TiN "cuboidal" shape and were identified using selected area diffraction and center dark field imaging. The final precipitates were fine V(CN) precipitates. These precipitates were spherical in shape, and typically of sizes less than 10nm in diameter.

8.0 Future Work

Although the TiN-bearing steels studied in this project demonstrated success in attaining high levels of prior austenite grain refinement, the proposed levels of strength, specifically in the accelerated cooling conditions, were not achieved.

Further experiments would be best designed by building on the knowledge gained here, starting with the compositions of the steels. As a primary objective of the project was to determine steels with low economic and environmental associated costs, additional processing steps and additional alloying of expensive elements, namely vanadium and molybdenum, is not feasible. It is suggested here, instead, that the cheaper alloying, specifically carbon, manganese and chromium, be increased to impact the properties of the final forgings. Here, carbon would help to increase both the strength of the bainite and the martensite, increasing the performance of the steels in the accelerated cooling conditions. Increases in manganese and chromium, elements with profound hardenability impacts, would complement the increased carbon levels, through allowing higher volume fractions of bainite and martensite to be attained in the final microstructure. The effectiveness of the RCF grain refinement of the steels was not fully realized in the designing of the steels, and with the knowledge gained here, further alloying is suggested to counter the reduced hardenability from the enhanced prior austenite grain refinement.

The hot WQRT method tested in the project shows promise as well, as the submersion trials showed elevated cooling rates of approximately 10°C/s throughout the thick geometry tested, while maintaining enough control over the cooling to allow for selective water end temperatures to be achieved. Changes in the submersion time, to change the WET, or perhaps changes in the

submersion temperature, or even submersion fluid, to adjust cooling rates, are suggested to take full advantage of this cooling technique.

Finally, in the literature was seen some excess at producing fine TiN precipitates, even at compositions exceeding the stoichiometric Ti:N ratio of 3.42.[71] In light of this, possible future experiments may consider the use of higher levels of titanium, approaching the atomic percent of the nitrogen, in order to investigate the possibility of further fine TiN precipitation in the steel. This does not seem necessary, or even beneficial, however, as the steels were determined successful in austenite grain refinement, and further titanium alloying would likely lead to further coarsening of the already present, coarse TiN precipitates observed in the steel.

Bibliography

[1] A. J. DeArdo and M. Hua, "Some Comments on the Physical Metallurgy of HSLA Steels Containing Vanadium and Nitrogen," in *Materials Science and Technology 2014*, Warrendale, 2014.

[2] M. Hua, X. Liang and A. J. DeArdo, "Microalloyed Steels for High-Strength Forgings," in *ASM International*, Metals Park, 1986.

[3] T. Siwecki, "Modelling of microstructure evolution during recrystallization controlled rolling," *ISIJ international*, vol. 32, no. 3, pp. 368-376, 1992.

[4] A. J. DeArdo, C. I. Garcia and M. Hua, "Multi-Phase, Microalloyed Bar Steels for Premium Forging Performance," in *AIM International Conference Hot Forming of Steels & Product Properties - Associazione Italiana di Metallurgia*, Grado, 2009.

[5] F. B. Pickering, "Physical Metallurgy and the design of the steels," *Applied Science Publishers*, pp. 1-88, 1978.

[6] G. E. Dieter and D. J. Bacon, Mechanical Metallurgy, vol. 3, New York: McGraw-Hill, 1986.

[7] J. Friedel, Dislocations, London: Pergamon Press, 1964.

[8] E. Orowan, "Discussion in The Symposium on Internal Stresses in Metals and Alloys, Inst.," in *Metals*, London, 1948.

[9] Y. Xiang and D. J. Srolovitz, "Dislocation climb effects on particle bypass mechanisms," *Philosophical Magazine*, vol. 86, no. 25-26, pp. 3937-3957, 2006.

[10] K. Danas and V. S. Deshpande, "Plane-Strain Discrete Dislocation Plasticity with Climb-Assisted Glide Motion of Dislocations," *Modelling and Simulation in Materials Science and Engineering*, vol. 21, no. 4, 2013.

[11] T. Gladman, "Precipitation Hardening in Metals," *Materials Science and Technology*, vol. 15, no. 1, pp. 30-36, 1999.

[12] E. O. Hall, "The deformation and ageing of mild steel: III discussion of results," in *Proceedings of the Physical Society*, Cambridge, 1951.

[13] N. J. Petch, "The cleavage strength of polycrystals," *J. Iron and Steel Inst.*, p. 174 .

[14] T. Siwecki and G. Engberg, "Recrystallization controlled rolling of steels," *Thermo-Mechanical Processing in Theory, Modelling & Practice[TMP] exp 2*, pp. 121-144., 1996.

[15] H.-l. Wei, G. Liu, H. Zhao and M. Zhang, "Effect of carbon content on hot deformation behaviors of vanadium microalloyed steels," *Materials Science and Engineering: A 596*, pp. 112-120, 2014.

[16] A. R. Rosenfield, G. T. Hahn and J. D. Embury, "Fracture of Steels Containing Pearlite," *Metallurgical Transactions*, vol. 3, pp. 2797-2804, 1972.

[17] Y. Z. Zheng, A. J. DeArdo, R. M. Fix and G. Fitzsimons, "Achieving Grain Refinement Through Recrystallization-Controlled Rolling and Controlled Cooling in V--Ti--N Microalloyed Steels," in *HSLA Steels, Technology and Applications*, Metals Park, 1983.

[18] J. Chen, M. Y. Lv, S. Tang, Z. Y. Liu and G. D. Wang, "Low-carbon bainite steel with high strength and toughness processed by recrystallization controlled rolling and ultra fast cooling (RCR+ UFC)," *ISIJ International*, vol. 54, no. 12, pp. 2926-2932.

[19] K. F. Al-Hajeri, "The grain coarsening and subsequent transformation of austenite in the HSLA steel during high temperature thermomechanical processing," University of Pittsburgh, 2005.

[20] S. F. Medina, M. Gómez and L. Rancel, "Grain refinement by intragranular nucleation of ferrite in a high nitrogen content vanadium microalloyed steel," *Scripta Materialia*, vol. 58, no. 12, pp. 1110-1113, 2008.

[21] L. Cheng and K. M. Wu, "New insights into intragranular ferrite in a low-carbon low-alloy steel," *Acta Materialia*, vol. 57, no. 13, pp. 3754-3762, 2009.

[22] T. Pan, Z. G. Yang, Z. C, B. B. Z and H. S. Fang, "Kinetics and mechanisms of intragranular ferrite nucleation on non-metallic inclusions in low carbon steels," *Materials Science and Engineering: A 438*, pp. 1128-1132, 2006.

[23] Y. Z. Zheng, G. T. Tang and Z. H. Lin, "Precipitation, Recrystallization and Transformation in V--Ti--N Microalloyed Steels," in *HSLA Steels: Processing, Properties and Applications*, Warrendale, 1990.

[24] M. Arribas, B. López and J. M. Rodriguez-Ibabe, "Additional grain refinement in recrystallization controlled rolling of Ti-microalloyed steels processed by near-net-

shape casting technology," *Materials Science and Engineering: A,* vol. 485, no. 1, pp. 383-394, 2008.

[25] M. T. Nagata, J. G. Speer and D. K. Matlock, "Titanium nitride precipitation behavior in thin-slab cast high-strength low-alloy steels," *Metallurgical and Materials Transactions A,* vol. 33, no. 10, pp. 3099-3110, 2002.

[26] M. I. Vega, S. F. Medina, A. Quispe and M. Gomez, "Influence of TiN particle precipitation state on static recrystallisation in structural steels," *ISIJ international,* vol. 45, no. 12, pp. 1878-1886, 2005.

[27] F. B. Pickering, "Titanium nitride technology," in *35th Mechanical Working and Steel Processing Conference,* Warrendale, 1993.

[28] S. F. Medina, M. Chapa, P. Valles and A. Quispe, "Influence of Ti and N contents on austenite grain control and precipitate size in structural steels," *ISIJ international,* vol. 39, no. 9, pp. 930-936, 1999.

[29] S. S. Hansen, J. B. Vander Sande and M. Cohen, "Niobium Carbonitride Precipitation and Austenite Recrystallization in Hot-Rolled Microalloyed Steels," *Metallurgical Transactions,* vol. 11, no. A, p. 387, 1980.

[30] A. J. DeArdo, G. A. Ratz and P. J. Wray, "The Effect of Microalloy Concentration on the Recrystallization of Austenite During Hot Deformation, by L.J. Cuddy," in *The Metallurgical Society of AIME,* Warrendale, 1982.

[31] C. Zener, "Private Communication to C.S. Smith," *Transactions of the AIME,* vol. 175, p. 15, 1949.

[32] N. Hansen, A. R. Jones and T. Leffers, "Recrystallization and Grain Growth of Multi-Phase and Particle Containing Materials," in *1st RISO International Symposium on Metallurgy and Material Science,* Denmark, 1980.

[33] T. Gladman, "On the Theory of the Effect of Precipitate Particles on Grain Growth in Metals," *Proceedings of the Royal Society of London,* vol. 294, p. 298, 1966.

[34] L. E. Murr, "Interfacial Phenomena in Metals and Alloys," Addison-Wesley Publishing Company, Reading, 1975.

[35] C. M. Sellars and G. J. Davies, "Effects of Rolling Variables and Stoichiometry on Strain-Induced Precipitation of Nb(CN) in C-Mn-Nb Steels, by R.K. Amin, G. Butterworth and F.B. Pickering," in *Hot Working and Forming Processes,* London, 1979.

[36] O. Kwon, "Static Recovery and Recrystallization of Hot Deformed FCC Materials, Ph.D. Thesis," University of Pittsburgh, Pittsburgh, 1985.

[37] R. M. Fix, Y. Z. Zheng and A. J. DeArdo, "Mechanical Properties of V--Ti Microalloyed Steels Subject to Plate Rolling Simulations Utilizing Recrystallization Controlled Rolling.(Extended Abstract).," in *HSLA Steels'85*, Russell Township, 1985.

[38] D. Litvinenko, "Development of Vanadium-Nitride-Strengthened Low-Alloy Steels for Large-Diameter Gas Pipelines," in *Proc. Conf. on Microalloying 75*, Metals Park, 1977.

[39] S. Shanmugam, M. Tanniru and R. D. K. Misra, "Precipitation in V bearing microalloyed steel containing low concentrations of Ti and Nb," *Materials science and technology*, vol. 21, no. 8, pp. 883-892, 2005.

[40] T. Gladman, D. Dulieu and I. D. McIvor, "Structure-Property Relationships in High-Strength Microalloyed Steels," in *Micro Alloying 75*, Washington D.C., 1975.

[41] T. Gladman, "HSLA Steels: Processing, Properties and Applications," in *TMS*, Warrendale, 1992.

[42] T. Gladman, "Physical metallurgy of microalloyed steels," *The Institute of Materials*, 1997.

[43] S. Shanmugam, M. Tanniru and R. D. K. Misra, "Microalloyed V–Nb–Ti and V steels Part 2–Precipitation behaviour during processing of structural beams," *Materials science and technology*, vol. 21, no. 2, pp. 165-177, 2005.

[44] M. Tamura, H. Lida, H. Esaka and K. Shinozuka, "Solubility product of VN in austenite of high Cr heat resistant steel," *ISIJ international*, vol. 43, no. 11, pp. 1807-1813, 2003.

[45] K. Inoue, I. Ohnuma, H. Ohtani and K. Ishida, "Solubility product of TiN in austenite," *ISIJ international*, vol. 38, no. 9, pp. 991-997, 1998.

[46] P. A. Manohar, M. Ferry and T. Chandra, "Five Decades of the Zener Equation," *ISIJ International*, vol. 38, no. 9, pp. 913-924, 1998.

[47] E. J. Palmiere, "Suppression of Recrystallization During the Hot Deformation of Microalloyed Austenite," University of Pittsburgh, Pittsburgh, 1991.

[48] A. J. DeArdo, "Unpublished Work".

[49] R. G. Baker and J. Nutting, "Precipitation Processes in Steels," The Iron and Steel Institute, London, 1959.

[50] "G. Kurdjumov and G. Sachs: Z. Phys., 1930, 62, 592.".

[51] E. V. Morales, J. Gallego and H. J. Kestenbach, "On Coherent Carbonitride Precipitation in Commercial MicroAlloyed Steels," *Philosophical Magazine Letters*, vol. 83, no. 2, pp. 79-87, 2003.

[52] T. Tomida, M. Wakita, M. Yasuyama, S. Sugaya, Y. Tomota and S. C. Vogel, "Memory Effects of Transformation Textures in Steel and its Prediction by the Double Kurdjumov-Sachs Relation," *Acta Meterialia,* vol. 61, pp. 2828-2839, 2013.

[53] S. H. M. Anijdan, A. Rezaeian and S. Yue, "The effect of chemical composition and austenite conditioning on the transformation behavior of microalloyed steels," *Materials Characterization 63,* pp. 27-38, 2012.

[54] J. Calvo, I. H. Jung, A. M. Elwazri, D. Bai and S. Yue, "Influence of the chemical composition on transformation behaviour of low carbon microalloyed steels," *Materials Science and Engineering: A,* vol. 520, no. 1, pp. 90-96, 2009.

[55] N. Radović, A. Koprivica, D. Glisic and F. Abdunnaser, "Influence of Cr, Mn and Mo on structure and properties of V microalloyed medium carbon forging steels," *Metalurgija,* vol. 16, no. 1, pp. 1-9, 2010.

[56] M. Maalekian, "The Effects of Alloying Elements on Steels (I)," *Institut für Werkstoffkunde, Schweißtechnik und Spanlose Formgebungsverfahren,* pp. 1-36, 2010.

[57] M. Gómez, R. Lucía and S. F. ". Medina, "Effects of aluminium and nitrogen on static recrystallisation in V-microalloyed steels," *Materials Science and Engineering: A,* vol. 506, no. 1, pp. 165-173, 2009.

[58] E. E. Underwood, "Surface area and length in volume," *QUANTITATIVE MICROSCOPY,* pp. 77-127, 1968.

[59] I. Kozasu, C. Ouchi, T. Sampei and T. Okita, "Hot rolling as a high-temperature thermo-mechanical process," in *Proc. Conf. on Microalloying 75*, Metals Park, 1977.

[60] G. R. Speich, L. J. Cuddy, C. R. Gordon and A. J. DeArdo, "Phase transformations in ferrous alloys," in *TMS-AIME*, Warrendale, 1984.

[61] A. J. DeArdo, "Unpublished research," University of Pittsburgh, 1985.

[62] A. J. DeArdo, in *Microalloying 95*, Warrendale, 1995.

[63] G. E. Dieter, H. A. Kuhn and S. L. Semiatin, Handbook of workability and process design, ASM international, 2003.

[64] L. J. Cuddy and J. C. Raley, "Austenite grain coarsening in microalloyed steels," *Metallurgical Transactions A*, vol. 14, no. 10, pp. 1989-1995, 1983.

[65] C. Zener, "Phase transformations in steel," *Transactions of the Metallurgical Society, AIME 167*, pp. 550-559, 1946.

[66] P. Hellman and M. Hillert, "Effect of second-phase particles on grain growth," *Scandinavian Journal of Metallurgy*, vol. 4, no. 5, pp. 211-219, 1975.

[67] P. C. M. Rodrigues, E. V. Pereloma and D. B. Santos, "Mechanical properities of an HSLA bainitic steel subjected to controlled rolling with accelerated cooling," *Materials Science and Engineering: A*, vol. 283, no. 1, pp. 136-143, 2000.

[68] A. v. d. Steinen, S. Engineer, E. Horn and G. Preis, *Stah u. Eisen*, vol. 95, no. 6, pp. 209-214, 1975.

[69] J. E. Sundgren, B. O. Johansson, S. E. Karlsson and H. T. Hentzell, "Mechanisms of Reactive Sputtering of Titanium Nitride and Titanium Carbide," *Thin Solid Films*, vol. 105, pp. 367-384, 1983.

[70] T. N. Baker, "Processes, Microstructure and Properties of Vanadium Microalloyed Steels," *Materials Science and Technology*, vol. 25, no. 9, pp. 1083-1107, 2009.

[71] M. I. Vega, S. F. Medina, A. Quispe, M. Gomez and P. P. Gomez, "Recrystallisation Driving Forces Against Pinning Forces in Hot Rolling of Ti-Microalloyed Steels," *Materials Science and Engineering*, vol. A, no. 423, pp. 253-261, 2006.

[72] B. Ma, "A Study of Processing, Microstructure and Mechanical Properties of Ultra-High Strength Microalloyed Steel Hot Band Coil For Automotive Applications," ProQuest LLC, Ann Arbor, 2017.

[73] B.R. Patterson, Y. Liu, *Metall Trans*, vol. 23A, pp. 2481-2482, 1992.

[74] P. Hellman, M. Hillert, *Scand J Metall*, vol. 4, pp. 211-219, 1975.

[75] F.J. Humphreys , M. Hatherly, Recrystallization and Related Annealing Phenomen. 2nd ed. Oxford: Elsevier; 2004.

[76] M. Hillert, *Acta Metall*, vol. 13, pp. 227-238, 1964.